Title

Unveiling the Structure-performance Relationship of the Cathode and Anode Catalyst in Electrochemical Water-splitting

Author

Liu, Haotian

Publication Date

2022

Peer reviewed|Thesis/dissertation

UNIVERSITY OF CALIFORNIA
Los Angeles

Unveiling the Structure-performance Relationship of the Cathode and Anode Catalyst in Electrochemical Water-splitting

A dissertation submitted in partial satisfaction
of the requirements for the degree
Doctor of Philosophy in Materials Science and Engineering

by

Haotian Liu

2022

ABSTRACT OF THE DISSERTATION

Unveiling the Structure-performance Relationship of
the Cathode and Anode Catalyst in Electrochemical Water-splitting

by

Haotian Liu
Doctor of Philosophy in Materials Science and Engineering
University of California, Los Angeles, 2022
Professor Yu Huang, Chair

Carbon neutrality has been the most popular topic of the twenty-first century. Substituting non-sustainable fossil fuels with the cleaner energy source hydrogen is a viable strategy for reducing total carbon footprints, but the conventional method of hydrogen production is energy-intensive and polluting. Water electrolysis stands out among all hydrogen production methods due to its low instrumentation requirements and high efficiency. However, water electrolysis costs have yet to be reduced. By engineering the catalysts used at the cathode and anode, the focus of this thesis will be to improve the water electrolysis efficiency and material durability. In addition, corresponding theory is studied in order to reveal the structure-performance relationship of the catalyst, which provides perspective and theoretical support for the design of future catalysts.

In the first chapter, I will briefly describe the current status of global carbon production. The rationale for selecting water electrolysis is then presented, along with an overview of water electrolysis devices.

In the second chapter, I will describe our work (*J. Am. Chem. Soc.* 2018, 140, 29,

9046–9050) on improving the performance of the hydrogen evolution reaction (HER) by applying surface engineering to PtNi alloy. Hydrogen holds the potential of replacing nonrenewable fossil fuel. Improving the efficiency of hydrogen evolution reaction (HER) is critical for environmental friendly hydrogen generation through electrochemical or photoelectrochemical water splitting. Here we report the surface-engineered PtNi-O nanoparticles with enriched NiO/PtNi interface on surface. Notably, PtNi-O/C showed a mass activity of 7.23 mA/μg at an overpotential of 70 mV, which is 7.9 times higher compared to that of the commercial Pt/C, representing the highest reported mass activity for HER in alkaline conditions. The HER overpotential can be lowered to 39.8 mV at 10 mA/cm^2 when platinum loading was only 5.1 μg_{Pt}/cm^2, showing exceptional HER efficiency. The performance improvement could be attributed to the successful creation of $Ni(OH)_2$/Pt(111) interface. $Ni(OH)_2$ facilitated H_2O molecule to be adsorbed on the surface as the first step of HER, and then recombination on the Pt(111) surface happened. Thus, the overall potential needed was decreased. Meanwhile, the prepared PtNi-O/C nanostructures demonstrated significantly improved stability as well as high current performance which are well over those of the commercial Pt/C and demonstrated capability of scaled hydrogen generation.

In the third chapter, I will demonstrate continuation of the last work, which is further improving the alkaline HER performance on Pt-based alloy. Lattice tuning is one of the effective ways to optimize the HER performance on Pt-based alloy. Here, we report a facile lattice tuning method on Pt-based alloy using Cu addition to control the lattice parameter for optimal HER performacne. During the performance evaluation, PtCuNi/C and PtCuNi-O/C showed an average overpotential of 38.8 mV and 31.3 mV at 10 mA/cm^2, respectively. The overpotential of PtCuNi-O/C is dramatically smaller than that of commercial Pt/C (115.2 mV). At an overpotential of 70 mV (-70 mV vs. RHE), the octahedral PtCuNi/C presents a mass activity (MA) of 4.9 mA/μg_{Pt}, while the PtCuNi-O/C demonstrates a MA of 8.7 mA/μg_{Pt}, which is nearly 9.5 folds to that of the commercial Pt/C (0.92 mA/μg_{Pt}). Also, the PtCuNi-O/C can reach a current density of 114 mA/cm^2 at -0.2 V vs. RHE without

iR compensation, which is well above that of Pt/C (22.4 mA/cm^2), indicating a promising potential for the industrial scale hydrogen production. For the stability test, in contrast to the 160.1 mV potential drop for the Pt/C, there was only 55.5 mV, 48.2 mV potential drop for octahedral PtCuNi/C, PtCuNi-O/C, correspondingly, showing a significantly improved durability. Moreover, the dealloyed nanocatalysts showed the best performance when the lattice parameter is in the range of 0.3825-0.3835 nm for both PtNi-O/C and PtCuNi-O/C.

In the fourth chapter, the main focus will be on the anode side featuring oxygen evolution reaction (OER) in acidic media. Developing durable non-precious catalysts for the acidic OER is crucial for the hydrogen production industry. In this regard, we report a facile strategy to synthesize the cobalt-based spinel oxide for the acidic OER with ultra-high activity and outstanding durability. Specifically, the as-prepared $NiCo_2O_4$ delivered a low overpotential of 407 mV vs. reversible hydrogen electrode at 100 mA/cm^2 and only a 68.9 mV increase at 10 mA/cm^2 after 20 hours of chronopotentiometry test. *Ex situ* x-ray absorption spectroscopy studies revealed that Ni mainly occupies the octahedral site. *In situ* x-ray absorption spectroscopy studies demonstrated that adding Ni helped minimize the structure change during the OER, leading to $NiCo_2O_4$'s outstanding durability. Density functional theory calculations demonstrated that the OER overpotential is lowered by 90 mV on the $NiCo_2O_4$ surface compared to that of Co_3O_4. The acidic OER on the $NiCo_2O_4$ spinel structure undergoes a kinetically more favorable direct O-O coupling mechanism rather than the adsorbate evolution mechanism, which was seldom reported regarding acidic OER on non-precious metal oxides. We showcase an ideal way to produce cobalt-based spinel oxides following direct O-O coupling mechanism design rules, achieving promising acidic OER performance cost-effectively.

The last chapter generally conclude the content covered in the thesis and provided some perspective on future catalyst design and scale-up applications.

The dissertation of Haotian Liu is approved.

Xiangfeng Duan

Ximin He

Qibing Pei

Yu Huang, Committee Chair

University of California, Los Angeles

2022

To my family ...

For their support, their patience, and their faith

Because they always love me unconditionally.

TABLE OF CONTENTS

LIST OF FIGURES

LIST OF TABLES

ACKNOWLEDGMENTS

Time flies by. My six-year research career at UCLA and at Huang Lab has been a very distinct yet significant period in my life. I am extremely fortunate to have so many individuals that care about me and want to see me succeed in this quest. First and foremost, I would want to thank my principal investigator, professor Yu Huang. Prof. Huang, in my opinion, has a severe attitude toward science but a caring heart toward her pupils. During my first two years in the group, I was disoriented and lacked a research goal. Then Prof. Huang showed me how to start the project and the proper scientific spirit, which helped me get through the difficult periods. Her expertise, kindness, and diligence greatly expanded my horizon. I could never accomplish so much without her guidance.

Second, I would like to thank my committee members, Prof. Xiangfeng Duan, Prof. Ximin He, and Prof. Qibing Pei, for their assistance with my qualification and final oral exams. I would also like to thank my collaborators Prof. William Andrew Goddard III and Dr. Soonho Kwon from California Institute of Technology for their assistance with theoretical studies, as well as Dr. Qingying Jia and Dr. Ershuai Liu from Northeastern University for their assistance with synchronchon studies. I would also like to thank Dr. Zipeng Zhao, who guided me through my first project and assisted me in adjusting to my new surroundings when I first arrived at UCLA. I would also want thank my other fellow colleagues, Dr. Enbo Zhu, Dr. Zhihong Huang, Dr. Chungsuk Choi, Dr. Lele Peng, Dr. Huilong Fei, Dr. Mufan Li, Dr. Chengzhang Wan, Dr. Luning Chen, Dr. Jin Huang, Dr. Peiqi Wang, Dr. Guangyan Zhong, Dr. Bocheng Cao, Dong Xu, Jin Cai, Zeyan Liu, Bosi Peng, Ao Zhang, Yang Liu, Jingxuan Zhou, Sibo Wang, and Heting Pu, etc.

I think it is worth one paragraph in the acknowledgements to express my gratitude to my mom and dad. Though the environment is changing every second, but their love on me never alters. When I was in middle school, they always woke up early in the morning, prepared breakfast, and accompanied me on my way to school, day after day. Now I am in the US,

they cannot give me their love physically like before. But they still talk to me every day, ask me if I need any help, and tell me to concentrate on learning. They use their time and efforts to make my life much easier and smoother. They are not only parents who brought me up, but also great educators. As life has reached a certain point as a student, I would like to say a word to my parents here in my thesis: thank you!

Another particular person for whom I want to show my gratitude is Weiting, my beloved. This is the already the 8^{th} year that we are in relationship, and the 4^{th} year we are married. During these years, when I make progress, you cheer for me; when I meet obstacles, you shed light for me; when I am in blue, you persuade me. I can not imagine how much more difficult my life would be without you. You brightened my day. Thank you, and let us spend the rest of our lives together.

VITA

2012–2016 B.S. (Chemistry), University of Science and Technology of China, Hefei, Anhui, China

2016–present Ph.D., Research Assistant (Materials Science and Engineering), UCLA, Los Angeles, CA, US

PUBLICATIONS

Selected 5 Publications

1. Z Zhao, **H Liu** (co-first), W Gao, W Xue, Z Liu, J Huang, X Pan, Y Huang, Surface-Engineered PtNi-O Nanostructure with Record-High Performance for Electrocatalytic Hydrogen Evolution Reaction, *J. Am. Chem. Soc.* 2018, 140, 29, 9046–9050

2. L Peng, Z Wei, C Wan, J Li, Z Chen, D Zhu, D Baumann, H Liu, C S Allen, X Xu, A I Kirkland, I Shakir, Z Almutairi, S Tolbert, B Dunn, Y Huang, P Sautet, X Duan, A fundamental look at electrocatalytic sulfur reduction reaction, *Nat. Catal.* 2020, 3, 9, 762-770

3. H Fei, J Dong, C Wan, Z Zhao, X Xu, Z Lin, Y Wang, H Liu, K Zang, J Luo, S Zhao, W Hu, W Yan, I Shakir, Y Huang, X Duan, Microwave-assisted rapid synthesis of graphene-supported single atomic metals, *Adv. Mater.* 2018, 30, 35, 1802146

4. Z Zhao, C Chen, Z Liu, J Huang, M Wu, H Liu, Y Li, Y Huang, Pt-based nanocrystal for electrocatalytic oxygen reduction, *Adv. Mater.* 2019, 31, 31, 1808115

5. J Huang, Y Liu, M Xu, C Wan, H Liu, M Li, Z Huang, X Duan, X Pan, Y Huang, PtCuNi tetrahedra catalysts with tailored surfaces for efficient alcohol oxidation, *Nano Lett.* 2019, 19, 8, 5431–5436

CHAPTER 1

Introduction

1.1 The Call for Carbon Neutrality

Carbon neutrality has been the most popular subject in the twenty-first century. The vast majority of major economies, including the United States, the European Union, Russia, and China, have declared their carbon-neutral objectives. Carbon neutrality is defined simply as the equilibrium between the amount of carbon emitted by humans and the amount of carbon absorbed by nature. According to data from the European Parliament, natural sinks can absorb between 9.5 and 11 Gt CO_2 annually, while yearly carbon emissions have reached 38.0 Gt in 2019[1].

To achieve carbon neutrality, it is essential to reduce carbon dioxide output. Even though carbon dioxide is not considered a pollutant, it comprises the great majority of greenhouse gases (GHG). Since the beginning of the Industrial Revolution, humans have been responsible for nearly all GHG increases in the atmosphere[2]. According to the United States Environmental Protection Agency (USEPA), the primary sources of greenhouse gas (GHG) emissions are transportation, electricity, industry, agriculture, and commercial and residential, and the percentage from the US can be found in **Figure 1.1**. Particularly for transportation, 90%[3] of the primary energy source is still fossil fuels, and the primary byproduct of burning fossil fuels is carbon dioxide. Consequently, substituting fossil fuels with clean energy sources is a viable strategy for reducing carbon dioxide emissions.

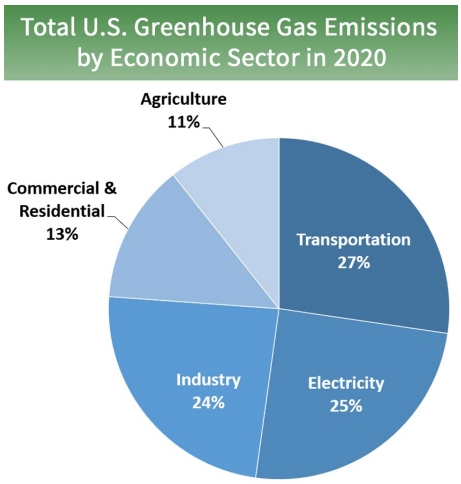

Figure 1.1: Total U.S. greenhouse gas emissions by economic sector in 2020

1.2 Hydrogen Production

Hydrogen distinguishes out among clean energy sources since the only byproduct of its oxidation is water. In addition, hydrogen possesses a higher specific energy of 141.86 (HHV) MJ/kg than other common substances, such as natural gas (53.6 MJ/kg), gasoline (46.4 MJ/kg), and diesel fuel (45.6 MJ/kg)[4,5]. With the development of hydrogen fuel cells, it is feasible to transform the chemical energy stored in hydrogen directly into electricity as a source of power at a very high conversion rate[6,7]. In addition to basic research, fuel-cell automobiles[8], fuel-cell ships[9], and fuel-cell aircraft[10] have been intensively researched during the past two decades. And major automakers, including Toyota, have revealed their commercialized fuel-cell automobiles. In the meantime, as the fuel cell's energy source, hydrogen production must become more cost-effective, environmentally friendly, and generation-efficient.

Currently, there are two basic sources for commercial hydrogen production: fossil fuels and renewable sources (**Figure 1.2**). Unfortunately, more than ninety percent of hydrogen is created from fossil fuels by reforming natural gas, which contradicts the objective of reducing fossil fuel consumption. In addition to environmental issues, the hydrogen produced in this manner contains a significant amount of contaminants, such as CO and NO_x, etc., which are

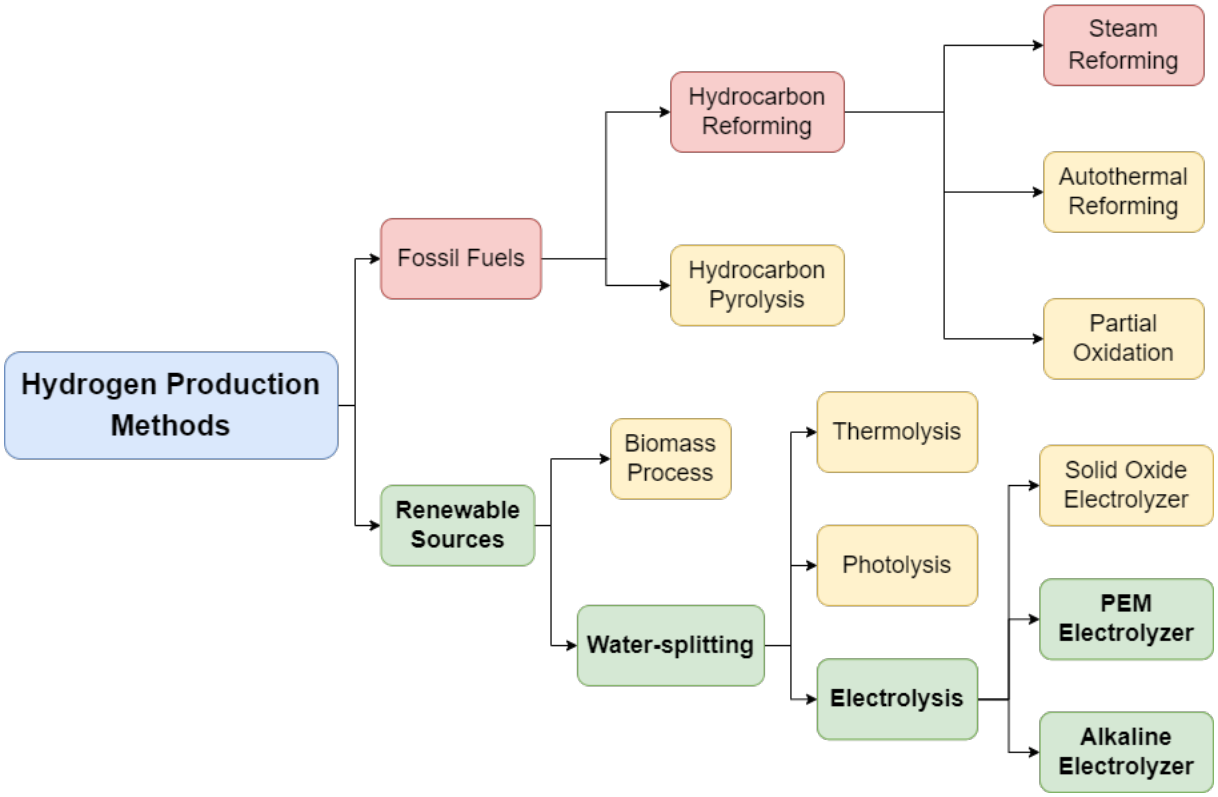

Figure 1.2: Current state-of-art hydrogen production methods. Adapted from ref[12].

harmful to the environment and can hinder hydrogen usage, e.g., CO is known to poison the Pt-based catalyst used in the fuel cell system[11].

In contrast, renewable hydrogen generation, which relies mostly on water-splitting, can supply hydrogen with extremely high purity (99% or higher) and no carbon or nitrogen impurities. The energy conversion efficiency of water electrolysis and natural gas reforming is around 70%, while the cost of water electrolysis is 10.30 $/kg compared to 2.27 $/kg for natural gas reforming[12]. Reducing the cost of water-splitting is one of the primary objectives of developing electrolysis-based hydrogen production.

1.3 Basic Water-splitting Techniques

The purpose of an electrolyzer is to produce hydrogen and oxygen from water using electricity as the driving force. The ideal power source for green hydrogen generation would be renewable energy, such as solar, wind, or hydro power, among others. **Figure 1.3** depicts the structure of a proton exchange membrane (PEM) water electrolyzer. Using lab-scale instruments, it will be difficult and expensive to perform comprehensive study on water-splitting; hence, half-cell reactions, hydrogen evolution reaction (HER) and oxygen evolution reaction (OER), will be researched separately. As displayed in **Figure 1.3B** the reactions taking place in cathodic chamber with hydrogen evolution and anodic chamber with oxygen evolution (OER), which are:

$$\textbf{Cathode} : 2H^+ + 2e^- = H_2$$

$$\textbf{Anode} : 2H_2O - 4e^- = O_2 + 2H^+$$

These two reactions are the two vital ones for this thesis, which will be covered in detail respectively in the following chapters.

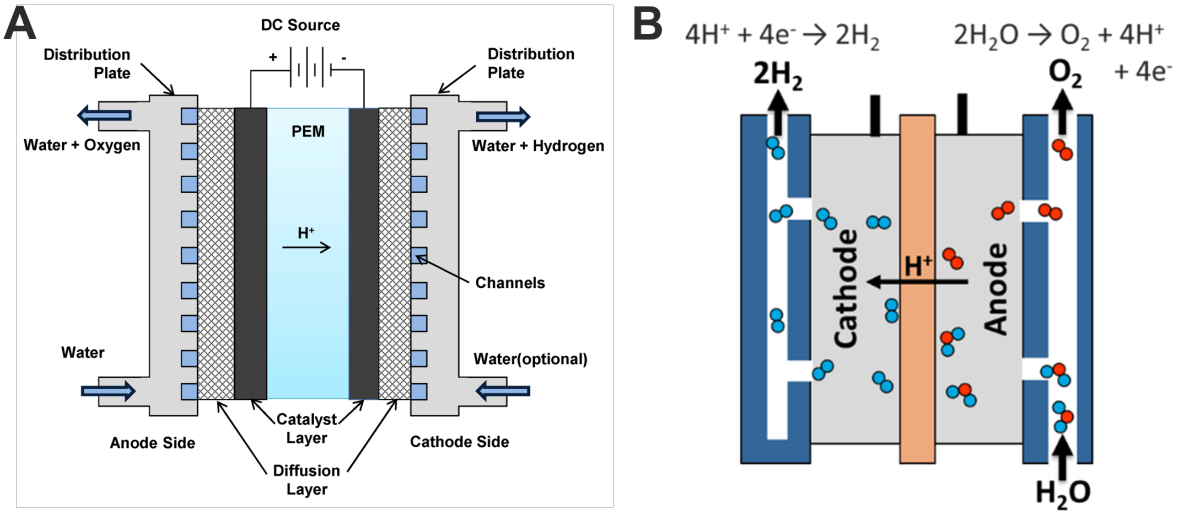

Figure 1.3: **A.** Schematic illustration of a typical PEM Electrolyzer. **B.** Cathode and anode reaction in an electrolyzer.

CHAPTER 2

Surface-Engineered PtNi-O/C Nanostructure with Record-high Performance for Electrocatalytic Alkaline Hydrogen Evolution Reaction

2.1 Background

Note: This chapter is a version of the co-first-authored ref.[13]

As discussed in chapter 1, electrolysis of water produces hydrogen that is a suitable replacement for nonrenewable and polluting fossil fuels. Acidic or alkaline conditions are typically necessary for water splitting. Due to the fact that the HER in acidic media frequently has a high equipment requirement, the HER in alkaline media is researched more frequently due to its benign condition and lower equipment requirement.

By far, platinum-group-metal-based (PGM-based, or precious-metal-based) catalysts and non-platinum-group-metal-based (non-PGM-based, or non-precious-metal-based) catalysts have been broadly researched for the HER. Though non-PGM-based catalysts, such as metal phosphides,[14,15] metal nitrides,[16,17] metal chalcogenides,[18,19] and metal carbides,[20,21] can reduce the cost of the catalyst while delivering acceptable HER performance, there is still a significant gap between the performance of PGM-based catalysts and non-PGM-catalysts.[22,23] As the holy grail of green hydrogen production, photoelectrochemical water splitting necessitates a low overpotential to power the HER. The present bottleneck for the PGM-based catalyst is the expensive PGM precursors, low HER activity, and mediocre durability.

2.2 Alkaline HER Mechanism Study and Catalyst Design

The HER mechanism contains two steps, which are the Volmer-Heyrovsky pathway or Volmer-Tafel Pathway[24] (H* means active hydrogen atom adsorbed on the catalyst surface):

$$\textbf{Volmer} : H_2O + e^- = H^* + OH^-$$

$$\textbf{Heyrovsky} : H_2O + H^* + e^- = H_2 + OH^-$$

$$\textbf{Tafel} : H^* + H^* = H_2$$

According to recent research on platinum-catalyzed alkaline HER, the performance limitation of Pt stems primarily from the fact that Pt is generally ineffective at initiating the water dissociation step (Volmer Step). However, Pt can facilitate the second step, Heyrovsky or Tafel step, with high efficiency.[25] Due to its inability to conduct the second step, $Ni(OH)_2$ is not an ideal material for the alkaline HER, but it is effective at cleaving the H-OH bond.[26,27] It is possible to combine the two types of materials to produce a new interface and heterostructures; hence, the majority of both materials can be exploited. Consequently, HER performance can be enhanced. As depicted in **Figure 2.1**, Subbaraman et al. presented a $Ni(OH)_2$/Pt(111) surface, and the $Ni(OH)_2$ decorated Pt surface displayed an 8-fold increase in HER activity compared to the Pt(111) surface.[25] On $Ni(OH)_2$, the water molecule is dissociated prior to the formation of H* on this heterosurface. On the Pt(111) surface, the two H* recombine to produce a hydrogen molecule.

The creation of $Ni(OH)_2$ on the Pt(111) surface at the micrometer scale is successful, while nanoscale attempts have met with little success.[28,29] The performance of alkaline HER produced by these nanocatalysts is significantly worse to that reported in investigations involving single crystals. In this paper, we provide octahedral PtNi nanoparticles with NiO enriched on the surface that change into $Ni(OH)_2$ in alkaline media.[30,31] The synthesized nanoparticle with nanoscale $Ni(OH)_2$/Pt(111) hetero-surface exhibited record-high alkaline HER activity as well as exceptional durability.

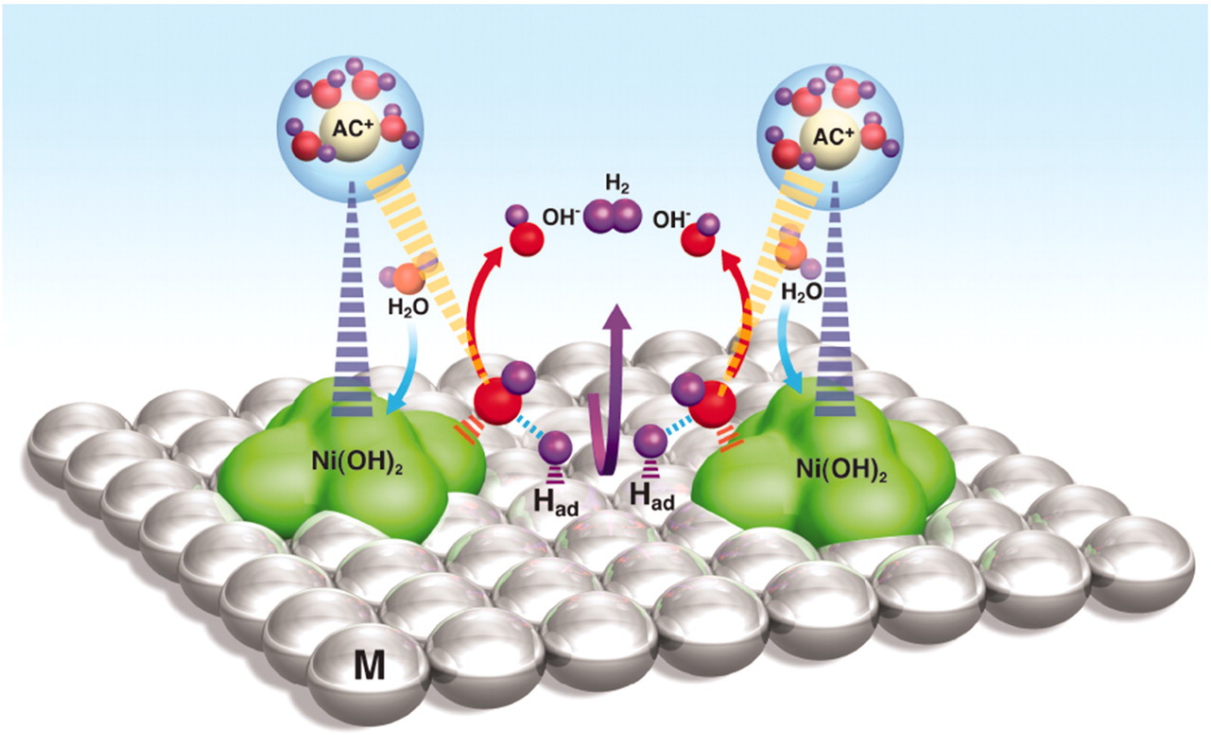

Figure 2.1: Schematic illustration of the promoted alkaline hydrogen evolution on the $Ni(OH)_2$ decorated Pt(111) surface. Reproduced from ref[25].

2.3 Materials and Methods

2.3.1 Chemicals and Materials

Platinum(II) acetylacetonate [$Pt(acac)_2$, Pt 48.0% min], nickel(II) acetylacetonate [$Ni(acac)_2$, 95%], nickel acetate tetrahydrate [$Ni(Ac)_2{\cdot}4H_2O$, $\geq$ 99%], benzoic acid ($\geq$ 99.5%), perchloric acid ($HClO_4$) were purchased from Sigma Aldrich. Commercial Pt/C catalyst (20 wt% Pt, and particle size 2 to 5 nm) were purchased from Alfa Aesar. Ethanol (200 proof) was obtained from DeconLabs, Inc. Potassium hydroxide (KOH), N, N-dimethylformamide (DMF, $\geq$ 99.8%), acetone ($\geq$ 99.5%), and isopropanol ($\geq$ 99.5%) were purchased from Fisher Chemical. All reagents were used as received without further purification. Carbon black (Vulcan XC-72) was received from Cabot Corporation and annealed for 2h at 400°C under an Ar gas environment before used. The deionized water (18 MΩ/cm) was obtained from an ultra-pure purification system (Milli-Q advantage A10)

2.3.2 Synthesis of Pt-Ni Octahedra

18mg of carbon black was suspended in 9 mL DMF in a 25 mL glass vial and underwent ultrasonication for at least 30 min. 9 mg of $Pt(acac)_2$, 7.2 mg of $Ni(acac)_2$ and 85 mg of benzoic acid were dissolved in 1 mL DMF to attain a clear solution, then were added to the carbon black suspended DMF solution. The vial was then capped and ultrasonic processed for 5 min. The vial was then heated with a magnetic stirring rate of 300 rpm in an oil bath at 140 °C and kept for 1.5 hours, then heated to 150 °C and kept for 48 hours. After being cooled to room temperature, the carbon-supported dispersive Pt-Ni alloy octahedra were obtained by centrifuging. Then the precipitate was washed with an isopropanol/acetone mixture at least 3 times to remove the organic impurities and precursor residues. The obtained catalyst was then dried under vacuum denoted as PtNi/C.

2.3.3 Catalyst Annealing

About 20 mg of catalyst was loaded into a quartz boat, and the quartz boat was placed within the center area of a quartz tube. Then the quartz tube was heated to 200 °C in the air for 2 hours to obtain PtNi-O/C.

2.3.4 Characterization

Transmission electron microscopy (TEM) images were taken on an FEI T12 operated at 120 kV. Energy-dispersive X-ray spectroscopy (EDS) was taken on an FEI TITAN operated at 300 kV. Atomic resolution high angle annular dark field scanning transmission electron microscopy (HAADF-STEM) images and EDS mapping were also taken on a JEOL Grand ARM300CF TEM/STEM operated at 300 kV. Samples for TEM measurements were prepared by dropping about 10-20 μL Pt-based octahedra isopropanol dispersion onto a carbon-coated copper grid (Ladd Research, Williston, VT) using a pipette and then drying under ambient conditions. Al grids and Au grids(Ted Pella, Redding, CA) were used for the EDS sample preparation. Powder X-ray diffraction patterns (PXRD) were collected on a Panalytical X'Pert Pro X-ray Powder Diffractometer with Cu-Kα radiation. The composition of catalysts was determined by inductively coupled plasma atomic emission spectroscopy (ICP-AES, Shimadzu ICPE-9000) as well as EDS. X-ray photoelectron spectroscopy (XPS) tests were done with a Kratos AXIS Ultra DLD spectrometer.

2.3.5 Electrode Preparation and Electrochemical Test

To obtain a homogeneous catalyst ink, 0.71 mg of dried PtNi/C was mixed with 1 mL ethanol and ultra-sonic processed for 5 min. Then 16 μL of Nafion (5 wt%) was added to each solution. Then, 10 μL of the homogeneous ink was dropped onto a 5 mm diameter glassy carbon electrode (Pine Research Instrumentation) using a pipette. Pt loading was about 1.0 μg, which was estimated by ICP-AES for all Pt-based alloy samples. The ink

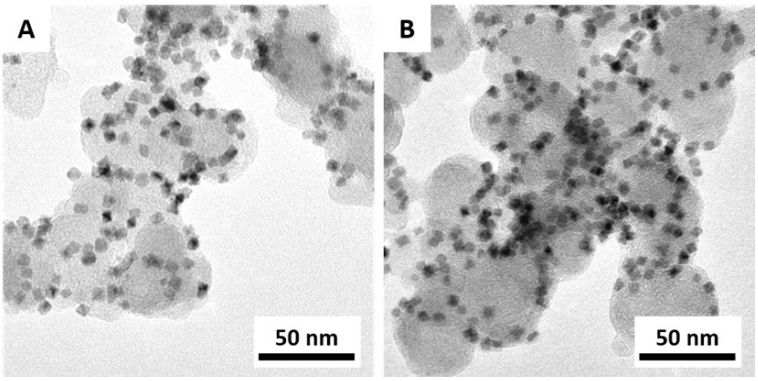

Figure 2.2: TEM images of **(A)** before annealing PtNi/C and **(B)** after annealing PtNi-O/C.

was dried under ambient air, then was ready for the electrochemical test. The procedure for obtaining PtNi-O/C catalyst ink is similar but changed from PtNi/C to PtNi-O/C. The procedure was still similar for the baseline commercial Pt/C (20 wt%) but changed 0.71 mg of PtNi/C to 0.50 mg of Pt/C. Pt loading was still about 1.0 μg for the commercial Pt/C catalyst. All electrochemical tests were carried out on a three-electrode cell from Pine Research Instrumentation. The working electrode was a glassy carbon rotating disk electrode (RDE) coated with the corresponding catalyst. The reference electrode was a Hg/HgO electrode from CH Instrument. A graphite rod was used as the counter electrode. The alkaline electrolyte 1.0 M KOH and 0.1 M KOH were saturated by N_2 respectively. Cyclic voltammetry (CV) was conducted in each solution between 50 mV to 1100 mV vs. Reverse Hydrogen Electrode (RHE) at a sweep rate of 100 mV/s. Hydrogen Evolution Reaction (HER) was tested between -200mV to 100 mV vs. RHE in each solution at a sweep rate of 5 mV/s for 1 M KOH and -500 mV to 100 mV vs. RHE for 0.1 M KOH. The impedance of each solution was tested on a Princeton VersaSTAT 4 electrochemistry workstation. The solution resistances measured via impedance test are 4.5 Ω and 39.2 Ω for 1.0 M and 0.1 M KOH, respectively. The above values are used for post-test iR correction. Electrochemical surface area (ECSA) was tested through hydrogen under potential deposition (H^{upd}) in nitrogen saturated 0.1 M $HClO_4$.

2.4 Results and Discussion

2.4.1 Structural Characterization

PtNi octahedra were synthesized using a one-pot hydrothermal technique, as described in the synthesis process. Corresponding PtNi-O/C was produced by annealing PtNi/C in air. To illustrate the structure of the synthesized catalyst, serial characterization was performed. The transmission electron microscopy (TEM) pictures revealed that the PtNi/C and PtNi-O/C nanoparticles had a homogeneous octahedral shape and were distributed uniformly across the carbon support. The nano octahedra have a 5.4 ± 0.6 nm edge length (**Figure 2.2**). **Figure 2.3A** depicted a schematic representation of the surface engineering procedure during the annealing procedure. On the PtNi-O/C nanoparticle, high-resolution scanning transmission electron microscopy (HRSTEM) revealed the creation of a core-shell structure. As shown in **Figure 2.3B, C**, the interplanar distances of PtNi/C {200} facets and PtNi-O/C {111} facets in the core region were 0.190 nm and 0.222 nm, respectively. Based on the face center cubic (fcc) structure, this interplanar spacing equated to a lattice parameter of 0.380 nm for PtNi/C and 0.384 nm for PtNi-O/C. During annealing, the lattice expansion of PtNi-O/C suggests Ni dealloying from PtNi/C.

On PtNi-O/C octahedron, a shell of 2-3 atomic layers with lighter contrast than PtNi/C octahedron can be found. The interplanar spacing matches NiO {111} facets. This is the evidence that Ni dealloyed from the structure's core, merged, and enriched on the surface. The HRSTEM energy dispersive spectroscopy (EDS) elemental mapping (**Figure 2.3D, E** clearly showed a Ni enrichment on the surface of PtNi-O/C. The composition was also calculated by EDS, and both PtNi/C and PtNi-O/C have a ratio of 60.5% and 39.5% for Pt and Ni, respectively.

According to the X-ray diffraction (XRD) pattern (**Figure 2.4A**), each sample exhibited only one set of peaks matching to the fcc structure. The lattice parameters determined by Bragg's Law based on the XRD pattern matched the lattice parameters obtained in the core

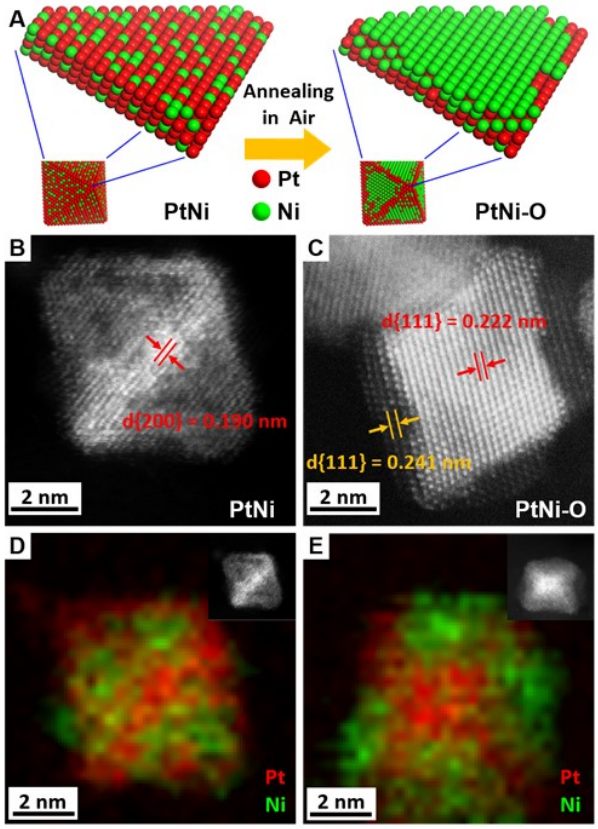

Figure 2.3: **(A)** Sketch illustration of PtNi/C to PtNi-O/C transformation via annealing in the air. HRSTEM images of octahedral nanostructures **(B)** PtNi/C, **(C)** PtNi-O/C. EDS mapping images of octahedral nanostructures **(D)** PtNi/C **(E)** PtNi-O/C. Insert images in D, E are corresponding HRSTEM images of mapped nanostructures.

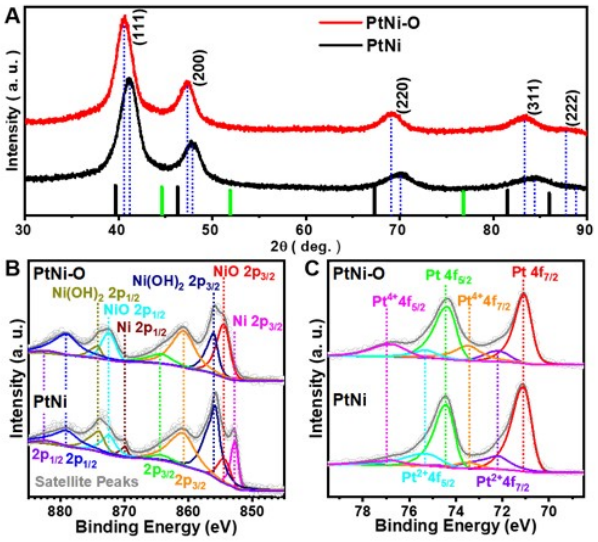

Figure 2.4: **(A)** XRD spectra of octahedral PtNi/C and PtNi-O/C, black, and green droplines represent the standard peak position of Pt (PDF #04-0802), Ni (PDF #04-0850), respectively. XPS spectra comparison of PtNi/C and PtNi-O/C. **(B)** Ni 2p region **(C)** Pt 4f region.

region of PtNi/C and PtNi-O/C in HRSTEM pictures. In addition, the platinum ratio can be determined using Vegard's Law. After annealing, the Pt ratio increased from 0.70 to 0.81 (**Table 2.1**), which was further proof of the dealloying process.

X-ray photoelectron spectroscopy (XPS) was employed to determine the surface valence of the catalyst. As shown in **Figure 2.4B**, there was a substantial amount of metallic Ni on PtNi/C; however, this peak disappeared on PtNi-O/C, showing that the metallic Ni was entirely oxidized to the species with a higher valence. According to the literature, the higher valence forms NiO and $Ni(OH)_2$ may be distinguished from one another.[32,33] Compared to PtNi/C, the $Ni(OH)_2$ peak intensity decreased on PtNi-O/C, however the NiO peak intensity increased, suggesting that $Ni(OH)_2$ lost a water molecule and converted into NiO during the annealing process. **Figure 2.4C** displayed the XPS spectrum of the Pt 4f area, where metallic Pt and a minor amount of Pt^{2+} predominated. Notably, Pt^{4+} was observed in a large quantity on PtNi-O/C but in a negligible amount on PtNi/C as a result of surface

Table 2.1: XRD comparison of octahedral PtNi/C, PtNi-O/C nanostructures

Sample	(111) peak at 2θ (deg.)	Approximate Pt ratio according to Vegard's Law
PtNi/C	41.16	0.70
PtNi-O/C	40.63	0.81

Table 2.2: XPS comparison of octahedral PtNi/C, PtNi-O/C nanostructures. The atomic ratio is based on Pt 4f and Ni 2p region

Sample	Pt	Ni
PtNi/C	49.1%	50.9%
PtNi-O/C	39.8%	60.2%

oxidation during annealing. The surface enrichment of Ni-based XPS spectra (**Table 2.2**) also revealed a dealloying process occurred during annealing in air. In addition, following annealing, the major peak (111) shifted to a lower angle that is near to that of metallic Pt, which may be the result of dealloying. In the meantime, HRSTEM EDS confirmed the creation of the NiO layer on the shell of the octahedron. Ni dealloyed from the PtNi/C core and merged to the surface after annealing, whereas Ni was equally distributed along the nanoparticle before to annealing (**Figure 2.2D, E**).

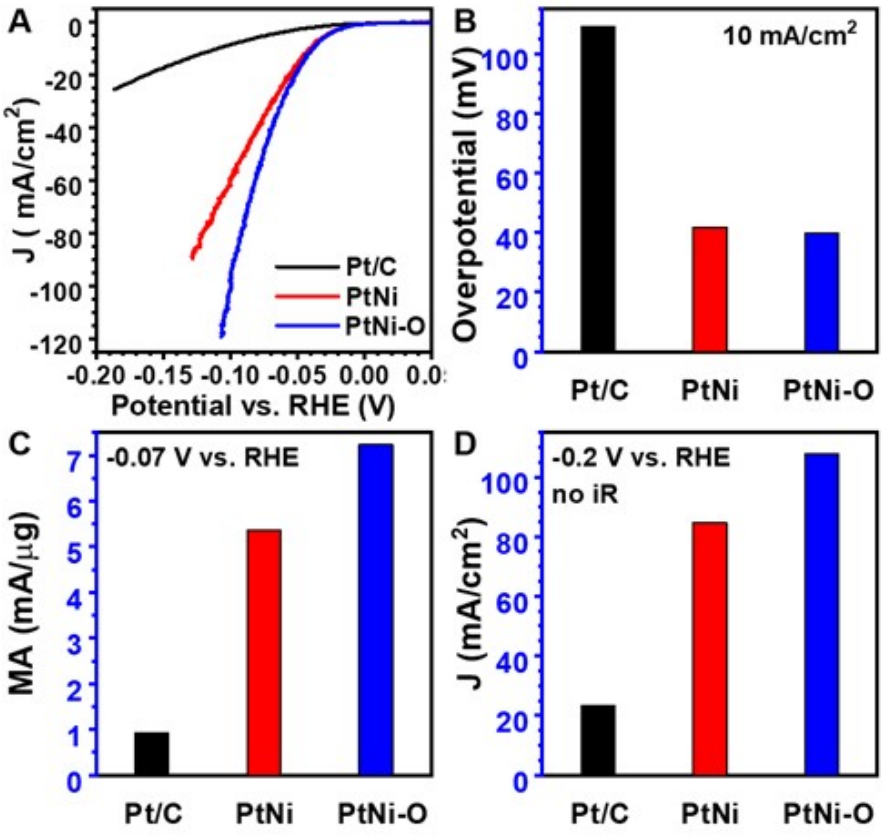

Figure 2.5: Comparison of commercial Pt/C, PtNi/C, PtNi-O/C **(A)** HER polarization curve **(B)** overpotential at 10 mA/cm^2, **(C)** mass activity at -0.07 V vs. RHE, **(D)** current density at -0.2 V vs. RHE (without iR compensation). All the polarization curves were recorded in 1.0 M KOH with a scan rate of 5 mV/s, and a rotation rate of 1600 r.p.m. All the current densities were normalized to the geometric area of the working electrode. iR compensation is applied in figures if not specifically noted.

2.4.2 Electrochemical Performance Evaluation

The performance of the alkaline HER was assessed by loading the catalyst onto the rotating disk electrode (RDE) utilizing three electrodes. For all catalysts, the loading was maintained at 1.0 μg of Pt, as estimated by inductively coupled plasma atomic emission spectroscopy (ICP-AES). As previously described, the HER activity was evaluated using CV scans with a sweeping rate of 5 mV/s in 1.0 M KOH. (**Figure 2.5A**) In general, the annealed PtNi-O/C exhibited superior performance to its native form PtNi/C and to commercial Pt/C. All potential refers to reversible hydrogen electrode (RHE). At a current density of 10 mA/cm^2, the overpotentials of PtNi-O/C and PtNi/C were 39.8 mV and 41.7 mV, respectively, which were significantly lower than that of commercial Pt/C (108.9 mV) (**Figure 2.5B**). At an overpotential of -70 mV, the mass activity (MA) of PtNi-O/C and PtNi/C was 7.23 mA/μg_{Pt} and 5.35 mA/μg_{Pt}, respectively, which is 7.86 and 5.82 times that of commercial Pt/C (**Figure 2.5C**) At an overpotential of -200 mV, PtNi-O/C was able to generate a current density greater than 100 mA/cm^2 without iR correction (**Figure 2.5D**), suggesting a significant potential for industrial applications.

It is worth noting that, the PtNi-O/C shows the highest HER mass activity in the alkaline condition to the best of our knowledge by that time (**Table 2.3**). In addition, the electrochemical active surface area (ECSA) was measured in 0.1 M $HClO_4$ (**Figure 2.6**), and the specific activity was computed using the measured ECSA. PtNi-O/C exhibited a specific activity of 14.8 mA/cm$^2_{ECSA}$ at -0.07 V in 1.0 M KOH, which is 11.5 times that of commercial Pt/C (1.29 mA/cm$^2_{ECSA}$). PtNi-O/C's enhanced alkaline HER activity is attributable to the effective development of NiO islands on the surface of the octahedra. After hydrogenation in the electrolyte, the heterostructure $Ni(OH)_2$/Pt(111) was generated, which is the structure intended for high-efficiency HER that facilitates simultaneous water dissociation and hydrogen recombination.

The stability of the catalyst was evaluated using chronopotentiometry (CP) at a fixed

Table 2.3: Comparison of the developed octahedral PtNi/C and PtNi-O/C with state-of-the-art Pt-based catalysts (with iR compensation)

Sample	Loading (μg/cm^2)	η at 10 mA/cm^2 (mV)	MA at -0.07 V (mA/μg)	Ref.
PtNi	5.1	41.7	5.35	This Work
PtNi-O	5.1	39.8	7.23	This Work
Pt NWs/ SL-Ni(OH)$_2$	16	~70	0.679	Ref[28]
NiO$_x$/Pt$_3$Ni Pt$_3$Ni$_3$-NWs	15.3	40	2.59	Ref[29]
Pt$_3$Ni$_2$ NWs/SC	15	42	2.48	Ref[23]

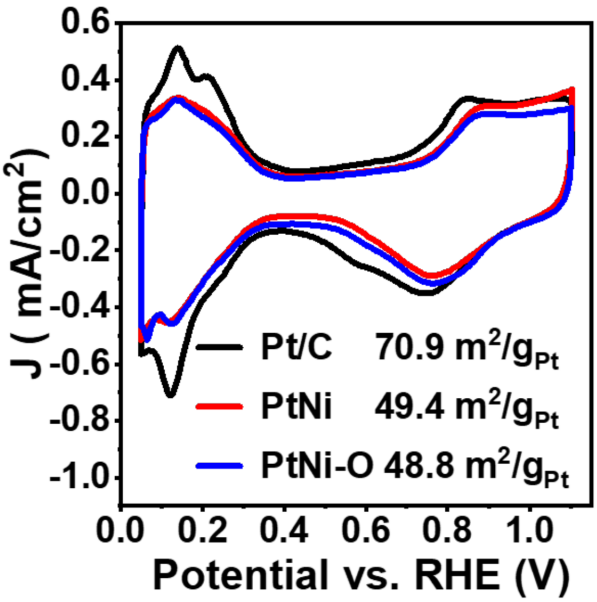

Figure 2.6: CV curves of Pt/C, PtNi/C, PtNi-O/C for H_{upd} estimation and related ECSA

Table 2.4: Composition comparison of octahedral PtNi, PtNi-O nanostructures before and after the HER durability test based on EDS.

Sample	Pt	Ni
PtNi-O/C	60.5%	39.5%
PtNi/C	60.5%	39.5%
PtNi-O/C After CP	66.1%	33.9%
PtNi/C After CP	66.4%	33.5%

current density of 10 mA/cm^2 in 1.0 M KOH. After the 10-hour test, both PtNi-O/C and PtNi/C showed robust durability of only 61.64 mV and 75.45 mV drop in overpotential, which was much better than the commercial Pt/C (260.7 mV). After the stability test, there was only 5.6% and 6.0% Ni loss for PtNi-O/C and PtNi/C, respectively. The comparison of the TEM images of the commercial Pt/C, PtNi/C, and PtNi-O/C before and after the CP test were displayed in **Figure 2.7**. After the CP test, PtNi/C and PtNi-O/C mostly maintained the octahedral morphology, while obvious sintering and aggregation can be the commercial Pt/C. Moreover, the Ni enrichment was still maintained after the stability test on PtNi-O/C according to HRSTEM EDS (**Figure 2.7**).

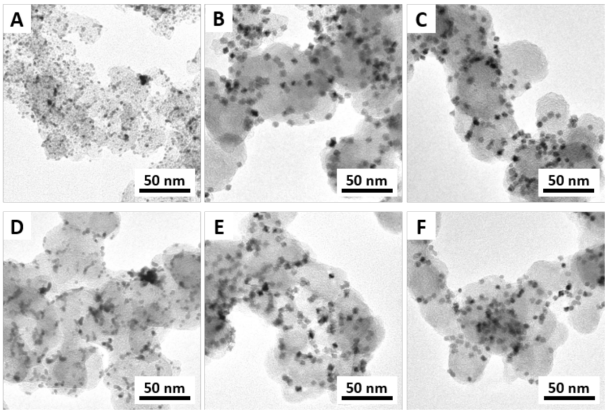

Figure 2.7: TEM images of materials before HER durability test **(A)** Pt/C, **(B)** octahedral PtNi/C **(C)** octahedral PtNi-O/C, after HER stability test **(D)** Pt/C, **(E)** octahedral PtNi/C, **(F)** octahedral PtNi-O/C.

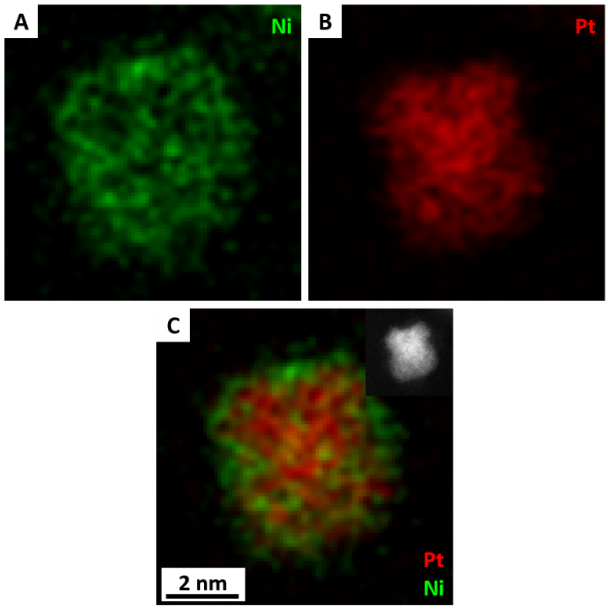

Figure 2.8: EDS mapping images of elemental components in octahedral PtNi-O/C after HER stability test **(A)** Ni, **(B)** Pt, **(C)** Pt and Ni. The insert image is the STEM image of the mapped octahedron.

2.5 Conclusion

In conclusion, we effectively synthesized PtNi-O/C with Ni enriched on the nanoparticle's surface, thereby forming a nanoscale $Ni(OH)_2$/Pt(111) heterosurface. The as-synthesized PtNi-O/C exhibited record-high HER activity in alkaline environments, exhibited exceptional stability, and indicated considerable industrial hydrogen production potential. PtNi-O/C emerged primarily from the formation of the $Ni(OH)_2$/Pt(111) heterosurface, which can promote water dissociation and hydrogen recombination on the same structure, hence accelerating hydrogen evolution.

2.6 Author Contribution

Zipeng Zhao proposed the idea of PtNi alloy, provided the original synthetic recipe, and conducted the corresponding characterization. Haotian Liu proposed the idea of Ni enrichment on the surface, improved the synthetic recipe, and conducted the corresponding characterization. Wenpei Gao and Xiaoqing Pan provided support on HRSTEM image acquisition. Wang Xue, Zeyan Liu, and Jin Huang provided support for other characterizations. Yu Huang proposed the idea and instructed the experiments.

CHAPTER 3

Improving Hydrogen Evolution Reaction Efficiency Through Lattice Tuning

3.1 Background

Note: This chapter is a version of the co-first-authored draft waiting for submission.

Continuing from the last chapter, this chapter will be focusing on improving the alkaline HER performance of the Pt-based alloy through lattice tuning. As discussed thereinbefore, dramatic improvement for the HER in alkaline electrolytes has been achieved by depositing $Ni(OH)_2$ on Pt(111) with two-dimensional (2D) Pt islands [$Ni(OH)_2$/Pt-islands/Pt(111)]. The HER activity of $Ni(OH)_2$/Pt-islands/Pt(111) was shown to be about eight times higher compared to that of Pt(111).[25] Recently, we demonstrated the development of nanoscale $Ni(OH)_2$/Pt(111) like structures enclosed by eight (111) facets through thermally dealloying octahedral PtNi nanoparticles in air.[13] Our PtNi-O/C catalyst showed record-high HER activity per unit platinum mass, 7.9 times better than Pt/C.[13] To further improve the HER efficiency and save energy during water electrolysis, we worked on tuning the lattice parameter of PtCuNi and PtNi based octahedral nanocatalysts with the NiO/Pt(111) interface. Herein, we report optimized PtCuNi-O, PtNi-O catalysts with HER mass activity nearly ten times that of the commercial Pt/C.

3.2 Materials and Methods

3.2.0.1 Chemicals and Materials

Platinum(II) acetylacetonate [$Pt(acac)_2$, Pt 48.0% minimum], nickel(II) acetylacetonate [$Ni(acac)_2$, 95%], nickel acetate tetrahydrate [$Ni(Ac)_2{\cdot}4H_2O$, $\geq$ 99%], copper(II) acetate monohydrate [$Cu(Ac)_2{\cdot}H_2O$, $\geq$ 99%], benzoic acid ($\geq$ 99.5%), perchloric acid ($HClO_4$) were purchased from Sigma Aldrich. Commercial Pt/C catalyst (20 wt% Pt, particle size 2 to 5 nm) were purchased from Alfa Aesar. Ethanol (200 proof) was obtained from Decon Labs, Inc. Potassium hydroxide (KOH), N, N-dimethylformamide (DMF, $\geq$ 99.8%), acetone ($\geq$ 99.5%) and isopropanol ($\geq$ 99.5%) were purchased from Fisher Chemical. All reagents were used as received without further purification. Carbon black (Vulcan XC-72) was received from Cabot Corporation and annealed 2 hours at 400 ℃ under Ar gas environment before used. The deionized water (18 MΩ/cm) was obtained from an ultra-pure purification system (Milli-Q advantage A10).

3.2.1 Synthesis of PtNi Octahedral Nanoparticles on Carbon Support (PtNi/C)

300 mg of carbon black was suspended in 100 mL DMF in a 325 mL pressure vessel and underwent ultrasonication for at least 30 mins. 150 mg of $Pt(acac)_2$, 120 mg of $Ni(acac)_2$ and 1416 mg of benzoic acid were dissolved in 20 mL DMF to attain a clear solution. Then the solution was added to the DMF dispersion of carbon black. The reaction vessel was then capped and ultrasonic processed for 5 mins. The reaction vessel was then heated with a magnetic stirring rate of 300 rpm in an oil bath to 130 °C and kept for 2 hours, then heated to 140 °C and kept for 60 hours. After being cooled to room temperature, the product was obtained by centrifugation. Then the precipitate was washed with isopropanol/acetone mixture for at least three times to remove the organic impurities and precursor residues. The obtained catalyst was then dried under vacuum.

3.2.2 Synthesis of PtNi-O/C through Annealing

About 20 mg of catalyst was loaded in a quartz boat, and the quartz boat was placed within the center area of a quartz tube. Then, the quartz tube was heated to 200 °C or 160 °C in the air for various length of time.

3.2.3 Synthesis of PtCuNi Octahedral Nanoparticles on Carbon Support (PtCuNi/C)

300 mg of carbon black was suspended in 130 mL DMF in a 325 mL pressure vessel glass vial and underwent ultrasonication for at least 30 mins. 150 mg of $Pt(acac)_2$, 75 mg of $Ni(Ac)_2{\cdot}4H_2O$, 7.5 mg of $Cu(Ac)_2{\cdot}H_2O$ and 975 mg of benzoic acid were dissolved in 20 mL DMF to attain a clear solution. Then the solution was added to the DMF dispersion of carbon black. The reaction vessel was then capped and ultrasonic processed for 5 mins. The vial was then heated with a magnetic stirring rate of 300 rpm in an oil bath to 140°C and kept for 1 hours, then heated to 160 °C and kept for 48 hours. After being cooled to room temperature, the product was obtained by centrifugation. Then the precipitate was washed with isopropanol/acetone mixture for at least three times to remove the organic impurities and precursor residues. The obtained catalyst was then dried under vacuum. Synthesis of PtCuNi-O/C through Annealing. About 20 mg of catalyst was loaded in a quartz boat, and the quartz boat was placed within the center area of a quartz tube. Then, the quartz tube was heated to 200 °C or 160 °C in air for various length of time.

3.2.4 Characterization

Transmission electron microscopy (TEM) images were taken on an FEI T12 operated at 120 kV. Scanning transmission electron microscopy (STEM) images were taken on an FEI TITAN operated at 200 kV, and energy-dispersive X-ray spectroscopy (EDS) spectra were measured on an FEI TITAN operated at 300 kV. Atomic resolution high angle annular dark

field (HAADF) STEM images and EDS mapping were taken on a JEOL Grand ARM300CF TEM/STEM operated at 300 kV. Samples for the TEM measurements were prepared by dropping 10 μL Pt-based octahedra isopropanol dispersion onto a carbon-coated copper grids (Ladd Research, Williston, VT) using a pipette and then drying under ambient conditions. Al grids or Au grids (Ted Pella, Redding, CA) were used for the EDS sample preparation. Powder X-ray diffraction patterns (PXRD) were collected on a Panalytical X'Pert Pro X-ray Powder Diffractometer with Cu-Kα radiation. The composition of catalysts was determined by inductively coupled plasma atomic emission spectroscopy (ICP-AES, Shimadzu ICPE-9000) as well as EDS. X-ray photoelectron spectroscopy (XPS) tests were done with Kratos AXIS Ultra DLD spectrometer with Al Kα (1486.6 eV) X-ray source in the University of California, Los Angeles (UCLA). All XAS measurement of PtCuNi-O/C were carrying out with transmission mode for avoiding self absorption issue. Also, Ni, Cu, and Pt reference foils data were collected as references at same time with samples to determine amplitude reduction factor S02. Analysis of the EXAFS data was performed using the Artemis program that combines the multiple-scattering EXAFS computer program FEFF36 and the nonlinear least-squares-fitting computer program FEFFIT[34]. For the representative PtNi-O/C and PtCuNi-O/C, ex situ XANES experiments were conducted at the beamline 7-BM (QAS) in National Synchrotron Light Source II (NSLS) (Brookhaven National Laboratory, NY) at room temperature. Full range Pt L_3-edge, Ni K-edge spectra were collected on the same XANES electrode. The Pt L_3-edge spectra were collected in the transmission mode, and the Ni K-edge spectra were collected in the fluorescence mode, with a Pt/Ni reference foil positioned between I_2 and I_3 as a reference. Typical experimental procedures were utilized with details provided in our previous work.[35] The data were processed and fitted using the IFEFFIT-based programs.[36] The χ(R) were modeled using single scattering paths calculated by FEFF639.

3.2.5 FT-EXAFS analysis

Traditional first shell Fourier Transform (F.T.) EXAFS analysis was performed on PtNi-O/C and PtCuNi-O/C with similar parameter settings. The fits were applied to the Pt L_3-edge. Fittings at the Ni and/or Cu K-edges are infeasible due to the co-presence of Ni/Cu species in the alloying form with Pt and in the form of oxides. Only Ni is used as the surrounding atom identity in the fitting model even fitting the XANES data of PtCuNi-O/C because Ni and Cu are indistinguishable by XANES as surrounding atoms. In both cases, the fittings with the Pt-O pathway included into the model are better than the ones without.

3.2.6 Electrode Preparation and Electrochemical Test

In a typical process, a prepared Pt-based catalyst (PtNi-O/C, PtCuNi-O/C) was mixed with ethanol and ultrasonicated for 5 mins to obtain a catalyst ink. Then Nafion (5 wt%) dispersion was added to the catalyst ink followed by ultrasonication aided mixing; the volume ratio is 16 μL of Nafion dispersion per mL of ink. After sonication, 10 μL of the ink was dropped onto a 5 mm diameter glassy-carbon electrode (Pine Research Instrumentation) using a pipette. Pt loading was about 1.3 μg, which was estimated based on the Pt loading within catalysts determined by ICP-AES for all Pt-based samples. The ink was dried under ambient air, then was ready for the electrochemical test. Commercial Pt/C (20 wt%) was tested as a benchmark, the procedure for preparation of Pt/C catalyst ink was still similar to the procedure for preparing PtNi-O/C and PtCuNi-O/C catalyst ink. The Pt loading was still about 1.0 μg for commercial Pt/C catalyst. All electrochemical tests were carried out on a three-electrode cell from Pine Research Instrumentation. The working electrode was a glassy carbon rotating disk electrode (RDE) coated with the corresponding catalyst. The reference electrode was a Hg/HgO electrode from C.H. Instrument. A graphite rod was used as the counter electrode. The alkaline electrolyte solutions (1 M KOH) were saturated with N_2. Cyclic voltammetry (CV) was conducted in each solution between 50 mV to 1100 mV

vs. Reverse Hydrogen Electrode (RHE) at a sweep rate of 100 mV/s. Hydrogen Evolution Reaction (HER) was tested between -200 mV to 100 mV vs. RHE in each solution at a sweep rate of 5 mV/s for 1 M KOH. The impedance of each solution was tested on a WaveDriver-200 (manufactured by Pine Research Instrumentation, Inc.) electrochemistry workstation. The solution resistances measured via impedance test are 4.5 Ω for 1 M KOH. The above values are used for post-test iR correction.

3.3 Results and Discussion

3.3.1 Structural Characterization

According to literature, the introduction of Cu lead to the change of surface elemental distribution in a Pt-Ni octahedral nanoparticle, which resulted in the improvement of catalytic activity and stability towards electrocatalysis, i.e. oxygen reduction reaction.[37] We prepared PtCuNi octahedral nanocatalyst on carbon support (noted as PtCuNi/C) through a solvent thermal process.[37,38,39] More specifically, N, N-dimethylformamide (DMF) was used as the solvent and reducing agent, platinum acetylacetonate [$Pt(acac)_2$], nickel acetylacetonate [$Ni(acac)_2$], copper acetate monohydrate [$Cu(Ac)_2{\cdot}H_2O$] were used as metal precursors, benzoic acid was used as a shape directing agent. Then the obtained PtCuNi/C was further annealed in air to dealloy the nanoparticle and form surface oxide (**Figure 3.1A**).[13,40] The obtained material is noted as PtCuNi-O/C. We performed multipronged characterization studies to unveil the structure and composition of the prepared catalysts. The transmission electron microscopy (TEM) image revealed that PtCuNi are of octahedral shape with an edge length of 5.8 ± 0.8 nm. The particles were well-distributed on the carbon support (**Figure 3.2**). Similar to PtNi/C, the PtCuNi/C retained their initial size and morphology after annealing in air (**Figure 3.2**). In the X-ray diffraction (XRD) data, only one set of peaks for PtCuNi-O/C were observed, while the XRD peaks of PtCuNi-O/C shifted to lower angles after oxidative annealing, which reflects the lattice parameter expands from 0.3780 nm

to 0.3832 nm according to Bragg's Law (**Figure 3.1B**). Also, the comparison of the x-ray photoelectron spectroscopy (XPS) spectra between PtCuNi/C and PtCuNi-O/C revealed a change in the surface composition induced by annealing. There is a significant increase in the Pt^{4+} fraction in the XPS spectrum of PtCuNi-O/C compared to PtCuNi/C, while most of near-surface Pt and Cu atoms remain in the metallic state (**Figure 3.1C, D**). In contrast, we observe dramatic changes in the XPS spectra of the Ni in these catalysts before and after annealing. Specifically, the peak of the metallic state Ni almost disappears in the XPS spectrum of PtCuNi-O/C (**Figure 3.1E**). The relative surface Ni/Pt ratio increases significantly from 0.53 to 1.27 when PtCuNi/C transformed to be PtCuNi-O/C (Table S1), which suggests the segregation and enrichment of Ni in the oxidized form on the surface of nanoparticles occurs upon the oxidative annealing (**Figure 3.1A**).[13]

Furthermore, the comparison of EDS maps between the unannealed particles with annealed particles supported that Ni migrated from the inner core and enriched on the surface of the nanoparticles during oxidative annealing induced dealloying of original alloy nanoparticles (**Figure 3.3**).

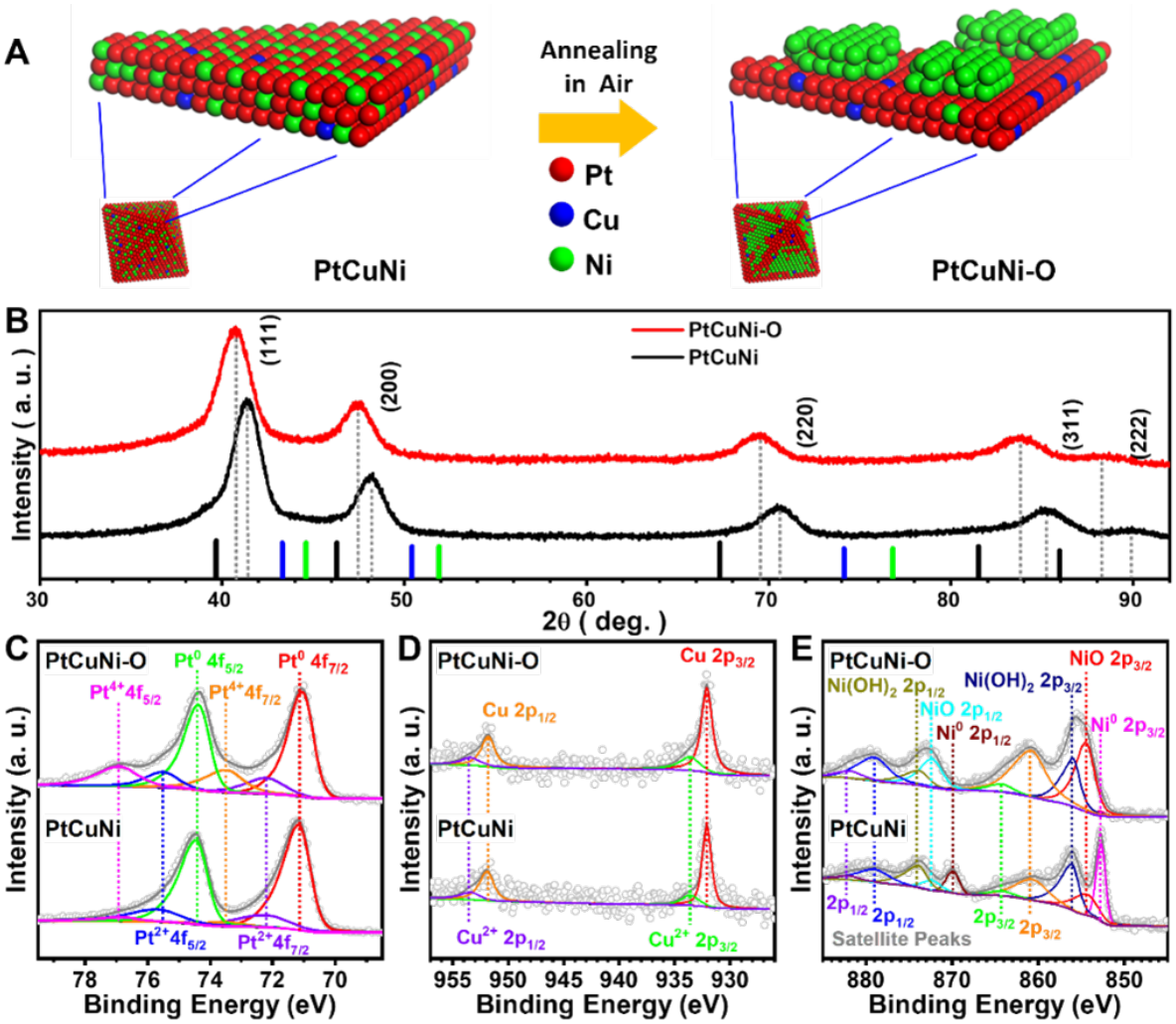

Figure 3.1: **(A)** Schematic illustration of PtCuNi/C to PtCuNi-O/C transformation via annealing in air. **(B)** XRD spectra of octahedral PtCuNi/C and PtCuNi-O/C. Black, blue and green lines are the standard peak position of Pt (PDF #04-0802), Ni (PDF #04-0850) and Cu (PDF #04-0836), respectively. XPS spectra of elements in octahedral PtCuNi/C and PtCuNi-O/C **(C)** Pt, **(D)** Cu, **(E)** Ni. For prepared catalysts, carbon support is omitted in notation in all figures of this work due to limited space, e.g., PtNi-O/C, PtCuNi-O/C are noted as PtNi-O, PtCuNi-O.

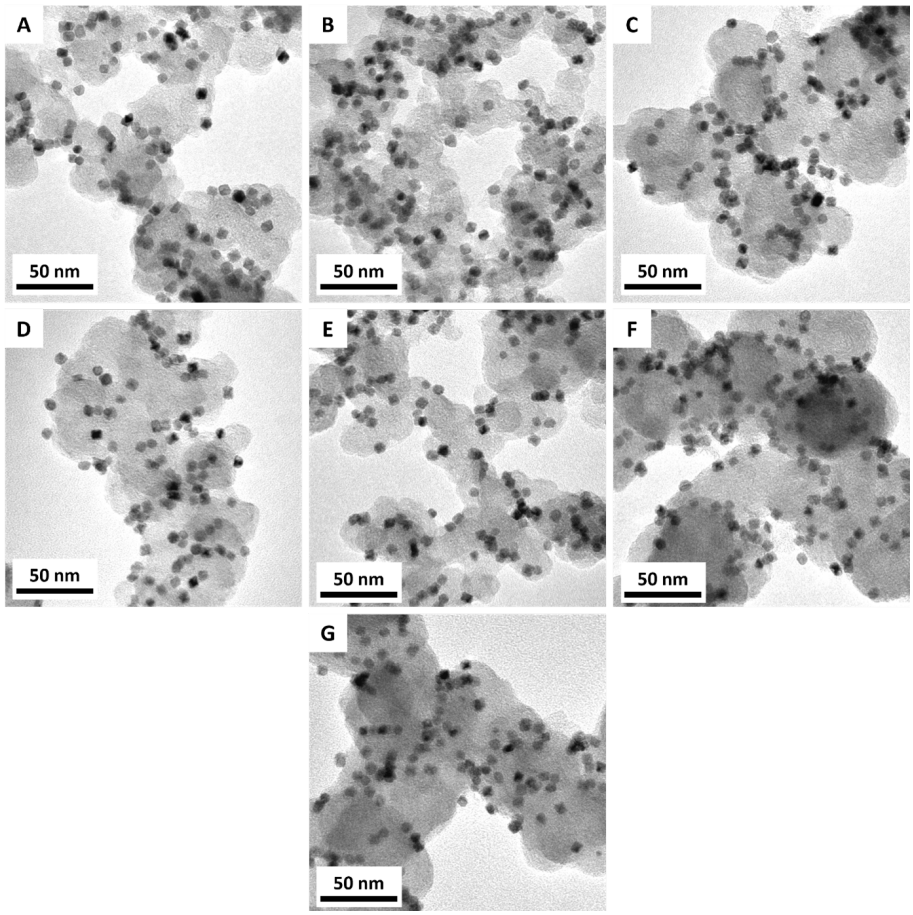

Figure 3.2: TEM image of octahedral PtCuNi/C **(A)** before annealing, annealing in air at 200 ºC **(B)** 15 min, **(C)** 30 min, **(D)** 60 min, **(E)** 120 min, **(F)** 240 min, **(G)** 480 min.

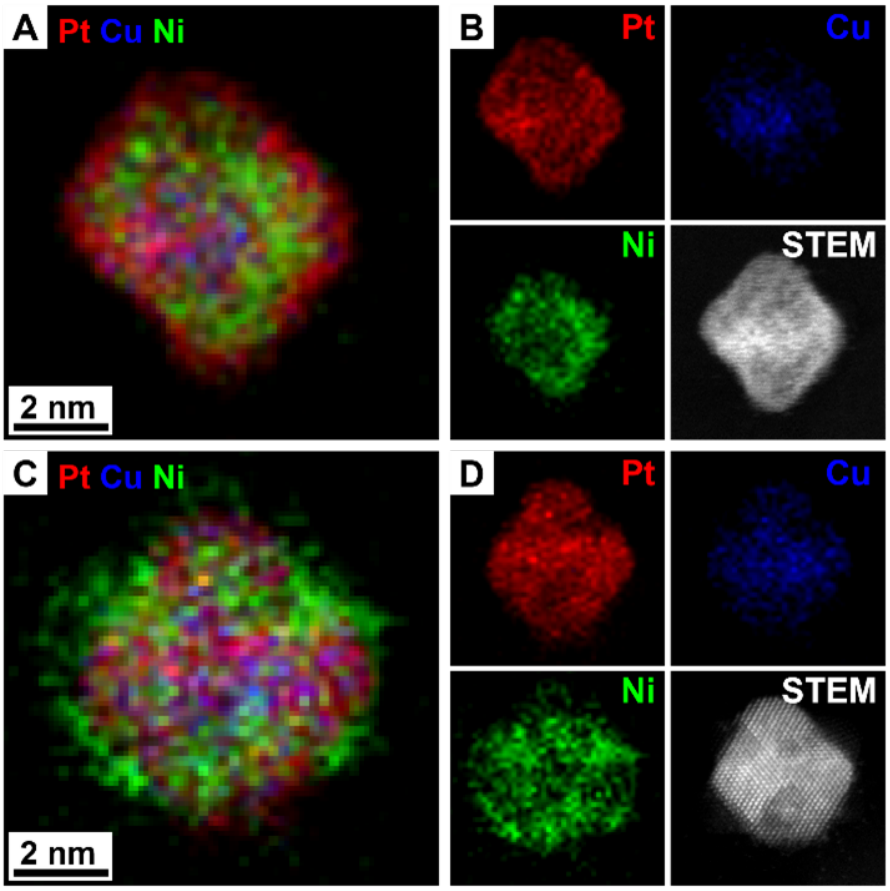

Figure 3.3: EDS maps of elemental components in an octahedral PtNiCu nanoparticle **(A)** overlapped distribution of Pt, Cu, Ni in a single map **(B)** EDS maps of Pt, Cu, Ni separated in individual panels and a HAADF STEM image of the mapped octahedral nanoparticle. EDS maps of elemental components in an octahedral PtNiCu-O nanoparticle **(C)** overlapped distribution of Pt, Cu, Ni in a single map **(D)** EDS maps of Pt, Cu, Ni in separated in individual panels and a HAADF-STEM image of the mapped PtCuNi-O octahedral nanoparticle.

3.3.2 Electrochemical Performance Evaluation

To evaluate the HER performance of our PtCuNi/C and PtCuNi-O/C nano octahedra, the rotating disk electrode (RDE) was used by loading the catalyst onto a glassy carbon disk. The loading of Pt was maintained at 1.3 μg, which was calculated using Pt weight ratio within the catalyst based on inductively coupled plasma atomic emission spectroscopy (ICP-AES). All potentials reported here are versus reversible hydrogen electrode (RHE) if not specified. Current densities are normalized to the geometric area of the working electrode, and iR compensation has been applied to the data if there is no specific note. Cyclic voltammetry (CV) scans were used to activate the catalyst. The HER activities of our catalysts were tested using cyclic sweeping voltammetry (CV) at a sweep rate of 5 mV/s in 1 M KOH. iR compensation was applied in data analysis if not specifically noted. In general, PtCuNi-O/C showed better activity than PtCuNi/C (**Figure 3.4A**), including lower overpotential at the same Pt loading and better mass normalized activity. During the performance evaluation, PtCuNi/C and PtCuNi-O/C showed an average overpotential of 38.8 mV and 31.3 mV at 10 mA/cm^2, respectively. The overpotential of PtCuNi-O/C is dramatically smaller than that of commercial Pt/C (115.2 mV) (**Figure 3.4B**). At an overpotential of 70 mV (-70 mV vs. RHE), the octahedral PtCuNi/C presents a mass activity (MA) of 4.9 mA/μg_{Pt}, while the PtCuNi-O/C demonstrates a MA of 8.7 mA/μg_{Pt}, which is nearly 9.5 folds to that of the commercial Pt/C (0.92 mA/μg_{Pt}) (**Figure 3.4C**). Also, the PtCuNi-O/C can reach a current density of 114 mA/cm^2 at -0.2 V vs. RHE without iR compensation (**Figure 3.4D**), which is well above that of Pt/C (22.4 mA/cm^2), indicating a promising potential for the industrial scale hydrogen production. The stability of catalysts was evaluated via a chronopotentiometry test (**Figure 3.4E**). The working electrode was maintained at 10 mA/cm^2 for 10 hours. Both octahedral PtCuNi/C and PtCuNi-O/C demonstrated significantly higher HER stability compared to the commercial Pt/C. In contrast to the 160.1 mV potential drop for the Pt/C, there was only 55.5 mV, 48.2 mV potential drop for octahedral PtCuNi/C, PtCuNi-O/C, correspondingly (**Figure 3.4F**).

According to EDS, the atomic content of Ni plus Cu dropped from 42.0% to 29.2% and from 42.0% to 35.5% for PtCuNi/C and PtCuNi-O/C after the HER stability test, respectively. The PtCuNi-O/C showed slightly better capability for retaining non-PGM transition metal than PtCuNi/C, which may be attributed to the formation of a better crystalized and more stable NiO structure due to the annealing process.

3.3.3 Lattice Tuning Discussion

The surface NiO islands are formed during the oxidative annealing (**Figure 3.1**), which naturally impacts the HER catalytic performance (**Figure 3.4**). In order to further optimize the catalytic performance, we studied the effect of annealing time on the structure of the catalyst and its corresponding catalytic activity. In our study, we prepared octahedral PtCuNi nanoparticles and octahedral PtNi nanoparticles using a similar solvent thermal synthesis method[13]. PtNi octahedral nanoparticle shows comparable size (octahedral edge length 6.1 ± 0.8 nm) as PtCuNi (octahedral edge length 5.8 ± 0.8 nm). With the increased annealing time, the peaks further shift to lower angles (**Figure 3.5A, Figure 3.6**), and the lattice parameters increase correspondingly. As shown in **Figure 3.6B**, the XRD-based lattice parameter increased from 0.3780 nm to 0.3835 nm, and from 0.3779 nm to 0.3841 nm after 480 minutes annealing for PtNi and PtCuNi nanoparticles, respectively. More specifically, for an annealing time of fewer than 120 minutes, there is an obvious change in lattice parameters, while only a minor change is found when the annealing time is extended beyond 120 minutes. The lattice change due to annealing was also confirmed by the fitted Pt-M (M can be Ni or Cu) scattering length based on extended X-ray absorption fine structure (EXAFS) spectra of PtNi/C, PtCuNi/C, and representative PtNi-O/C, PtCuNi-O/C (**Figure 3.7**). For instance, the fitted Pt-M bond length increased from 0.2618 ± 0.0009 nm to 0.2630 ± 0.001 nm and from 0.2620 ± 0.0008 nm to 0.2630 ± 0.002 nm for PtNi/C and PtCuNi/C, correspondingly (**Figure 3.5C**). At the same time, the Pt-M bond counts, which describes the average number of nearest M metal per Pt atom, decrease from 2.8 to 1.8 and from 3.1

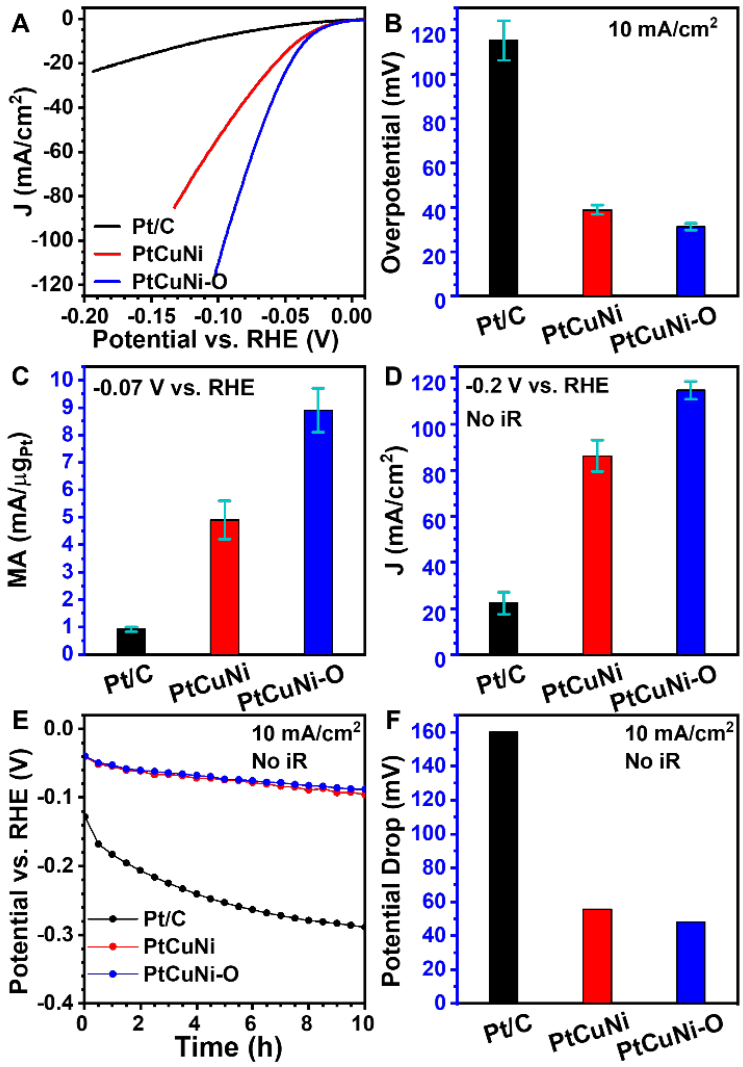

Figure 3.4: Comparison of commercial Pt/C, PtCuNi/C, PtCuNi-O/C **(A)** HER polarization plot **(B)** overpotential at 10 mA/cm^2, **(C)** mass activity at -0.07 V vs. RHE, **(D)** current density at -0.2 V vs. RHE. Comparison of commercial Pt/C, PtCuNi/C, PtCuNi-O/C in stability test **(E)** HER chronopotentiometry curve **(F)** potential drop based on initial and end comparison. All tests were performed in 1M KOH with a rotation rate of 1600 r.p.m. and current densities are normalized to the geometric area of the working electrode. The error bars in all figures of this work represent standard deviation if not specifically noted.

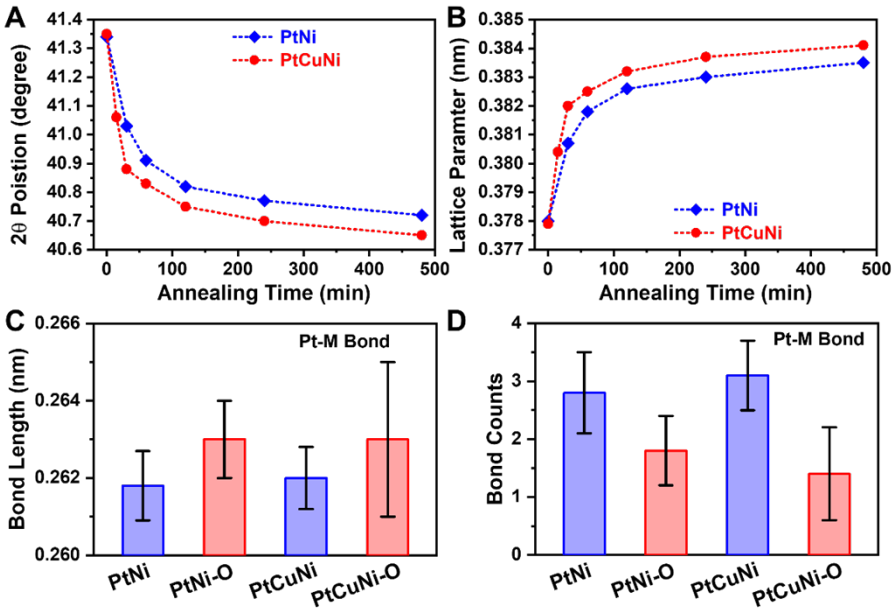

Figure 3.5: XRD and XAS characterization of the dealloying induced structural change. XRD characterization of the dealloying process, **(A)** The relation between the representative (111) peak position and annealing time, **(B)** the relation between lattice parameter and the annealing time. The comparison of PtNi/C, PtCuNi/C and representative PtNi-O/C, PtCuNi-O/C based on EXASF data, **(C)** Pt-M bond length, **(D)** Pt-M bond counts.

to 1.4 due to the dealloying process of PtNi and PtCuNi nanoparticles, respectively (**Figure 3.5D**).

We further characterized the representative PtNi-O/C and PtCuNi-O/C nanocatalysts. The high angle annular dark field (HAADF) scanning transmission electron microscopy (STEM) and the atomic resolution HAADF-HRSTEM image reveal that the average (200) lattice spacing of PtNi-O nanoparticle is 0.191 nm, corresponding to a lattice parameter of 0.382 nm for the core of nanoparticle, given the fcc structure (**Figure 3.8A**). Similarly, for the PtCuNi-O nanoparticle, the observed average (111) interplane distance is 0.221 nm (**Figure 3.8A**), corresponding to a lattice parameter of 0.383 nm based on its fcc packing. Also, NiO islands, which consist of 3-4 NiO (111) layers (marked with yellow in **Figure 3.8**),

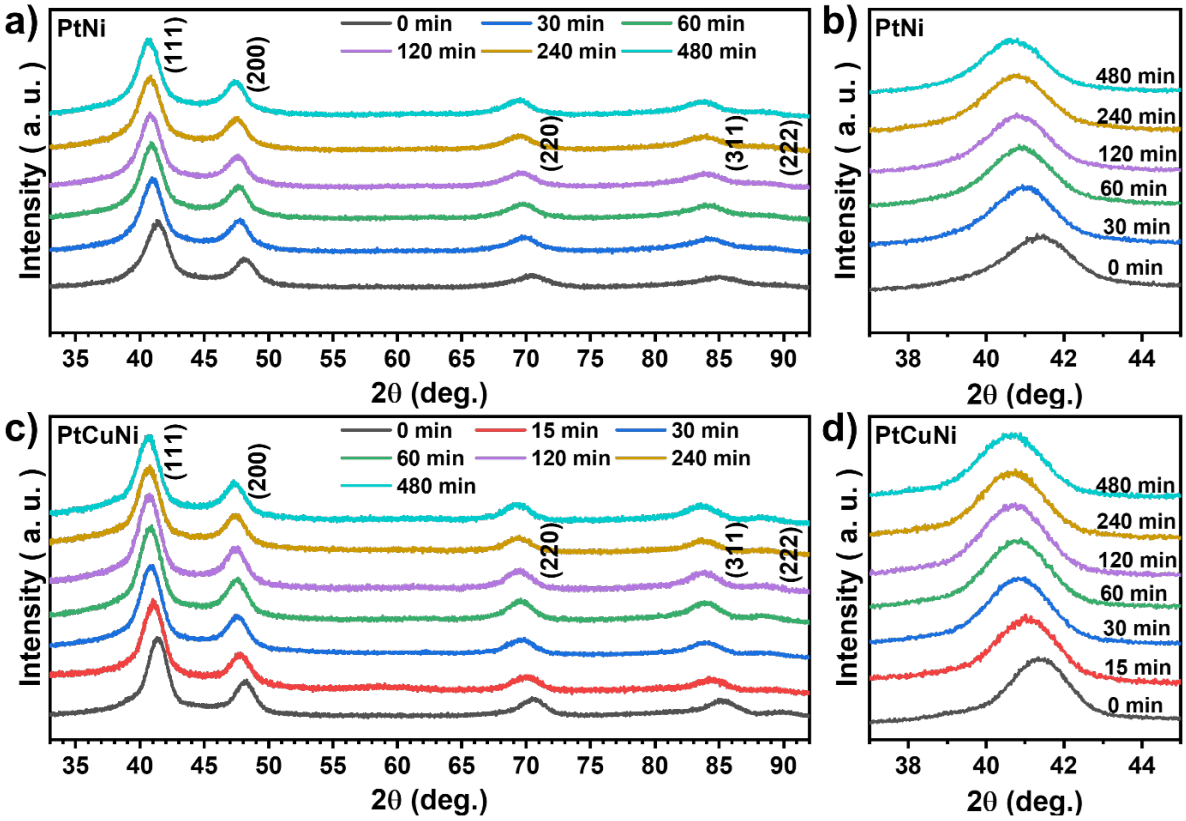

Figure 3.6: XRD Characterization of nanocatalysts. **(A)** PtNi annealed at 160 °C air with a series of time. **(B)** zoom in of **A**. **(C)** PtCuNi annealed at 200 °C air with a series of time. **(D)** zoom in of **(C)**.

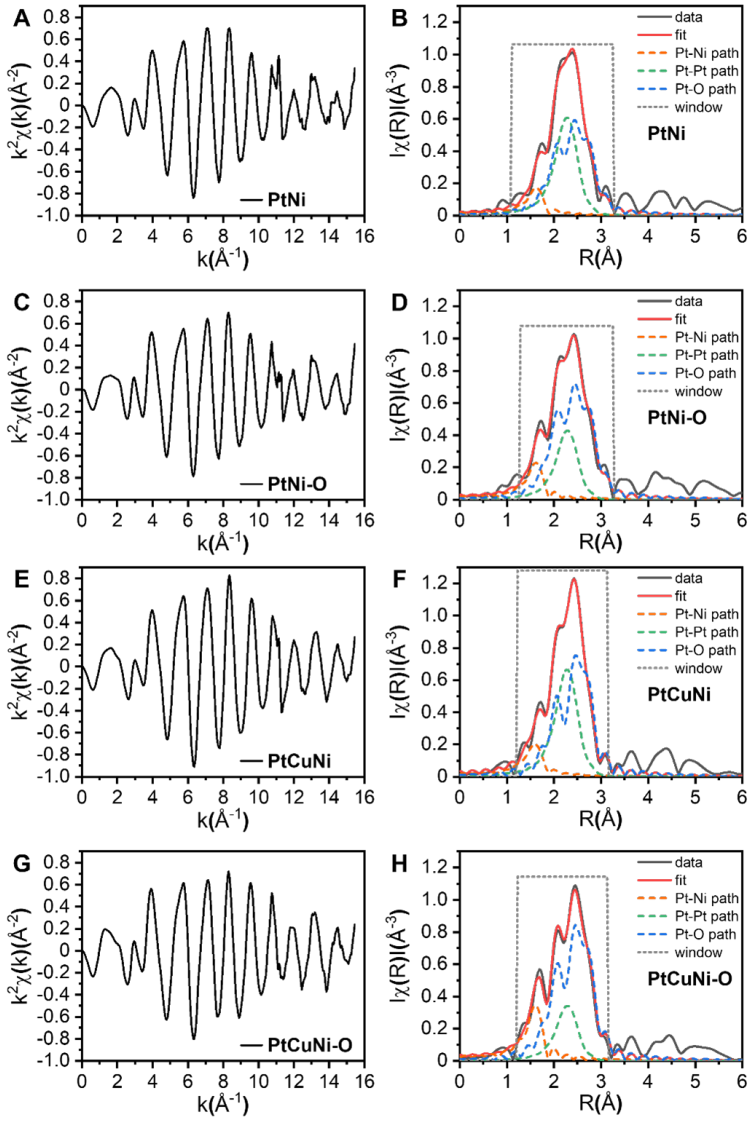

Figure 3.7: FT-EXAFS spectra and fittings at the Pt L_3-edge of **A, (B)** PtNi/C, **C, (D)** PtNi-O/C, **(E, F)** PtCuNi/C, **(G, H)** PtCuNi-O/C. The FT-EXAFS spectra are not phase-corrected for showing the original data. S_0^2 was fixed at 0.83 as obtained by fitting the reference foil. Fits were done in the R-space with k1,2,3 weighting. The windows of $1.12 < R < 3.31$ Å and $\Delta k = 3.0 - 14.6$ Å^{-1} were used for fitting. The fitting results of the E_0 are 6.4 ± 0.7 eV and 5.7 ± 0.6 eV for PtNi-O and PtCuNi-O, respectively. Raw $k^2\chi(k)$(Å^{-2})

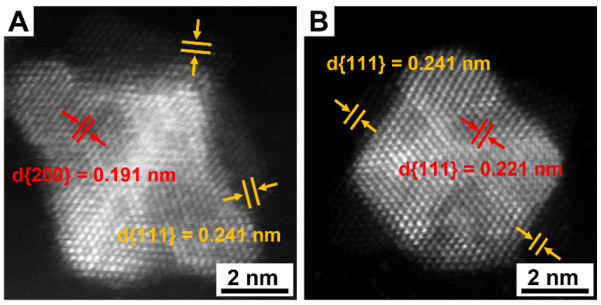

Figure 3.8: STEM characterization of PtNi-O and PtCuNi-O octahedral nanoparticles. Atomic resolution HAADF STEM images **(A)** PtNi-O/C, **(B)** PtCuNi-O/C.

are observed on the surface of the PtNi-O/C and PtCuNi-O/C nanoparticles. The observation of NiO surface islands can be supported by the energy dispersive spectroscopy (EDS) maps (**Figure 3.3A**). Based on XRD spectra, STEM images, and EDS maps, we further confirmed that, for both PtNi-O and PtCuNi-O, Ni is mainly distributed on the surface of the nanoparticle, Pt is located at the relatively central part, and Cu is more concentrated at the center. Both PtNi-O/C and PtCuNi-O/C octahedral nanoparticles consist of Pt alloy cores and NiO surface islands. This observation matches well with the XPS spectra that present obvious NiO peaks, which suggests the surface enrichment of NiO through the oxidative annealing process.

Furthermore, the relationship of the hydrogen evolution reaction (HER) mass activity with the lattice parameter was studied (**Figure 3.9**). To compare the HER performance of the PtNi/C and PtCuNi/C with different annealing time, a rotating disk electrode (RDE) system was used for the HER test. For a fair comparison, we followed the same test protocol for all prepared catalysts. Among all samples, the PtNi-O/C annealed for 120 mins presented the highest mass activity (MA) of 9.1 $\pm$ 0.6 mA/μg_{Pt} at an overpotential of -0.07 V (**Figure 3.9A**). The PtCuNi-O/C annealed for 120 mins showed the highest MA of 8.7 $\pm$ 0.8 mA/μg_{Pt} among all PtCuNi-O/C samples (**Figure 3.9A**). The PtNi-O/C and PtCuNi-O/C showed similar trends and presented the highest mass activity at a lattice parameter between 0.3825 to 0.3835 nm (**Figure 3.9B**). The representative PtNi-O and PtCuNi-O (annealed for

120 min) catalysts show 9.9-fold and 9.5-fold MA compared to Pt/C (0.92mA/μg_{Pt}), respectively (**Figure 3.9C**). In order to study the stability of the developed material, the working electrode was maintained at 10 mA/cm^2 for 10 hours. PtCuNi-O/C demonstrated slightly better durability over PtNi-O/C and obviously superior stability over the commercial Pt/C (**Figure 3.9D**). The EDS analysis reveals that there is only a small drop of Ni content for PtNi-O/C (47.1% to 42.5%) and PtCuNi-O/C (37.3% to 29.1%) before and after the stability test. Comparing the TEM images, both PtNi-O/C and PtCuNi-O/C demonstrate neither significant aggregation nor morphology change of nanoparticles before and after the stability test, while Pt/C shows apparent particle aggregation (**Figure 3.10**). In the EDS maps, Ni remains enriched on the surface of representative PtNi-O/C and PtCuNi-O/C nanoparticles after the stability test (**Figure 3.11**). Thus, there is no significant change in the elemental distribution for PtNi-O/C and PtCuNi-O/C before and after the stability test (**Figure 3.3, 3.11**).

The overall composition for Pt-based catalysts is maintained the same assuming no metal loss during the annealing process. In addition, we further analyzed the surface composition evolution during the annealing process based on XPS spectra (**Figure 3.12, 3.13, Table 3.1**). The ratio of non-precious group metal (Ni and Cu) to platinum is estimated for PtNi-O and PtCuNi-O annealed at different lengths of time (**Table 3.1**). By plotting the obtained MA of the annealed catalysts in HER versus the surface (Ni+Cu)/Pt ratio, it is found that further increasing the annealing time of PtCuNi-O/C from 240 min to 480 min leads to no further increase of surface (Ni+Cu)/Pt ratio while the HER MA of PtCuNi-O decrease. Also, the surface (Ni+Cu)/Pt ratios associated with the best performance of PtNi-O/C and PtCuNi-O/C are 1.53 and 1.31, respectively (**Table 3.1**). In contrast, **Figure 3.9B** shows that the trend of MA in the HER test versus lattice parameter obtained from XRD is quite similar for both PtNi-O/C and PtCuNi-O/C catalysts. The lattice parameters associated with the PtNi-O/C and PtCuNi-O/C show the best MA fall within the region of 0.3825-0.3835 nm (**Figure 3.9B, Table 3.2**). Thus, tuning the lattice parameter is critical for

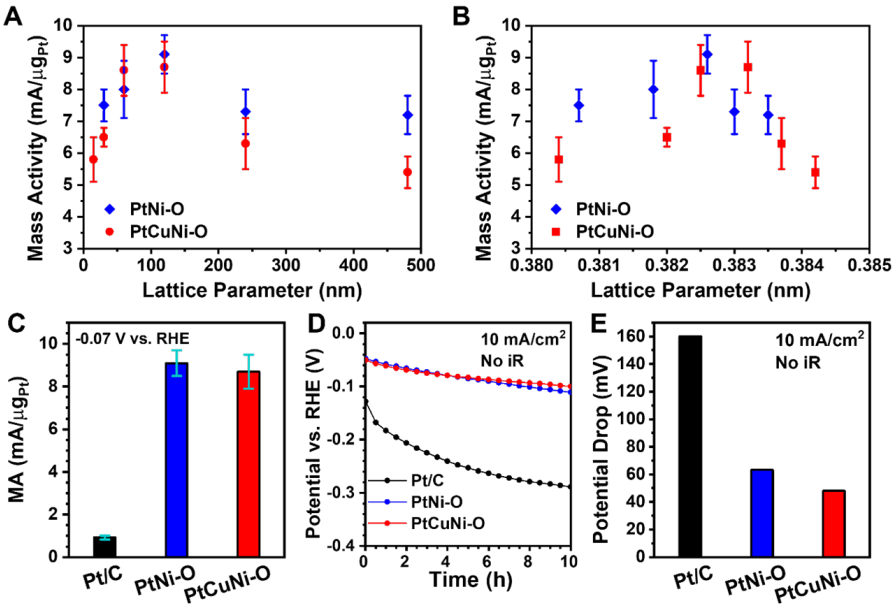

Figure 3.9: HER test of prepared catalysts. Comparison of HER mass activity of PtNi-O/C and PtCuNi-O/C annealed at different periods of time, **(A)** relationship between mass activity and annealing time **(B)** relationship between mass activity and lattice parameter. **(C)** commercial Pt/C, representative PtNi-O/C, and PtCuNi-O/C. **(D)** HER chronopotentiometry plot for stability test, **(E)** potential drop based on initial and end comparison. All the performances were evaluated in 1 M KOH. The stability test is maintained at a constant current density 10 mA/cm^2.

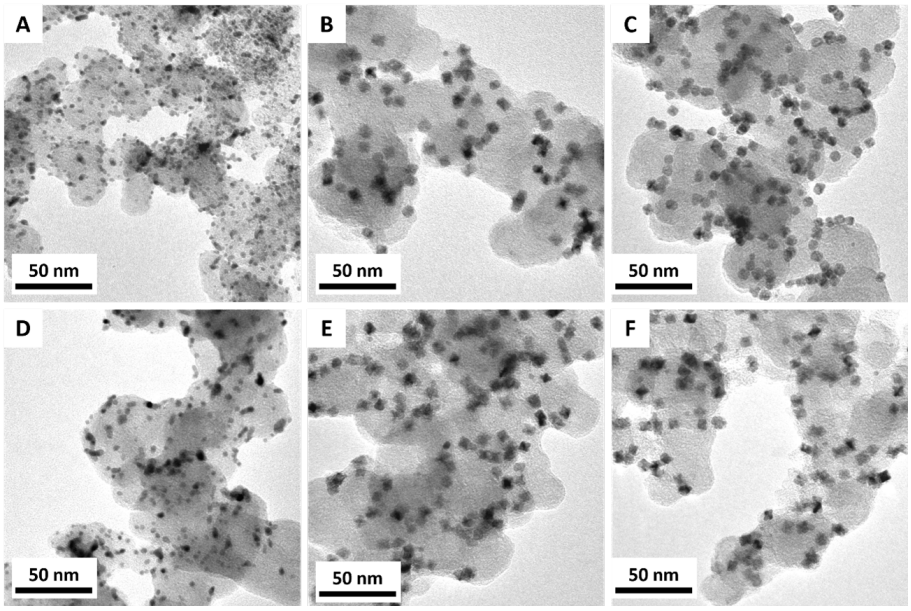

Figure 3.10: TEM images of materials before HER durability test **(A)** Pt/C, **(B)** octahedral PtNi-O/C, **(C)** octahedral PtCuNi-O/C, after HER stability test **(D)** Pt/C, **(E)** octahedral PtNi-O/C, **(F)** octahedral PtCuNi-O/C.

optimizing the HER performance of Pt-based catalysts.

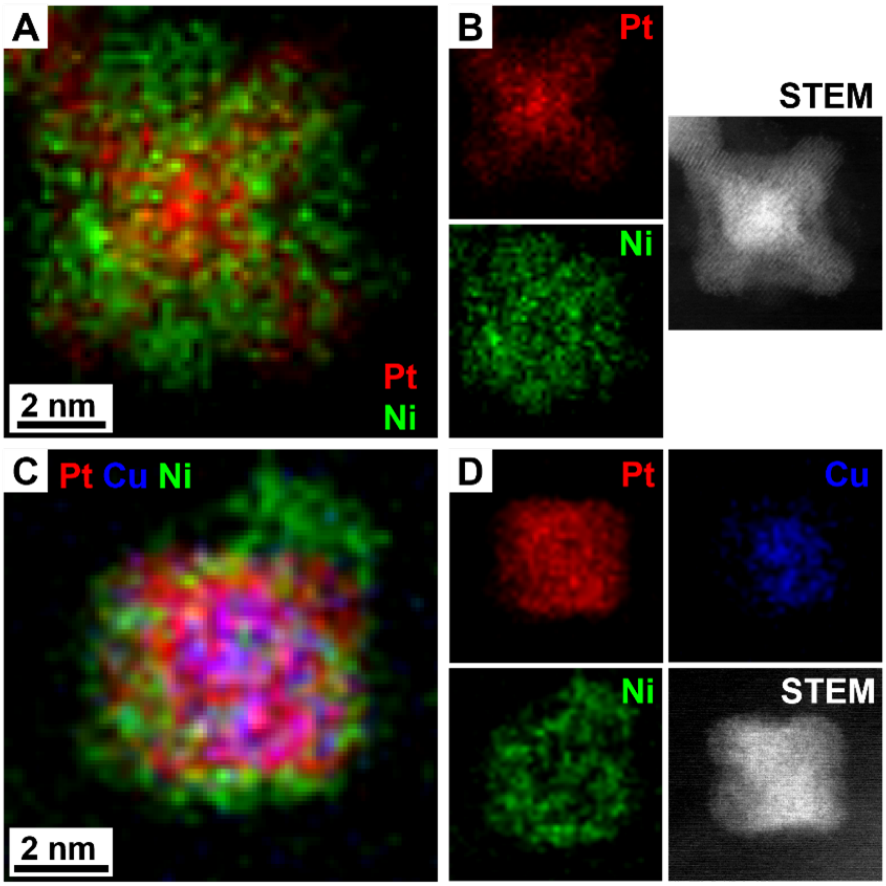

Figure 3.11: EDS maps of elemental components in a representative PtNi-O octahedral nanoparticle after HER stability test **(A)** overlapped distribution of Pt, Ni in a single map **(B)** EDS maps of Pt, Ni in separated panels and a HAADF STEM image of the mapped PtNi-O octahedral nanoparticle. EDS maps of a representative PtCuNi-O octahedral nanoparticle after HER stability test **(C)** overlapped distribution of Pt, Cu, Ni in a single map **(D)** EDS maps of Pt, Cu, Ni in separated panels and a HAADF STEM image of the mapped PtCuNi-O octahedral nanoparticle.

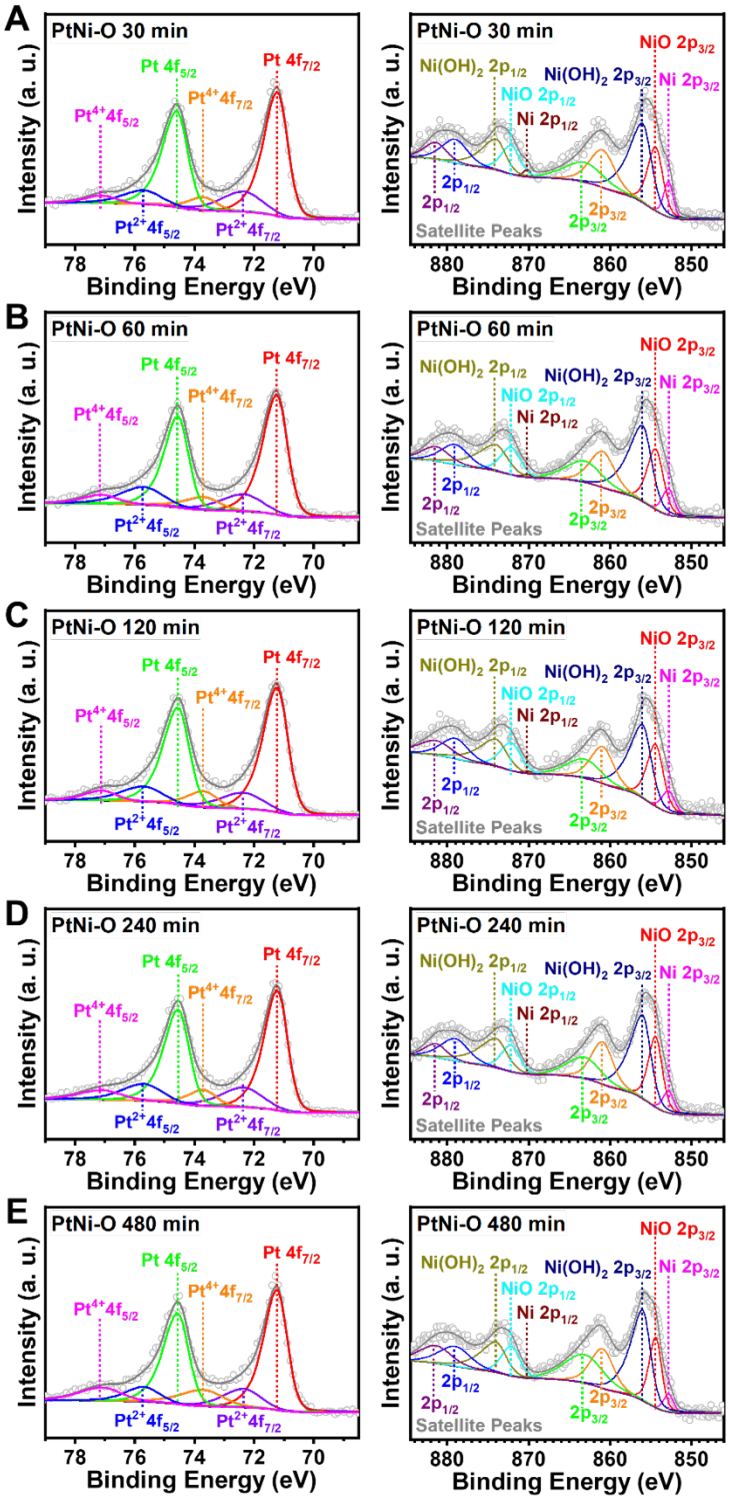

Figure 3.12: XPS spectra of Pt 4f and Ni 2p for PtNi-O annealed at 160 °C in air for **(A)** 30 min, **(B)** 60 min, **(C)** 120 min, **(D)** 240 min, **(E)** 480 min.

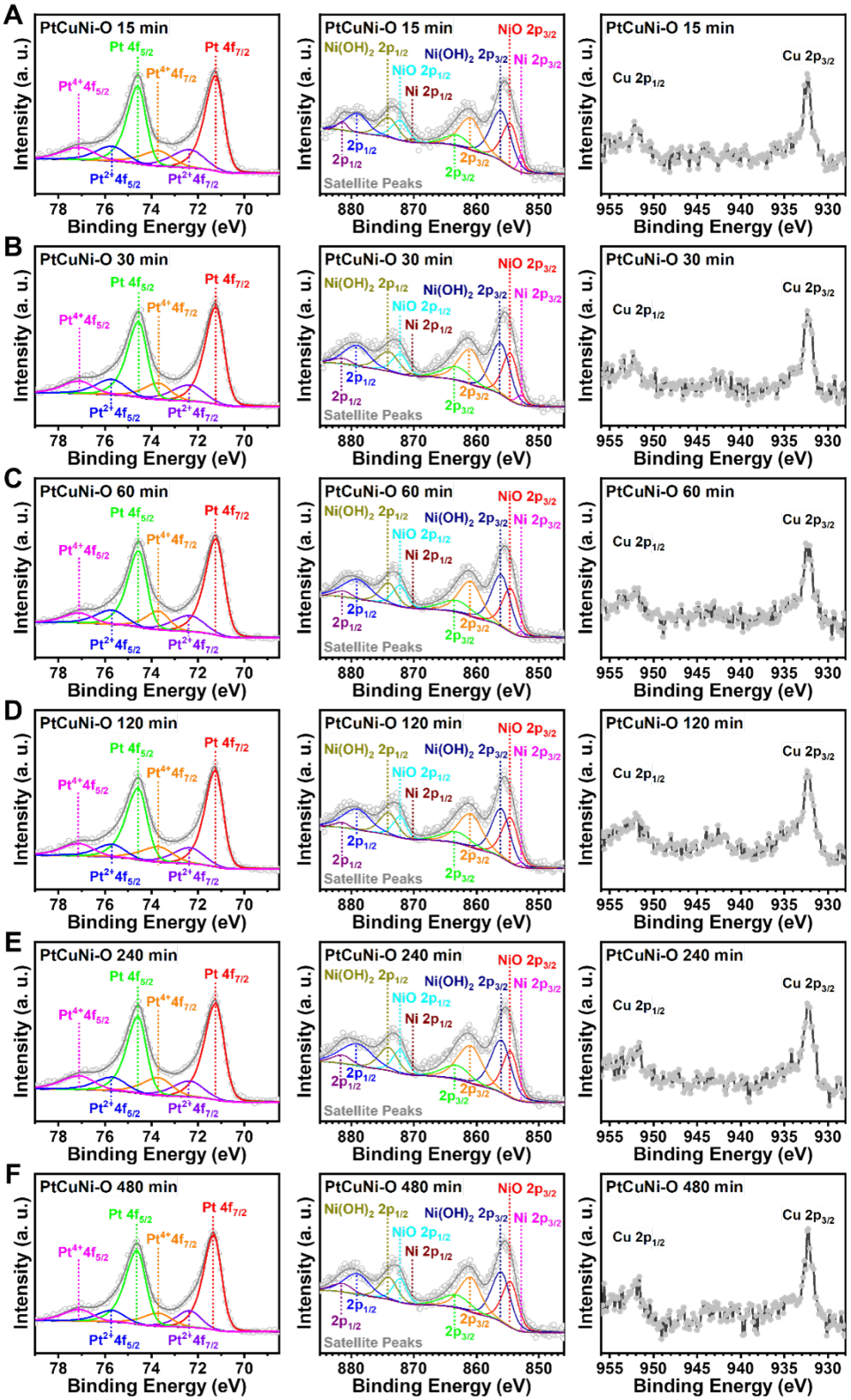

Figure 3.13: XPS spectra of Pt 4f, Ni 2p, and Cu 2p for PtCuNi-O annealed at 200 °C in air for **(A)** 15 min, **(B)** 30 min, **(C)** 60 min, **(D)** 120 min, **(E)** 240 min, **(F)** 480 min.

Table 3.1: Comparison of PtCuNi/C, PtCuNi-O/C, PtNi/C, and PtNi-O/C for the surface ratio of non-platinum group metal (Ni+Cu) to platinum at different annealing time. The metal ratio estimation is based on the integration of peak area in XPS spectra.

Sample	**Annealing Time (min)**	**XPS ratio of Ni/Pt**	**XPS ratio of (Ni+Cu)/Pt**
PtNi/C	0	1.02	1.02
PtNi-O/C	30	1.35	1.35
PtNi-O/C	60	1.49	1.49
PtNi-O/C	120	1.53	1.53
PtNi-O/C	240	1.59	1.59
PtNi-O/C	480	1.68	1.68
PtCuNi	0	0.53	0.56
PtCuNi-O/C	15	1.08	1.12
PtCuNi-O/C	30	1.16	1.19
PtCuNi-O/C	60	1.21	1.25
PtCuNi-O/C	120	1.27	1.31
PtCuNi-O/C	240	1.29	1.33
PtCuNi-O/C	480	1.29	1.33

Table 3.2: Comparison of PtNi-O/C, PtCuNi-O/C nanocatalysts in terms of annealing time, (111) peak position for octahedral nanoparticles in XRD spectrum, lattice parameter based on XRD, shortest atomic distance based on lattice parameter, HER mass activity at -0.07 V vs. RHE.

Sample	**Annealing Time(min)**	**The (111) Peak at 2θ (degree)**	**Lattice Parameter (nm)**	**Shortest Atomic Distance (nm)**	**Mass Activity ($mA/\mu g_{Pt}$)**
PtNi-O/C	30	41.03	0.3807	0.2692	7.5 ± 0.5
PtNi-O/C	60	40.91	0.3818	0.2700	8.0 ± 0.9
PtNi-O/C	120	40.82	0.3826	0.2705	9.1 ± 0.6
PtNi-O/C	240	40.77	0.3830	0.2708	7.3 ± 0.7
PtNi-O/C	480	40.72	0.3835	0.2712	7.2 ± 0.6
PtCuNi-O/C	15	41.06	0.3804	0.2690	5.8 ± 0.7
PtCuNi-O/C	30	40.88	0.3820	0.2701	6.5 ± 0.3
PtCuNi-O/C	60	40.83	0.3825	0.2705	8.6 ± 0.8
PtCuNi-O/C	120	40.75	0.3832	0.2710	8.7 ± 0.8
PtCuNi-O/C	240	40.70	0.3837	0.2713	6.3 ± 0.8
PtCuNi-O/C	480	40.65	0.3841	0.2716	5.4 ± 0.5

3.4 Conclusion

In this study, we report a way of further optimizing the HER performance of highly active Pt-based nanocatalysts by tuning their lattice parameter. We found that the dealloyed nanocatalysts showed the best performance when the lattice parameter was in the range of 0.3825-0.3835 nm for both PtNi-O/C and PtCuNi-O/C. The optimized PtNi-O/C demonstrated a mass activity of 9.1 $mA/\mu g_{Pt}$, which is 9.9-fold compared to that of Pt/C. The reported PtNi-O/C is one of the best Pt-based HER catalysts, with mass activity only surpassed by SANi-PtNWs[41]. To sum up, we demonstrated a way to further improve HER efficiency by tuning the lattice of Pt-based nanocatalyst, which can potentially reduce the operational cost of industrial electrolyzer further and enhance the efficiency of renewable energy storage.

3.5 Author Contribution

Zipeng Zhao proposed the idea of PtNi alloy, provided the original synthetic recipe, and conducted the corresponding characterization. Haotian Liu proposed the idea of Ni enrichment and Cu lattice tuning on the surface, improved the synthetic recipe, and conducted the corresponding characterization. Wenpei Gao and Xiaoqing Pan provided support on HRSTEM image acquisition. Wang Xue, Zeyan Liu, and Jin Huang provided support for other characterizations. Yu Huang proposed the idea and instructed the experiments.

CHAPTER 4

Unveiling the Structure-Activity Relationships for Cobalt-based Spinel Oxide with Superior Acidic OER Performance

4.1 Background

Note: this is a version of a paper in preparation.

Carbon neutrality is one of the most critical priorities for the twenty-first century.[42,43,44] Society must discover ecologically benign energy sources to replace fossil fuels and cut net CO_2 emissions significantly to attain carbon neutrality. Molecular hydrogen stands out among the many possible energy sources due to its high gravimetric energy density[45] and the lack of harmful byproducts during energy conversion. However, the most efficient industrial method for hydrogen production is the steam reforming of natural gas,[45] which is energy-intensive and produces CO_x and NO_x pollutants. Water electrolysis is a most attractive alternative for clean hydrogen production because oxygen and water vapor are the only byproducts, and the energy source can be renewable (such as solar, geothermal, or biomass).[46] Ideally, water electrolysis would be more effective in acidic environments. Platinum's electrochemical hydrogen evolution activity is approximately two orders of magnitude more active in acidic than alkaline conditions.[25,47] In addition, the proton exchange membrane water electrolyzer, featuring acidic conditions, receives intensive attention over the alkaline electrolyzer because the former produces pure hydrogen at a higher current density

and higher voltage efficiency.[12,48] In acidic environments, the anode catalysts are Ru or Ir-based catalysts,[49] which suffer from high price and poor longevity in acidic environments.[50] Finding a low-cost, efficient, and durable catalyst for the acidic oxygen evolution reaction (OER) can drastically cut the cost of water electrolysis.

Non-noble-metal-based catalysts, including unary metal oxides,[51,52] polymetallic oxides,[53,54] and polyoxometalates,[55] showed potential for acidic OER. The spinel Co_3O_4 attracts attention because of its facile synthetic strategy, high activity, and good acid resistance.[56,57,58] However, the activity of Co_3O_4 needs to be improved due to the notable performance gap between Co_3O_4 and RuO_2.[56] Decorating Co_3O_4 with other non-noble transition metals is an effective method to improve the OER performance, which brings higher electrical conductivity and lower kinetic barrier towards OER in alkaline conditions.[59,60,61] Nevertheless, employing a similar design strategy while maintaining the acidic corrosion resistivity and high activity for acidic OER can be challenging.

Adsorbate evolution mechanism (AEM) is widely studied as the OER mechanism, involving O*, OH*, and OOH* intermediates during the catalytic cycle.[62] A stringent scaling relationship demonstrates the linear-correlated binding energy of the intermediates.[63] Therefore, the binding energy cannot be individually tuned. However, some recent works reported that catalysts could overcome the theoretical free energy limit between OH* and OOH* ($\Delta G_{OH^*}=\Delta G_{OOH^*} + 3.2 \pm 0.2$ eV)[64,65] ruled by scaling relationship,[66,67,68] indicating that there are possible alternative mechanisms involved other than AEM. Lattice oxygen evolution mechanism (LOM) and direct O-O coupling (DOC) mechanism are widely demonstrated in recent studies. LOM delivers a high activity but poor stability due to the *in situ* formation of oxygen vacancies in the oxides.[69,70] Whereas the direct O-O coupling (DOC) mechanism is optimal because the oxides have no structural change during the catalytic cycle.[71] Two oxygen-containing intermediates adsorbed on adjacent metal atoms couple and form oxygen molecules without OOH* involved. Thus the scaling relationship can be broken. Nevertheless, DOC mechanism has a strict requirement on the geometrical configuration of the

crystal structure.[67,68] However, designing a non-noble-metal-based spinel oxide structure that facilitates acidic OER by employing DOC mechanism has seldom been reported.

Here, we report a cobalt-based spinel oxide structure (MCo_2O_4, M = Mn, Ni, Co, Cu) following DOC mechanism requirements with ultrahigh acidic OER activity and exceptional stability. We showed that decorating the spinel cobalt oxides with other transition metals (Mn, Ni, Cu) could enhance the OER activity and durability. Among decorated spinel oxides, $NiCo_2O_4$ showed the highest acidic OER activity demonstrating an overpotential of 407 mV at 100 mA/cm^2 in 0.5 M H_2SO_4. $NiCo_2O_4$ also exhibited superior OER durability in 0.5 M H_2SO_4 with an overpotential increase of 68.9 mV at 10 mA/cm^2 and 98.6 mV at 100 mA/cm^2 after 20 hours of chronopotentiometry test. X-ray absorption spectroscopy (XAS) studies demonstrated that Ni occupies the octahedral site predominantly. *In situ* XAS revealed that adding Ni to the structure resulted in less structural change during the OER process, which was the source of $NiCo_2O_4$'s higher endurance. DFT calculations on the (110) facet of $NiCo_2O_4$ and Co_3O_4 indicate that OER in acidic conditions undergoes the DOC mechanism as opposed to the water nucleophilic attack AEM that we found for many other systems[72,73,74]. Our DFT calculations indicate that the $NiCo_2O_4$ (110) surface has an overpotential towards OER that is 90 mV lower than that for the Co_3O_4 (110) surface, which is consistent with the experimental difference of 67 mV.

4.2 Materials and Methods

4.2.1 Chemicals and Materials

Cobalt(II) chloride hexahydrate [$CoCl_2{\cdot}6H_2O$, ACS Reagent, 98%], nickel(II) chloride hexahydrate [$NiCl_2{\cdot}6H_2O$, ReagentPlus], ammonium fluoride [NH_4F, ACS Reagent, $\geq$ 98.0%], urea [$CO(NH_2)_2$, ReagentPlus, $\geq$ 99.5%, pellets], ruthenium(IV) oxide (RuO_2, 99.9% trace metals basis), sulfuric acid (H_2SO_4) were purchased from Sigma Aldrich. Ethanol (200 proof) was obtained from Decon Labs, Inc. Acetone ($\geq$ 99.5%) and isopropanol ($\geq$ 99.5%) were

purchased from Fisher Chemical. All reagents were used as received without further purification. The carbon fiber paper (AvCarb MGL370) was purchased from Fuel Cell Store. The deionized water (18 MΩ/cm) was obtained from an ultra-pure purification system (Milli-Q advantage A10).

4.2.2 Pretreatment of Carbon Fiber Paper (CFP)

The CFP was washed and sonicated in ethanol and water several times to removed surface impurities. Then the CFP was oxidized in 0.5 M H_2SO_4 via cyclic voltammetry from 1.8 V to 2.3 V at a sweep speed of 100 mV/s for 40 cycles. This step is to further clean the CFP's surface and improve its hydrophilicity. The oxidized CFP was washed and sonicated in water 3 times and ready for use.

4.2.3 Synthesis of Hierarchical Spinel Cobalt Oxide (Co_3O_4) on CFP

The hierarchical MCo_2O_4 was synthesized via a facile hydrothermal method adjusted from previous literature[75] and directly grown on CFP. Typically, 3 mmol of $CoCl_2{\cdot}6H_2O$, 4 mmol of NH_4F, and 10 mmol of urea were dissolved in 13 mL of water and sonicated for 5 mins until the solution was clear. The solution was then transferred into a 20-mL Teflon shell. The CFP was placed in the shell, and the shell was placed in a stainless-steel autoclave. The autoclave was kept at 120 ℃ for 12 hours and cooled down naturally. The loaded CFP was then washed with water and ethanol 3 times, respectively, and dried in vacuum at room temperature. After the loaded CFP was fully dried, it was annealed in a tube furnace at 350 ℃ for 3 hours and cooled down naturally. Now the Co_3O_4 on CFP is ready to use.

4.2.4 Synthesis of Hierarchical Cobalt-based Spinel Oxide (MCo_2O_4, M = Mn, Ni, Cu) on CFP

The hierarchical MCo_2O_4 was synthesized via a facile hydrothermal method and directly grown on CFP. Typically, for the synthesis of $NiCo_2O_4$, 2 mmol of $CoCl_2{\cdot}6H_2O$, 1 mmol of $NiCl_2{\cdot}6H_2O$, 4 mmol of NH_4F, and 10 mmol of urea were dissolved in 13 mL of water and sonicated for 5 mins until the solution was clear. The solution was then transferred into a 25-mL Teflon shell. The CFP was placed in the shell, and the shell was placed in a stainless-steel autoclave. The autoclave was kept at 130 ℃ for 12 hours and cooled down naturally. The loaded CFP was then washed with water and ethanol 3 times, respectively, and dried in vacuum at room temperature. After the loaded CFP was fully dried, it was annealed in a tube furnace at 350 ℃ for 3 hours and cooled down naturally. Now the $NiCo_2O_4$ on CFP is ready to use. For $MnCo_2O_4$ and $CuCo_2O_4$ on CFP, the synthetic route is very similar except that the $NiCl_2{\cdot}6H_2O$ was substituted by $MnCl_2{\cdot}4H_2O$ and $CuCl_2{\cdot}2H_2O$.

4.2.5 XAS Study Sample Preparation

4.2.5.1 For *ex situ* Test

The original catalyst loaded on CFP was directly used for the XAS study. For after-CV samples, the CV was conducted between 1500 mV and 1700 mV in 0.5 M H_2SO_4 at a sweep rate of 100 mV/s for designated cycles (10, 50, 100, and 500 cycles). After the CV was finished, the sample was washed with water several times to remove the acid residue. Then the sample was dried in vacuum and ready for the XAS test.

4.2.5.2 For *in situ* Test

Before the *in situ* XAS test, the catalyst was washed with water and placed in 0.5 M H_2SO_4, and then a CV between 1500 mV and 1700 mV was conducted at a sweep rate of 100 mV/s

for 10 cycles until stable. Subsequently, the *in situ* XAS test was conducted in 0.5 M H_2SO_4 at 1.65 V vs. RHE.

4.2.6 Characterization

Transmission electron microscopy (TEM) images were taken on an FEI T12 operated at 120 kV. Scanning transmission electron microscopy (STEM) images were taken on an FEI TITAN operated at 200 kV, and energy-dispersive X-ray spectroscopy (EDS) spectra were measured on an FEI TITAN operated at 200 kV. Atomic resolution high angle annular dark field (HAADF) STEM images and EDS mapping were taken on a JEOL Grand ARM300CF TEM/STEM operated at 300 kV. Samples for TEM measurements were prepared by dropping 10 μL Pt-based octahedra isopropanol dispersion onto carbon-coated copper grids (Ladd Research, Williston, VT) using a pipette and then drying under ambient conditions. Al grids or Au grids (Ted Pella, Redding, CA) were used for the EDS sample preparation. Powder X-ray diffraction patterns (PXRD) were collected on a Panalytical X'Pert Pro X-ray Powder Diffractometer with Cu-Kα radiation. The composition of catalysts was determined by inductively coupled plasma atomic emission spectroscopy (ICP-AES, Shimadzu ICPE-9000) as well as EDS. X-ray photoelectron spectroscopy (XPS) tests were done with Kratos AXIS Ultra DLD spectrometer with Al Kα (1486.6 eV) X-ray source in the University of California, Los Angeles (UCLA). For the sample Co_3O_4 and $NiCo_2O_4$, the Co and Ni K-edge x-ray absorption near edge spectroscopy (XANES) and extended x-ray absorption fine structure (EXAFS) spectra were collected at beamlines ISS 6-BM and 8-ID at the National Synchrotron Light Source II (Brookhaven National Laboratory, NY). The *in situ* XAS experiments were conducted at room temperature in a previously described *in situ* spectro-electrochemical half cell in which a continuously O_2-purged 0.5 M H_2SO_4 aqueous solution was circulated[76], at beamlines ISS 6-BM and 8-ID at the National Synchrotron Light Source II (Brookhaven National Laboratory, NY).

4.2.7 Electrochemical Test

The cobalt-based spinel oxide catalyst on CFP (MCo_2O_4/CFP) was directly used for electrocatalytic tests without further treatments. As the catalyst was directly grown on CFP, catalyst binders such as Nafion are not needed. The catalyst loading was $\sim$ 3 mg/cm^2 on CFP, which was estimated by ICP-AES for all samples. The catalyst was briefly washed with water before each test.

All electrochemical tests were carried out on a three-electrode cell from Pine Research Instrumentation. The working electrode was the CFP loaded with the corresponding catalyst. The reference electrode was an Ag/AgCl electrode from CH Instrument. The reference electrode was calibrated in a hydrogen-saturated 0.5 M H_2SO_4 solution using Pt wire as both working and counter electrode. The CV test was conducted and the potential for 0 current is the reference potential vs. reversible hydrogen electrode (RHE). A Pt coil was used as the counter electrode. The acidic electrolyte solutions (0.5 M H_2SO_4) were saturated with oxygen. Cyclic voltammetry (CV) was conducted in each solution between 1500 mV to 1700 mV vs. Reverse Hydrogen Electrode (RHE) at a sweep rate of 100 mV/s for 10 cycles before oxygen evolution reaction (OER) tests. OER was tested between 1100 mV to 1830 mV vs. RHE in each solution using linear sweep voltammetry (LSV) at a sweep rate of 10 mV/s. The impedance of each solution was tested on a Princeton VersaSTAT 4 electrochemistry workstation. The solution resistance measured via impedance test was around 2.5 Ω in 0.5 M H_2SO_4. The above values are used for post-test iR correction. The stability of the catalyst is evaluated via chronopotentiometry (CP) test at a current density of 10 mA/cm^2 in 0.5 M H_2SO_4.

4.3 Results and Discussion

Hierarchical MCo_2O_4 (M = Mn, Co, Ni, Cu) on carbon fiber paper with a high surface area is typically synthesized using a hydrothermal-annealing method which we have modified

from a previous report on Co_3O_4 synthesis (**Figure 4.1**).[75] The as-synthesized MCo_2O_4 is ready for use without further modification. **Figure 4.1A** depicts a schematic illustration of the hierarchical structures of $NiCo_2O_4$. With *in situ* growth on the carbon fiber paper, $NiCo_2O_4$ displayed a flower-like structure, with each branch composed of nanoparticles. Based on the scanning electron microscopy (SEM) images (**Figure 4.1B, C**), the flower-like structure has an average size of approximately 12 μm. Moreover, the transmission electron microscopy (TEM) image shows that the 15-nanometer nanoparticles form the branches of this hierarchical structure (**Figure 4.1D**). From the energy dispersive spectroscopy (EDS) mapping, Ni, Co, and O were evenly distributed across the hierarchical structure (**Figure 4.2** and **Figure 4.3**). The high-resolution transmission electron microscopy (HRTEM) image reveals a lattice spacing of 0.245 nm, which corresponds well with the $NiCo_2O_4$ (311) facet lattice spacing (**Figure 4.1E**). As shown in **Figure 4.1F**, the diffraction peaks of $NiCo_2O_4$ coincide well with those of the cubic spinel structures (Fd-3m), with the main peak at $\sim$ 36.7°. The peaks at 25.8°, 42.4°, and 53.5° are attributable to the carbon fiber paper (**Figure 4.4**). Co_3O_4, $MnCo_2O_4$, and $CuCo_2O_4$ also exhibited similar crystal structures according to corresponding XRD patterns (**Figure 4.5**). The SEM-EDS mapping showed that the elements were evenly distributed throughout the structure (**Figure 4.6**, **Figure 4.7**, and **Figure 4.8**). SEM and TEM images showed that $NiCo_2O_4$ and Co_3O_4 had similar flower-like hierarchical structures (**Figure 4.2C, D**, and **Figure 4.9**).

X-ray photoelectron spectroscopy (XPS) was utilized for surface analysis of $NiCo_2O_4$ and Co_3O_4 (**Figure 4.10**). The predominant surface oxidation states of cobalt in $NiCo_2O_4$ and Co_3O_4 are Co^{2+} and Co^{3+}, and the predominant surface oxidation states of nickel in $NiCo_2O_4$ are Ni^{2+} and Ni^{3+}, which is consistent with the previous report[77].

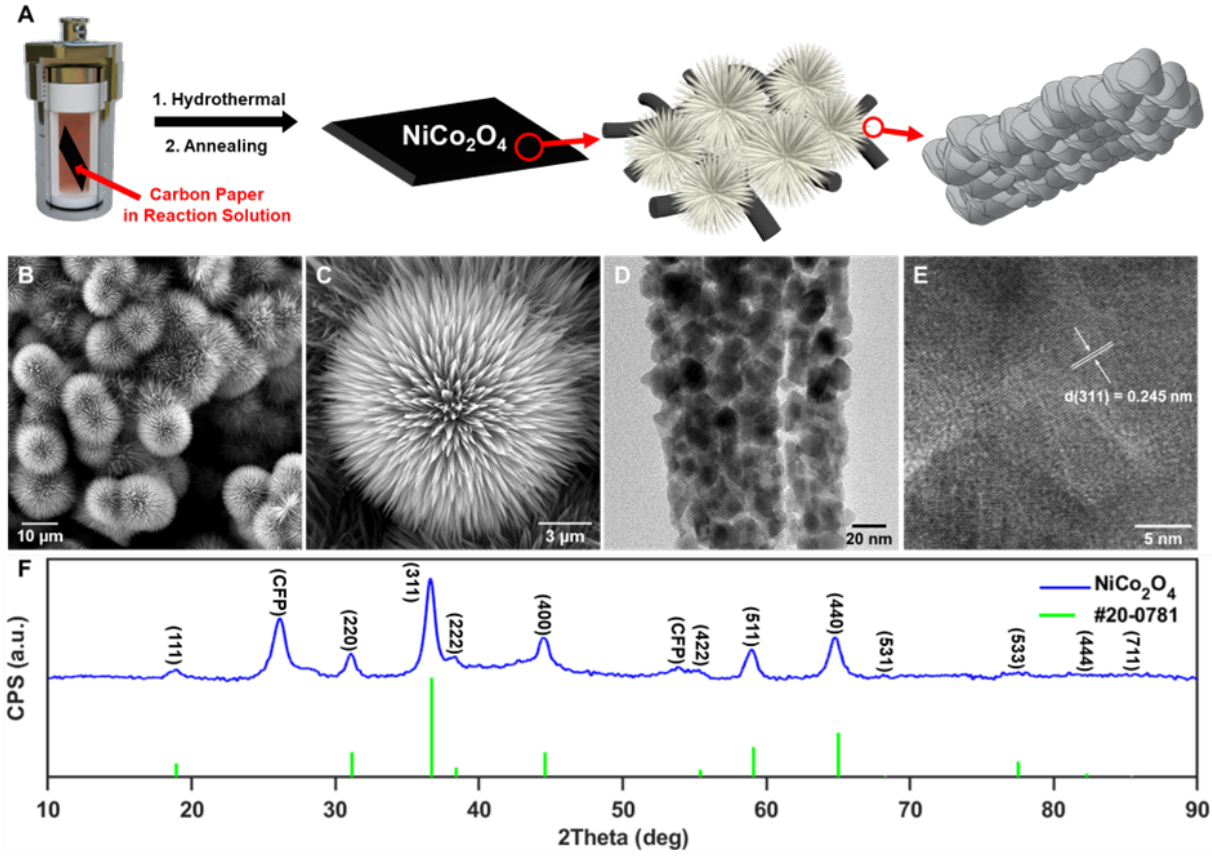

Figure 4.1: Structure characterization for $NiCo_2O_4$. **(A)** Schematic illustration of the synthetic method and corresponding hierarchical structures. **(B)** and **(C)** SEM images. **(D)** TEM image. **(E)** HRTEM image. **(F)** XRD Pattern. Green droplines indicate the standard XRD pattern for $NiCo_2O_4$ (JCPDS #20-0781).

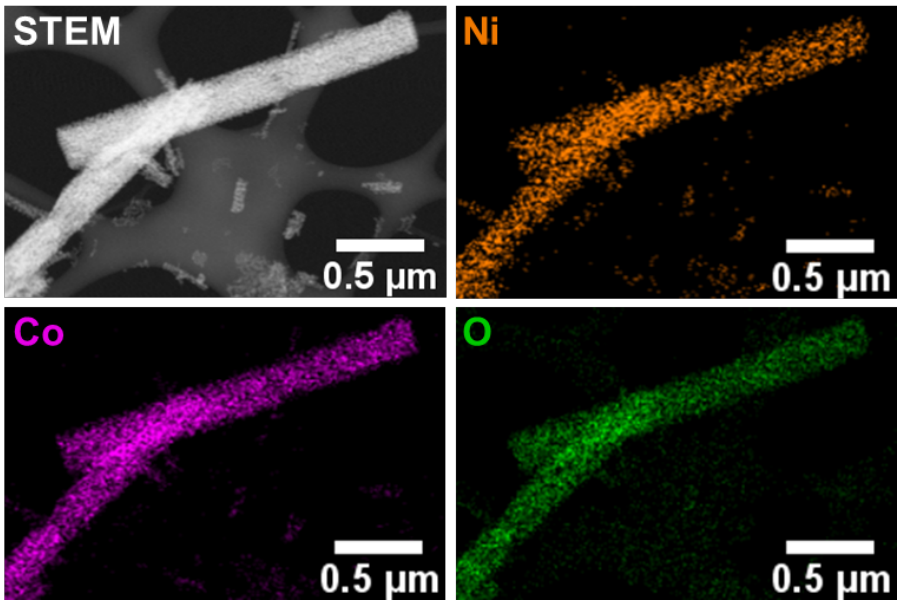

Figure 4.2: TEM-EDS mapping of $NiCo_2O_4$.

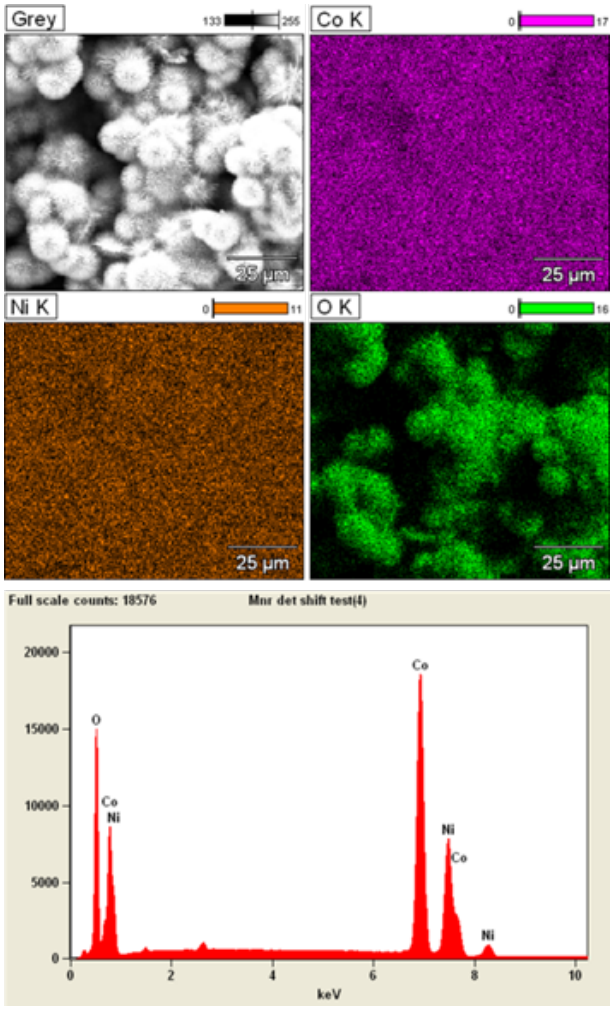

Figure 4.3: SEM-EDS mapping and spectrum $NiCo_2O_4$.

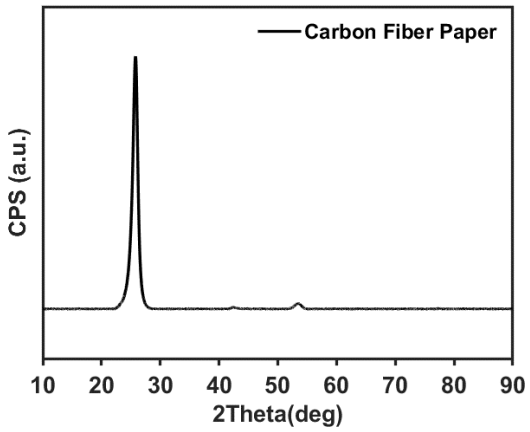

Figure 4.4: XRD pattern of the carbon fiber paper.

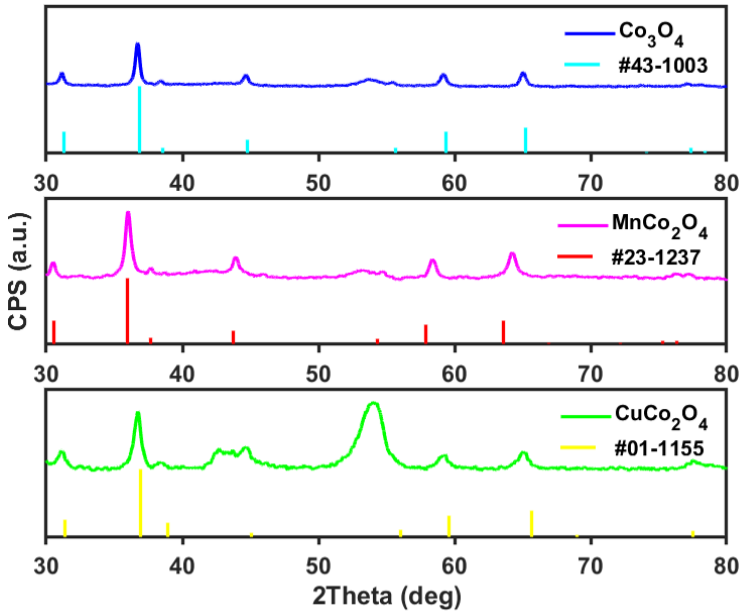

Figure 4.5: XRD patterns of Co_3O_4, $MnCo_2O_4$, and $CuCo_2O_4$.

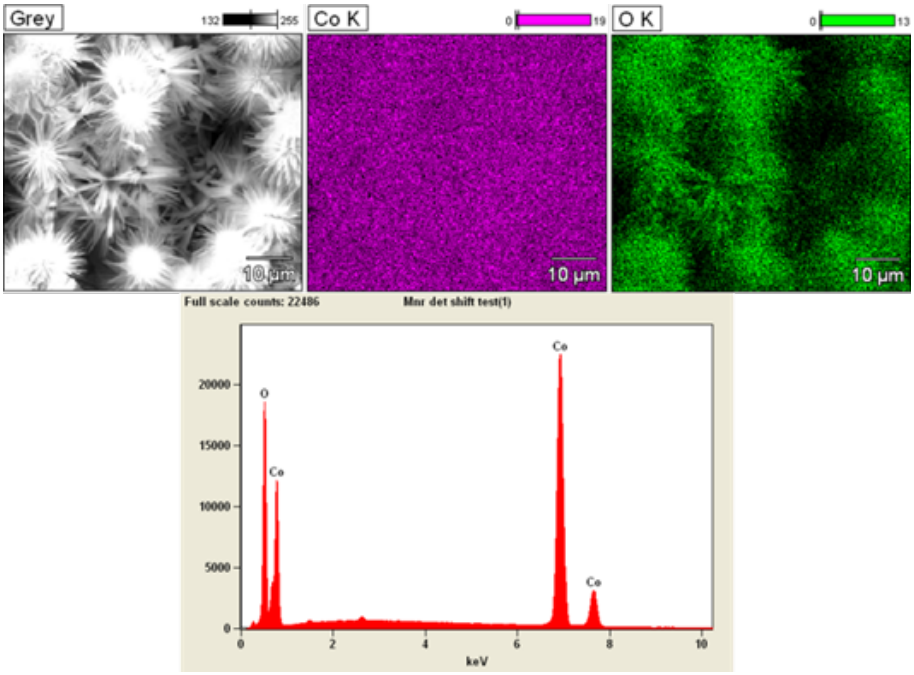

Figure 4.6: SEM-EDS mapping and spectrum Co_3O_4.

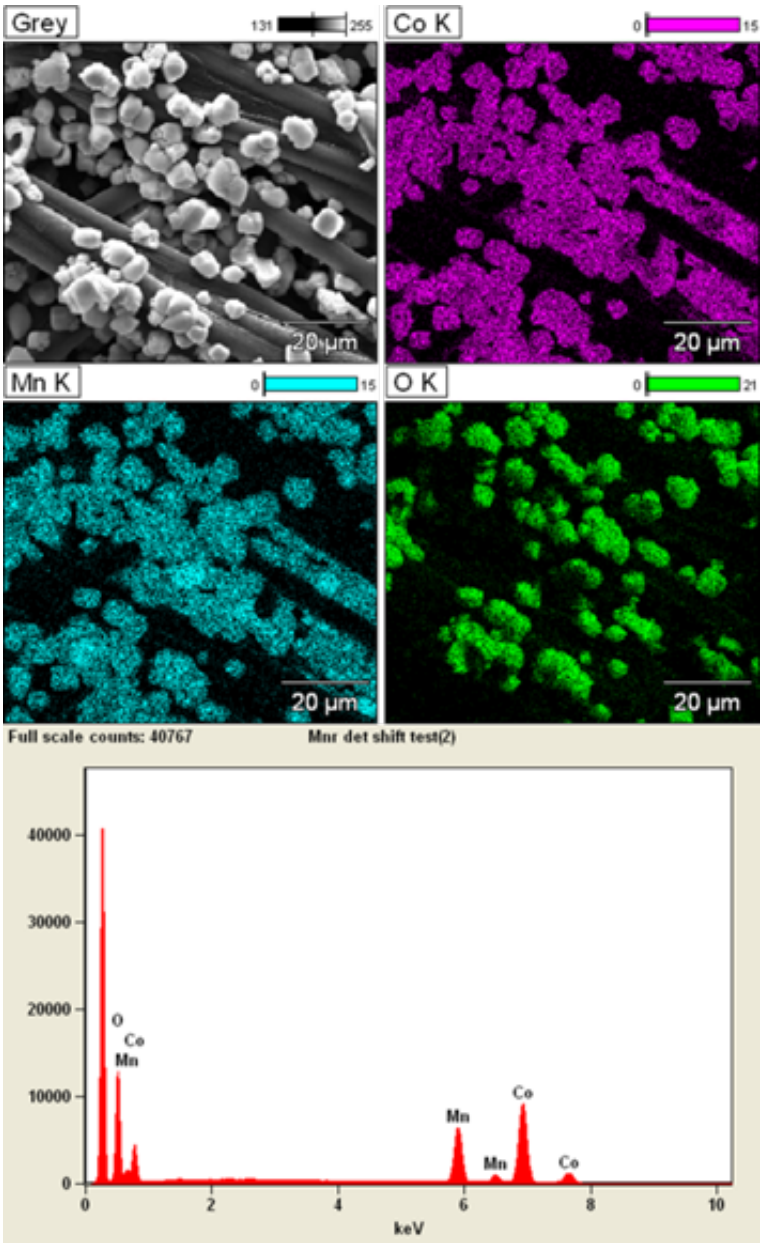

Figure 4.7: SEM-EDS mapping and spectrum $MnCo_2O_4$.

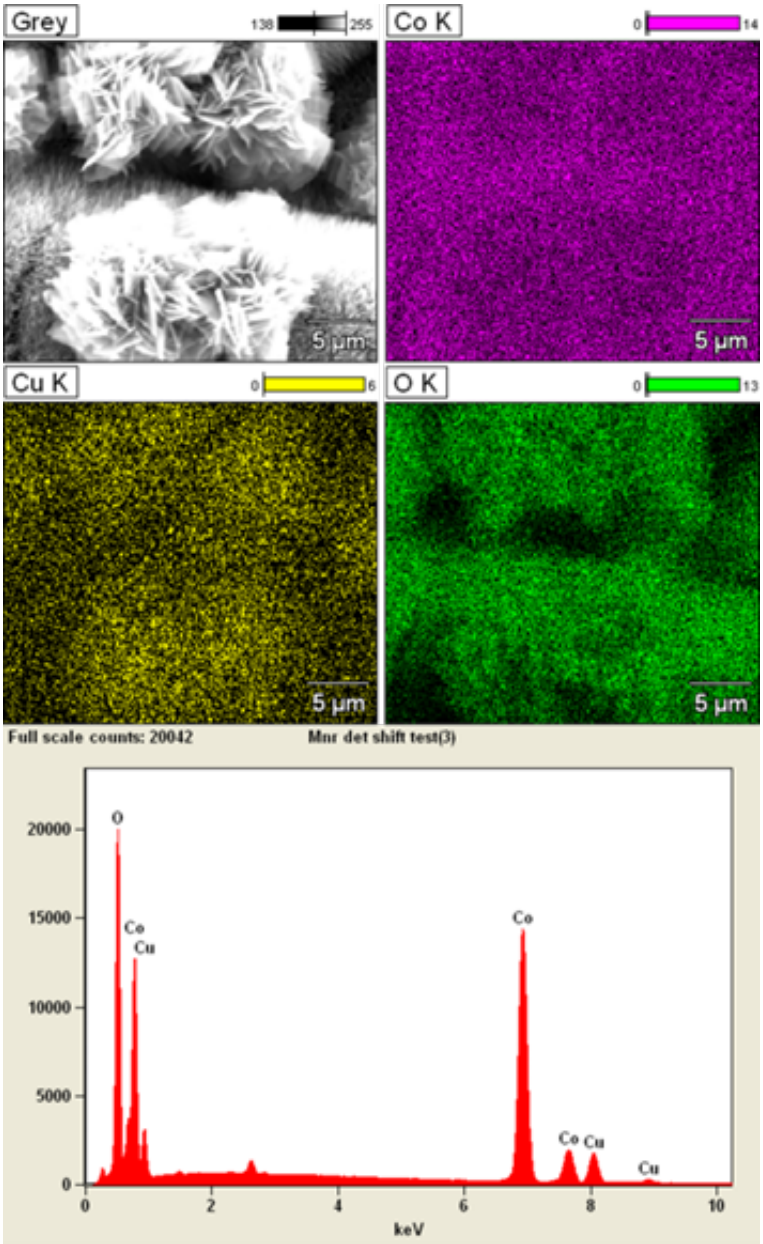

Figure 4.8: SEM-EDS mapping and spectrum $CuCo_2O_4$.

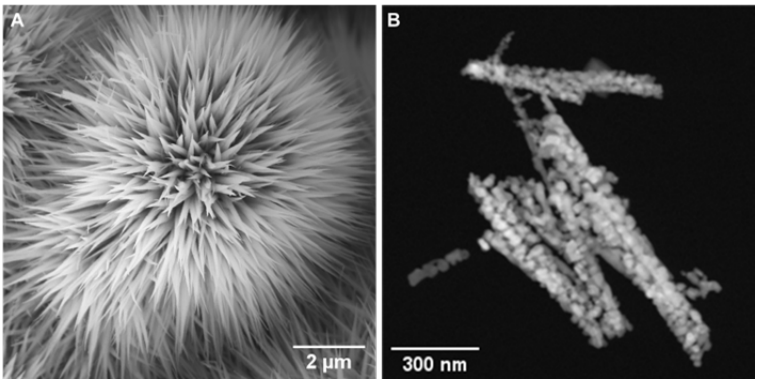

Figure 4.9: **(A)** SEM image **(B)** STEM image of Co_3O_4.

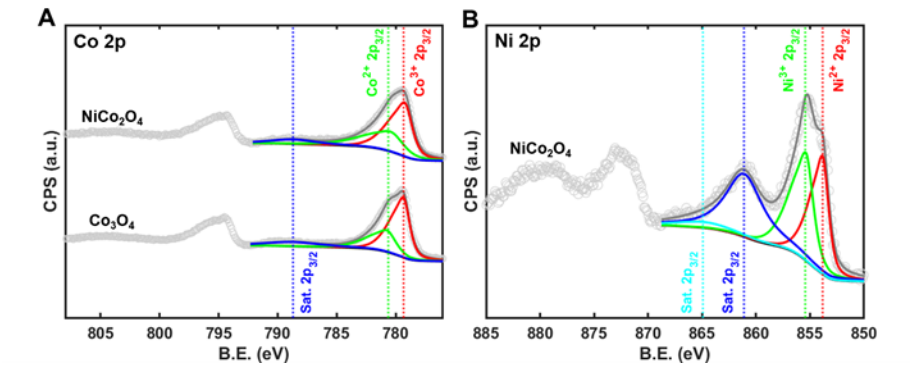

Figure 4.10: XPS spectrum of (**A**) Co 2p region of $NiCo_2O_4$ and Co_3O_4. (**B**) Ni 2p region of $NiCo_2O_4$.

The x-ray absorption near edge spectroscopy (XANES) and extended x-ray absorption fine structure (EXAFS) analysis were employed to determine the atomic environment of Ni and Co in $NiCo_2O_4$ and Co_3O_4. The spinel structure (AB_2O_4) consists of tetrahedral sites (A site or Td site) and octahedral sites (B site or Oh site) in a ratio of 1:2 (**Figure 4.11A**).[78] The Co K-edge Fourier Transformed EXAFS (FT-EXAFS) revealed the local bonding structure of Co in $NiCo_2O_4$ and Co_3O_4. As depicted in **Figure 4.11B**, three major peaks at $\sim$ 1.5 Å, 2.4 Å, and 3.0 Å are associated with the Co-O, Co_{Oh}-Co/Ni_{Oh}, and Co_{Td}-Co/Ni_{Oh} scattering paths, respectively.[61,79,80] For $NiCo_2O_4$ and Co_3O_4, both Co_{Oh} and Co_{Td} have substantial populations based on the comparably high Co_{Oh}-Co/Ni_{Oh} and Co_{Td}-Co/Ni_{Oh} peak intensity. For $NiCo_2O_4$, however, the Co_{Oh}-Co/Ni_{Oh} peak intensity decreases and the Co_{Td}-Co/Ni_{Oh} peak intensity increases, indicating that Ni tends to replace Co in the octahedral site. In addition, as shown in the Co K-edge XANES(**Figure 4.12A**), the pre-peak feature $\sim$ 7709 eV indicates the superposition of the 1s to 3d transition of tetrahedral Co and the 1s to $4t_{1u}$ transition of the octahedral low spin Co(III),[81] which supports the conclusion that tetrahedral and octahedral Co exist in both structures.

According to the Ni K-edge FT-EXAFS (**Figure 4.11C**), three major peaks at $\sim$ 1.6 Å, 2.5 Å, and 3.1 Å are associated with the Ni-O, Ni_{Oh}-Co/Ni_{Oh}, and Ni_{Td}-Co/Ni_{Oh} scattering paths, respectively.[82] The significantly higher intensity of the Ni_{Oh}-Co/Ni_{Oh} peak compared to that of the Ni_{Td}-Co/Ni_{Oh} peak demonstrates that Ni in octahedral coordination predominates over Ni in tetrahedral coordination. According to the Ni K-edge XANES (**Figure 4.12B**), the minor pre-peak feature at $\sim$ 8334 eV suggests that the local Ni structure is not totally symmetric,[83] confirming the existence of Ni in the tetrahedral site. In addition, based on the fitting result shown in **Table 4.2**, the Ni-O bond length is 1.985 Å, which is very close to but slightly longer than the typical Ni^{3+}-O bond distance (1.95-1.98 Å) in octahedral coordination,[84] indicating that the majority of Ni stays trivalent with a small divalent portion in the octahedral site. Theoretical model structures for $Co_{Td}[Co_{Oh}]_2O_4$, $Ni_{Td}[Co_{Oh}]_2O_4$, and $Co_{Td}[Ni_{Oh}Co_{Oh}]O_4$ were constructed and examined to determine the quantitative atomic

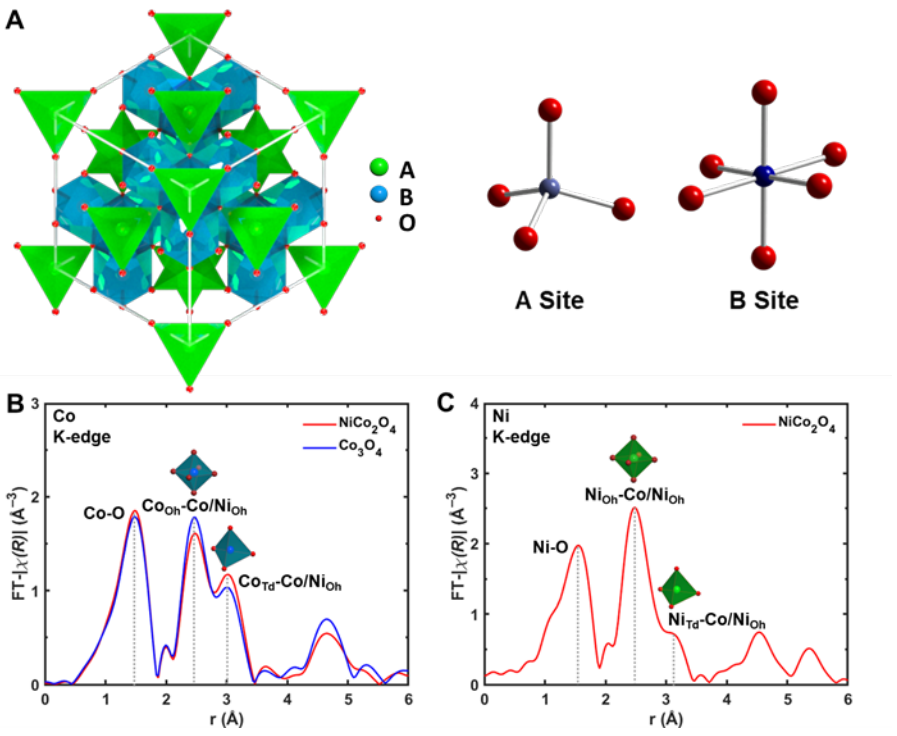

Figure 4.11: **(A)** Schematic illustration of the spinel crystal structure showing the tetrahedral (Td) and octahedral (Oh) sites. **(B)** FT-EXAFS spectrum of Co K-edge from $NiCo_2O_4$ and Co_3O_4 showing the peaks assigned to Td and Oh. **(C)** FT-EXAFS spectrum of Ni K-edge from $NiCo_2O_4$ showing the peaks assigned to Td and Oh.

environment of Co and Ni. The theoretical structure details for the standard model were calculated (See following section for detailed calculations). From the FT-EXAFS fitting results of the Co and Ni K-edges from the as-prepared $NiCo_2O_4$, the results are considerably closer to those of the $Co_{Td}[Ni_{Oh}Co_{Oh}]O_4$ model structure, indicating that Ni mainly occupies the octahedral site while Co occupies both the octahedral and tetrahedral sites.

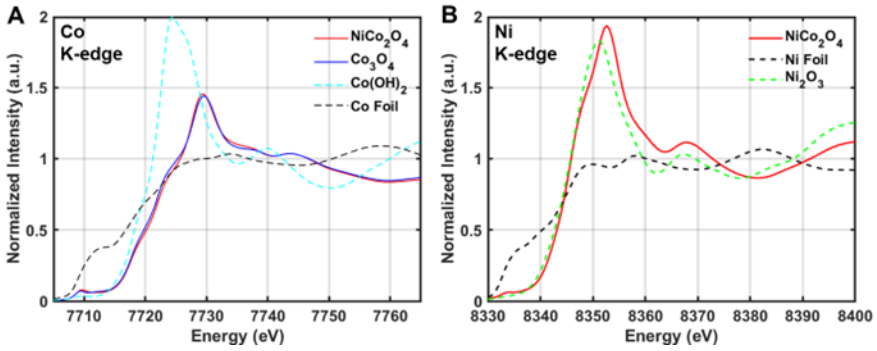

Figure 4.12: XANES spectrum of **(A)** Co K-edge from $NiCo_2O_4$ and Co_3O_4. **(B)** Ni K-edge from $NiCo_2O_4$. $Co(OH)_2$, Co Foil, and Ni_2O_3 are standard spectra.

4.3.1 Building EXAFS Fitting Models for Co_3O_4 and $NiCo_2O_4$

In a typical spinel structure AB_2O_4, there are two kinds of sites created by oxygen, which are the tetrahedral site (A Site) and the octahedral site (B site) (**Figure 4.11A**). To figure out which site nickel atom stays (tetrahedral or octahedral), it is essential to study the standard structure model of Co_3O_4 and $NiCo_2O_4$, and investigate what should be the fitting result from FT-EXAFS. Co_3O_4 and $NiCo_2O_4$ are already confirmed to possess the Fd-3m spinel structure, therefore we will begin with the fundamental spinel structure.

4.3.1.1 Co_3O_4 Model Structure

A = Co and B = Co, Model: $Co_{Td}[Co_{Oh}]_2O_4$

(Td: Tetrahedral Site; Oh: Octahedral Site; N = Coordination Number; CN = Average Coordination Number; A-B = A as center atom, B as coordinating atom; R = atomic distance. The unit cell is set as 8 Å. We only consider the metal-metal distance of around 3 Å, so A-A bond (over 5 Å) is not considered. Hereinafter the same.)

$$\textbf{For A Site}: N_{A-B} = 12; R_{A-B} = 3.32\ \text{Å}; N_{A-O} = 4; R_{A-O} = 2\ \text{Å}$$

$$\textbf{For B Site}: N_{B-A} = 6; R_{B-A} = 3.32\ \text{Å}; R_{B-B} = 2.83\ \text{Å}; N_{B-O} = 6; R_{B-O} = 1.73\ \text{Å}$$

Because A atom and B atom are the same (Co), so A-B and B-A are the same, so:

$$CN_{A-B} = \frac{12 \times 1 + 6 \times 2}{1 + 2} = 8$$
$$CN_{B-A} = \frac{12 \times 1 + 6 \times 2}{1 + 2} = 8$$
$$CN_{B-B} = \frac{0 \times 1 + 6 \times 2}{1 + 2} = 4$$

Therefore: For Co A site, only 1 metal-metal bond distance of 3.32 Å with a coordination number of 8. For Co B site, there are 2 bond distances: A shorter bond distance of 2.83 Å with a coordination number of 4. A longer bond distance of 3.32 Å with a coordination

number of 8. For metal-oxygen bonds:

$$CN_{A-O} = CN_{A-O} = \frac{4 \times 1 + 6 \times 2}{1 + 2} = 5.3$$
$$R_{A-O} = R_{B-O} = \frac{2 \times 4 + 1.73 \times 6 \times 2}{1 + 2} = 1.8 \text{ Å}$$

And based on the XAS principle, Co and Ni cannot be distinguished by XAS as scattering neighbors. So, the Co_3O_4 theoretical model structure features seen by EXAFS should be:

Co K-edge	$\mathbf{R_{Co\text{-}O}}$ **(Å)**	$\mathbf{CN_{Co\text{-}O}}$	$\mathbf{R_{Co\text{-}Co/Ni}}$ **(Å)**	$\mathbf{CN_{Co\text{-}Co/Ni}}$	$\mathbf{R_{Co\text{-}Co/Ni}}$ **(Å)**	$\mathbf{CN_{Co\text{-}Co/Ni}}$
$\mathbf{Co_{Td}[Co_{Oh}]_2O_4}$	1.8	5.3	2.83	4	3.32	8

4.3.1.2 $NiCo_2O_4$ Model Structure

For $NiCo_2O_4$ structure, there are two possibilities which are A = Ni, B = Co (Ni in tetrahedral site, Co in octahedral site, denote as $Ni_{Td}[Co_{Oh}]_2O_4$) and A = Co, B = Co and Ni (Half Co in tetrahedral site, half Co in octahedral site, Ni in octahedral site, denote as $Co_{Td}[Co_{Oh}Ni_{Oh}]O_4$). We will discuss both cases.

I. A = Ni and B = Co, Model: $\mathbf{Ni_{Td}[Co_{Oh}]_2O_4}$

For A Site : $N_{A-B} = 12; R_{A-B} = 3.32$ Å; $N_{A-O} = 4; R_{A-O} = 2$ Å

For B Site : $N_{B-A} = 6; R_{B-A} = 3.32$ Å; $R_{B-B} = 2.83$ Å; $N_{B-O} = 6; R_{B-O} = 1.73$ Å

Because A atom and B atom is not the same, so A-B and B-A are not the same, so:

$$CN_{A-B} = 12$$
$$CN_{B-A} = 6$$
$$CN_{B-B} = \frac{6 \times 2}{2} = 6$$

Therefore:

For the Ni site, only 1 metal-metal bond distance of 3.32 Å with a coordination number of 12.

For Co site, there are 2 bond distances:

A shorter bond distance of 2.83 Å with a coordination number of 6.

A longer bond distance of 3.32 Å with a coordination number of 6.

For metal-oxygen bonds:

$$CN_{A-O} = 4;\ R_{A-O} = 2\ \text{Å}$$

$$CN_{B-O} = 6;\ R_{B-O} = 1.73\ \text{Å}$$

So, the $Ni_{Td}[Co_{Oh}]_2O_4$ theoretical model structure features seen by EXAFS should be:

Co K-Edge	$\mathbf{R_{Co\text{-}O}}$ **(Å)**	$\mathbf{CN_{Co\text{-}O}}$	$\mathbf{R_{Co\text{-}Co/Ni}}$ **(Å)**	$\mathbf{CN_{Co\text{-}Co/Ni}}$	$\mathbf{R_{Co\text{-}Co/Ni}}$ **(Å)**	$\mathbf{CN_{Co\text{-}Co/Ni}}$
$\mathbf{Ni_{Td}[Co_{Oh}]_2O_4}$	1.73	6	2.83	6	3.32	6
Ni K-edge	$\mathbf{R_{Ni\text{-}O}}$ **(Å)**	$\mathbf{CN_{Ni\text{-}O}}$	$\mathbf{R_{Ni\text{-}Co/Ni}}$ **(Å)**	$\mathbf{CN_{Ni\text{-}Co/Ni}}$	$\mathbf{R_{Ni\text{-}Co/Ni}}$ **(Å)**	$\mathbf{CN_{Ni\text{-}Co/Ni}}$
$\mathbf{Ni_{Td}[Co_{Oh}]_2O_4}$	2	4	-	0	3.32	12

II. A = Co and B = Co and Ni, Model: $\mathbf{Co_{Td}[Co_{Oh}Ni_{Oh}]O_4}$

For A Site : $N_{A-B} = 12; R_{A-B} = 3.32\ \text{Å}; N_{A-O} = 4; R_{A-O} = 2\ \text{Å}$

For B Site : $N_{B-A} = 6; R_{B-A} = 3.32\ \text{Å}; R_{B-B} = 2.83\ \text{Å}; N_{B-O} = 6; R_{B-O} = 1.73\ \text{Å}$

Because A atom and B atom is not the same, so A-B and B-A are not the same, so:

$$CN_{A-B} = \frac{12+6}{1+1} = 9$$

$$CN_{B-A} = 6$$

$$CN_{B-B} = \frac{6\times 2}{2} = 6$$

Therefore:

For Co site, there are 2 bond distances:

A shorter bond distance of 2.83 Å with a coordination number of 6.

A longer bond distance of 3.32 Å with a coordination number of 9.

For the Ni site, there are 2 bond distances:

A shorter bond distance of 2.83 Å with a coordination number of 6.

A longer bond distance of 3.32 Å with a coordination number of 6.

For metal-oxygen bonds:

$$CN_{Co-O} = \frac{4+6}{1+1} = 5;\ R_{Co-O} = \frac{2\times 4 + 1.73\times 6}{1+1} = 2\text{Å}$$
$$CN_{Ni-O} = 6; \qquad R_{Ni-O} = 1.73\text{Å}$$

So, the $Co_{Td}[Co_{Oh}Ni_{Oh}]O_4$ theoretical model structure features seen by EXAFS should be:

Co K-Edge	$\mathbf{R_{Co\text{-}O}}$ **(Å)**	$\mathbf{CN_{Co\text{-}O}}$	$\mathbf{R_{Co\text{-}Co/Ni}}$ **(Å)**	$\mathbf{CN_{Co\text{-}Co/Ni}}$	$\mathbf{R_{Co\text{-}Co/Ni}}$ **(Å)**	$\mathbf{CN_{Co\text{-}Co/Ni}}$
$\mathbf{Ni_{Td}[Co_{Oh}]_2O_4}$	1.84	5	2.83	6	3.32	9
Ni K-edge	$\mathbf{R_{Ni\text{-}O}}$ **(Å)**	$\mathbf{CN_{Ni\text{-}O}}$	$\mathbf{R_{Ni\text{-}Co/Ni}}$ **(Å)**	$\mathbf{CN_{Ni\text{-}Co/Ni}}$	$\mathbf{R_{Ni\text{-}Co/Ni}}$ **(Å)**	$\mathbf{CN_{Ni\text{-}Co/Ni}}$
$\mathbf{Ni_{Td}[Co_{Oh}]_2O_4}$	1.73	6	2.83	6	3.32	6

4.3.1.3 Conclusion

As the models have been studied, the results were gathered in Table4.1, which will be the evidence for investigating the Ni coordination environment in the actual $NiCo_2O_4$ sample.

Table 4.1: The theoretical model structure features are seen by EXAFS.

Co K-Edge	$\mathbf{R_{Co\text{-}O}}$ (Å)	$\mathbf{CN_{Co\text{-}O}}$	$\mathbf{R_{Co\text{-}Co/Ni}}$ (Å)	$\mathbf{CN_{Co\text{-}Co/Ni}}$	$\mathbf{R_{Co\text{-}Co/Ni}}$ (Å)	$\mathbf{CN_{Co\text{-}Co/Ni}}$
$\mathbf{Co_{Td}[Co_{Oh}]_2O_4}$	1.8	5.3	2.83	4	3.32	8
$\mathbf{Ni_{Td}[Co_{Oh}]_2O_4}$	1.73	6	2.83	6	3.32	6
$\mathbf{Co_{Td}[Co_{Oh}Ni_{Oh}]O_4}$	1.84	5	2.83	6	3.32	9
Ni K-edge	$\mathbf{R_{Ni\text{-}O}}$ (Å)	$\mathbf{CN_{Ni\text{-}O}}$	$\mathbf{R_{Ni\text{-}Co/Ni}}$ (Å)	$\mathbf{CN_{Ni\text{-}Co/Ni}}$	$\mathbf{R_{Ni\text{-}Co/Ni}}$ (Å)	$\mathbf{CN_{Ni\text{-}Co/Ni}}$
$\mathbf{Co_{Td}[Co_{Oh}]_2O_4}$	-	-	-	-	-	-
$\mathbf{Ni_{Td}[Co_{Oh}]_2O_4}$	2	4	-	0	3.32	12
$\mathbf{Co_{Td}[Co_{Oh}Ni_{Oh}]O_4}$	1.73	6	2.83	6	3.32	6

Table 4.2: Ni and Co K-edge FT-EXAFS in Co_3O_4 and $NiCo_2O_4$ Fitting Results

Co K-Edge	$\mathbf{R_{Co\text{-}O}}$ (Å)	$\mathbf{CN_{Co\text{-}O}}$	$\mathbf{R_{Co\text{-}Co/Ni}}$ (Å)	$\mathbf{CN_{Co\text{-}Co/Ni}}$	$\mathbf{R_{Co\text{-}Co/Ni}}$ (Å)	$\mathbf{CN_{Co\text{-}Co/Ni}}$
$\mathbf{Co_3O_4}$	1.922±0.006	5.0±0.7	2.868±0.006	5.3±0.7	3.374±0.008	6±1
$\mathbf{NiCo_2O_4}$	1.921±0.008	5.5±0.9	2.878±0.008	5.4±0.9	3.395±0.008	8±1
Ni K-edge	$\mathbf{R_{Ni\text{-}O}}$ (Å)	$\mathbf{CN_{Ni\text{-}O}}$	$\mathbf{R_{Ni\text{-}Co/Ni}}$ (Å)	$\mathbf{CN_{Ni\text{-}Co/Ni}}$	$\mathbf{R_{Ni\text{-}Co/Ni}}$ (Å)	$\mathbf{CN_{Ni\text{-}Co/Ni}}$
$\mathbf{NiCo_2O_4}$	1.985±0.007	5.7±0.9	2.890±0.005	9±1	3.38±0.01	5±1

4.3.2 Electrochemical Performance Evaluation

The OER performance of the catalysts was measured using a single-cell three-electrode setup in 0.5 M H_2SO_4. The working electrode was a catalyst-loaded carbon fiber paper clipped to an electrode clip, while the reference electrode was an Ag/AgCl electrode, and the counter electrode was a Pt wire. Unless otherwise specified, all potentials in this work are versus the reversible hydrogen electrode (RHE), and all electrochemical data are iR-corrected. The OER activity of the examined catalyst is depicted in **Figure 4.13A**. $NiCo_2O_4$ demonstrated ultrahigh OER activity in 0.5 M H_2SO_4 of an overpotential of 407 mV at a current density of 100 mA/cm^2, which is much lower than that of Co_3O_4 (474 mV). A chronopotentiometry test kept at 10 mA/cm^2 was performed to assess the stability of the catalysts (**Figure 4.13B**). After the 20-hour test, the overpotential for $NiCo_2O_4$ increased by only 68.9 mV, demonstrating more robust stability compared to Co_3O_4 (81.7 mV increase). **Figure 4.13C** compares the current density at 1.65 V for OER in 0.5 M H_2SO_4 for the catalysts studied in this work to that of various state-of-the-art catalysts.[56,85,86] The as-prepared $NiCo_2O_4$ was vastly superior to other acidic OER catalysts. As displayed in **Figure 4.13D**, the Tafel slope of $NiCo_2O_4$ was 65.4 mV/dec, much lower than that of Co_3O_4 (84.1 mV/dec), showing superior OER kinetics on $NiCo_2O_4$. We also compared the acidic OER performance of $NiCo_2O_4$ to that of other spinel oxides ($MnCo_2O_4$ and $CuCo_2O_4$). The activity of $NiCo_2O_4$ was also superior to that of other spinel catalysts, which led to 448 mV for $MnCo_2O_4$ and 502 mV for $CuCo_2O_4$ (**Figure 4.14**).

The chronopotentiometry test in 0.5 M H_2SO_4 further characterized $NiCo_2O_4$ with a longer duration and a higher current density, respectively. $NiCo_2O_4$ was functional for over 70 hours at 10 mA/cm^2 with only a 106.9 mV overpotential increase (**Figure 4.15A**). In addition, after the chronopotentiometry test for 20 hours at 100 mA/cm^2, the overpotential for $NiCo_2O_4$ increased by only 98.6 mV (**Figure 4.15A**), indicating exceptional durability at high current density. This high activity, long-term durability, and high-current-density stability of $NiCo_2O_4$ demonstrates its great potential as an anode catalyst for the industrial

Table 4.3: Ni and Co K-edge *in situ* FT-EXAFS at 1.65 V in Co_3O_4 and $NiCo_2O_4$ Fitting Results

Co K-Edge	$\mathbf{R_{Co\text{-}O}}$ **(Å)**	$\mathbf{CN_{Co\text{-}O}}$	$\mathbf{R_{Co\text{-}Co/Ni}}$ **(Å)**	$\mathbf{CN_{Co\text{-}Co/Ni}}$	$\mathbf{R_{Co\text{-}Co/Ni}}$ **(Å)**	$\mathbf{CN_{Co\text{-}Co/Ni}}$
Co_3O_4-1.65V	1.89±0.01	2.7±0.6	2.86±0.01	1.8±0.4	3.33±0.01	3.6±0.8
$NiCo_2O_4$-1.65V	1.908±0.007	4.1±0.7	2.859±0.008	3.9±0.7	3.37±0.01	5±1
Ni K-edge	$\mathbf{R_{Ni\text{-}O}}$ **(Å)**	$\mathbf{CN_{Ni\text{-}O}}$	$\mathbf{R_{Ni\text{-}Co/Ni}}$ **(Å)**	$\mathbf{CN_{Ni\text{-}Co/Ni}}$	$\mathbf{R_{Ni\text{-}Co/Ni}}$ **(Å)**	$\mathbf{CN_{Ni\text{-}Co/Ni}}$
$NiCo_2O_4$-1.65V	1.944±0.007	4.6±0.9	2.865±0.005	9±1	3.40±0.01	7±2

water-splitting system.

To comprehend the exceptional structural stability that Ni imparts, we used *in situ* XAS analysis to investigate the atomic configuration of $NiCo_2O_4$ and Co_3O_4 under OER conditions, using 1.65 V as the OER working potential for *in situ* XAS data collection. The coordination number change compared to the pristine structure was significantly smaller for $NiCo_2O_4$ for the Co-O bond and Co_{Oh}-Co/Ni_{Oh} bond at the potential of 1.65 V (**Figure 4.16A, 4.16C**, and **Table 4.2**, **4.3**). This less coordination number change may indicate that $NiCo_2O_4$ was more durable than Co_3O_4 during the OER process, which is consistent with the result that $NiCo_2O_4$ had a minor potential increase in the chronopotentiometry test (**Figure 4.13B**). According to **Figure 4.16B, 4.16D**, and **Table 4.2**, **4.3**, Ni was substantially more stable than Co under the OER condition, as evidenced by less coordination number change for the Ni-O bond and Ni_{Oh}-Co/Ni_{Oh} bond, which may support $NiCo_2O_4$'s exceptional durability.

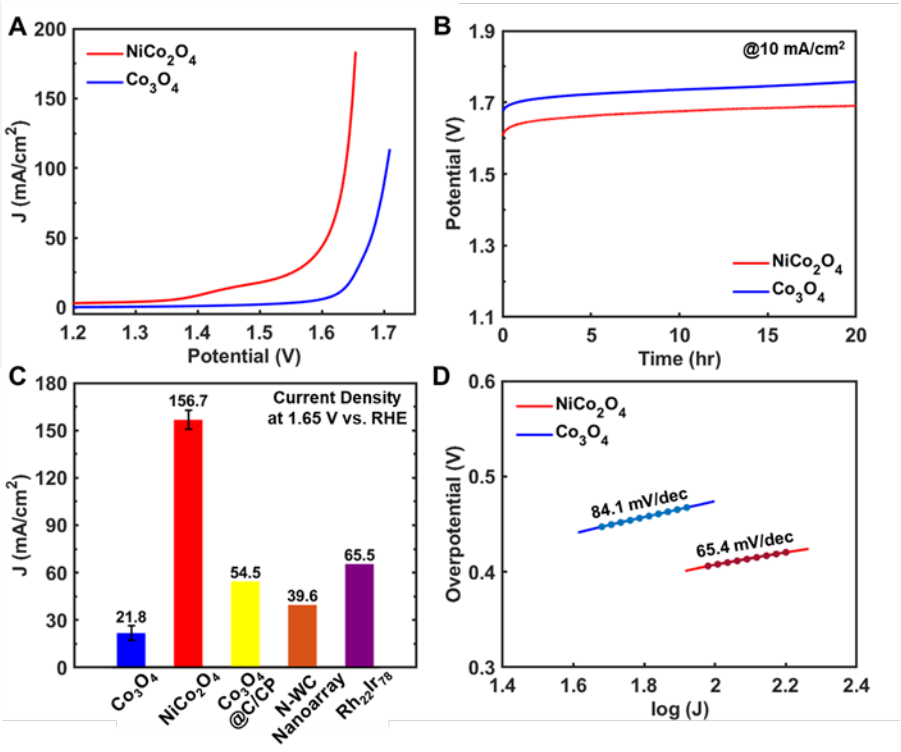

Figure 4.13: OER performance evaluation in 0.5 M H_2SO_4 for $NiCo_2O_4$ and Co_3O_4. **(A)** Polarization curve. **(B)** Chronopotentiometry test at 10 mA/cm^2. **(C)** Current density comparison histogram with other reported works at 1.65 V vs. RHE. (D) Tafel plots.

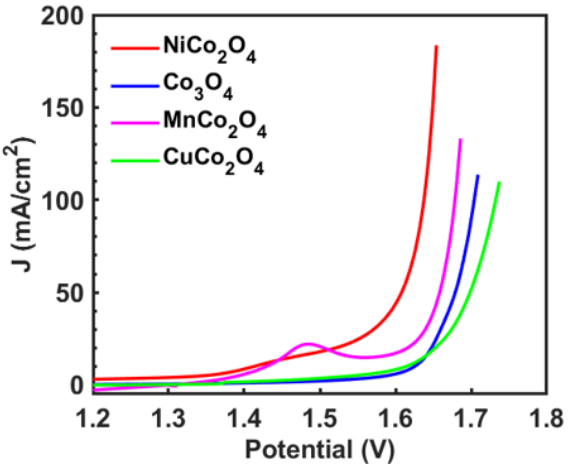

Figure 4.14: OER polarization curve in 0.5 M H_2SO_4 for $NiCo_2O_4$, Co_3O_4, $MnCo_2O_4$, and $CuCo_2O_4$.

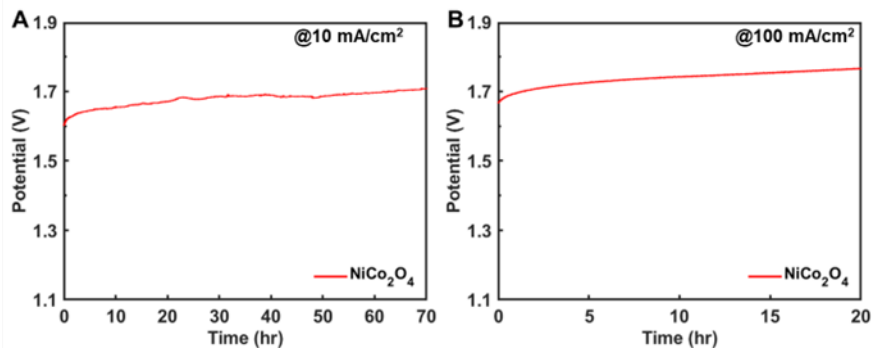

Figure 4.15: Chronopotentiometry test in 0.5 M H_2SO_4 for $NiCo_2O_4$: **(A)** at 10 mA/cm^2 for 70 hours. **(B)** at 100 mA/cm^2 for 20 hours.

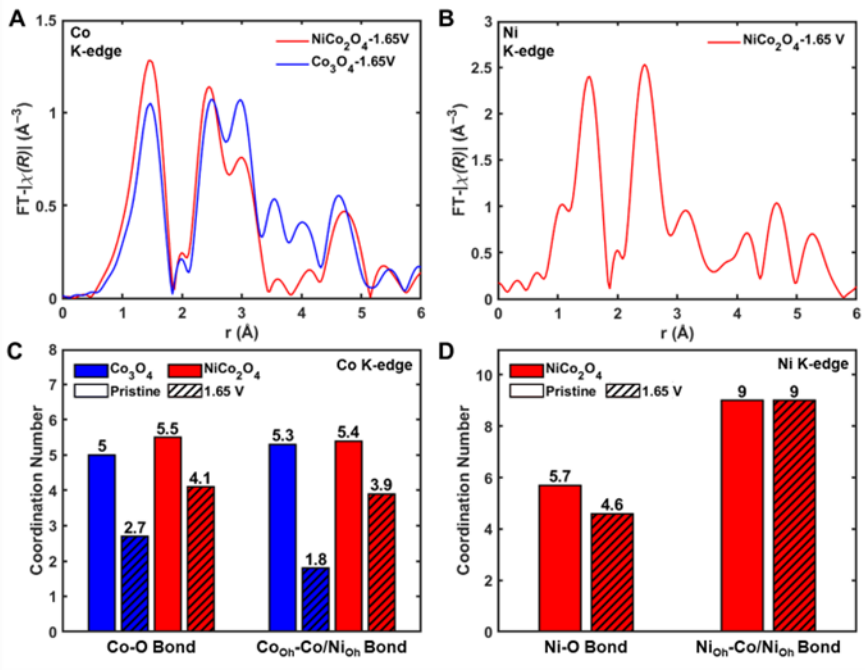

Figure 4.16: *In situ* EXAFS analysis of $NiCo_2O_4$ and Co_3O_4. **(A)** FT-EXAFS results for the Co K-edge from $NiCo_2O_4$ and Co_3O_4. **(B)** FT-EXAFS results for the Ni K-edge from $NiCo_2O_4$. **(C)** Coordination number change for the Co-O and Co_{Oh}-Co/Ni_{Oh} bonds from the pristine structure to the structure at 1.65 V. **(D)** Coordination number change the Ni-O and Ni_{Oh}-Co/Ni_{Oh} bonds from the pristine structure to the structure at 1.65 V.

4.4 Simulation

Studies employing facet engineering of spinel Co_3O_4 to find the correlation between the Co^{III}/Co^{II} ratio and OER kinetics suggested that the Co^{III} in the octahedral site (Oh) is responsible for the high OER performance.[87,88,89] Our EXAFS analysis (**Figure 4.16A, 4.16C**, and **Table 4.2**, **4.3**) also clearly indicates that Co_{Oh} dissolution dominates in OER working conditions for Co_3O_4 catalysts, implying the abundant population of surface Co_{Oh}. While the Ni incorporation impedes the Co_{Oh} dissolution during OER, the lack of change in the Ni coordination environment during the OER (**Figure 4.16B, 4.16D**, and **Table 4.2**, **4.3**) rules out the Ni as the OER active site.

Accordingly, we constructed the (110) surface with a termination that exclusively exposes octahedral sites with Co occupation while the fully coordinated metals in Td sites remain below the top surface layer by $\sim$ 1 Å. The time-resolved Fourier-transform infrared spectroscopy study suggested that two adjacent active Co sites on the Co_3O_4 nanoparticles are simultaneously involved in a fast catalytic cycle.[90] Therefore, we considered the dual active sites for the OER pathway rather than only a single active site mechanism.[89,91,92] This allows consideration of the associative interaction between reaction intermediates on two adjacent Co_{Oh} sites. Based on the identical morphology between Co_3O_4 and $NiCo_2O_4$ (**Figure 4.1B**, **4.2**, and **4.9**), we assumed that their surface structures have a similar orientation, which is confirmed by the XRD (**Figure 4.1F** and **4.5**). We also investigated the possible effect of Ni_{Td} on OER activity.

Starting with the fully reduced state (Co^{II}-H_2O*) on the inverse spinel (110) surface, sequential deprotonation occurs as the electrode is polarized positively, oxidizing the catalyst surface. **Figure 4.17A** and **4.17B** show the free energies of various Co_3O_4 and $NiCo_2O_4$ (110) surface states, respectively. At low potential, the (110) surface is mainly covered by 0.5 monolayers Co^{II}-H_2O* and 0.5 monolayers Co^{III}-OH* state (denoted as μ_1-H_2O/μ_1-OH). In contrast, the fully oxidized surface (Co^{IV}=O* or 2μ_1-O) dominates at high potential. On

the $NiCo_2O_4$ (110) surface, the terminal oxo (Co^{IV}=O*) appears at U > 1.56 V while it requires U > 1.65 V on the Co_3O_4 (110) surface, which is 0.09 V higher. This agrees well with the experimental overpotential difference of 0.067 V (**Figure 4.13A**), implying that the fully oxidized surface (Co^{IV}) is the active phase for OER.[79,93,94]

From the fully oxidized (Co^{IV}) surface state, we calculated the free energy along the full OER pathway, as shown in **Figure 4.18A**. All elementary reaction steps are considered, including the proton-coupled electron transfer (PCET) step, non-electrochemical O-O bond formation, and the O_2 desorption steps. There are two possible pathways for O-O bond formation: direct O-O coupling (DOC) mechanism (**Figure 4.18A**, red) and adsorbate evolution mechanism (AEM), and the latter involves water nucleophilic attack (WNA) (**Figure 4.18A**, blue). In the DOC mechanism,[95,96] two adjacent terminal metal oxo combine to form the bridging O_2 species (μ_2-O_2). In the AEM mechanism,[90,97] interfacial water attacks the terminal oxo to form hydroperoxo (μ_1-OOH) species while transferring proton to a nearby terminal oxo (often via a Grotthuss chain of one or more additional waters), forming hydroxo (μ_1-OH). The black lines and frames in **Figure 4.18A** denote the common reaction steps for both mechanisms.

Figure 4.18B and **4.18C** show the free energy landscape along possible OER pathways in **Figure 4.18A** for Co_3O_4 and $NiCo_2O_4$ (110) surface, respectively. A theoretical overpotential (η) is defined using the extra potential above the equilibrium potential of the water oxidation (1.23 V) required to make all PCET steps exothermic.[98] On both surfaces, the value of η is determined by a water reduction step ($reaction_{8 \rightarrow 9}$ in **Figure 4.18B** and **4.18C**), which leads to the $2\mu_1$-OH state. This implies high stability for the mixed Co^{II}/Co^{III} state. For Co_3O_4 (110), we calculate $\eta = 0.61$ V. Whereas $NiCo_2O_4$ (110) has a $\eta = 0.45$ V, indicating higher OER performance of $NiCo_2O_4$ catalysts, which agrees with our experiments.

For the non-electrochemical steps on Co_3O_4 (110), the kinetic barrier of $\Delta G^{\ddagger} = 0.24$ eV for O-O coupling in the DOC mechanism is 0.49 eV lower than that in the AEM mechanism

($\Delta G^{\ddagger}$=0.73 eV). Moreover, the reaction free energy of ΔG = 0.5 eV is also lower. $NiCo_2O_4$ (110) leads to similar energetics of $\Delta G^{\ddagger}$=0.25 eV and ΔG=-0.46 eV for DOC mechanism and $\Delta G^{\ddagger}$=0.48 eV and ΔG=-0.21 eV for AEM.

Therefore, both catalysts prefer DOC mechanism to AEM. The μ_1-O_2/μ_1-OH state is the most energetically stable state among the O_2-bound states along the most favorable pathway (**Figure 4.18B** and **4.18C**). It leads to an O-O bond distance ($d_{O\text{-}O}$) of 1.27 Å with a spin density ($\rho\uparrow$) of 0.82 e^-, which agrees well with the strong superoxo signal (1068 cm^{-1}) from *in situ* experiments.[90,99] The μ_2-O_2 state also possesses partial radical character ($\rho\uparrow$=0.65 e^-) but with a longer O-O bond ($d_{O\text{-}O}$=1.34 Å). The endothermic transition from μ_2-O_2 to μ_1-O_2 (ΔG=0.17 eV) may explain the peroxo signal observed in electrochemical OER,[99] which also supports the DOC mechanism.

We found that the O_2 desorption step depends strongly on the presence of a nearby reaction intermediate. On both catalyst surfaces, the O_2 desorption is least endothermic from the μ_1-O_2/μ_1-OH state (Co^{III}/Co^{III}), with desorption free energy of 0.31 eV for Co_3O_4 (110) and 0.13 eV for $NiCo_2O_4$ (110). This supports the strong coupling of two Co active sites in the OER cycle.[90]

Our calculations indicate that all non-electrochemical steps are quite favorable on (110), which is supported by a theoretical study on Co_3O_4 (001) surface.[97] This implies that the electrochemical steps, depending strongly on the applied potential, play a crucial role. The state in which H_2O* is stabilized by a neighboring OH* via hydrogen bonding (μ_1-H_2O/μ_1-OH) is the primary phase that impedes the formation of active Co^{IV}=O species (**Figure 4.17A** and **4.17B**). The Co^{IV}=O formation determines the OER overpotential (**Figure 4.18B** and **4.18C**). The incorporation of Ni reduces the extra potential needed to oxidize the Co^{III}/Co^{II} surface state, leading to higher OER activity than Co_3O_4.

Moreover, our XAS measurements indicate that a small portion of Ni stays in the tetrahedral site (**Figure 4.11C**). To examine if surface Ni_{Td} affects the OER activity, we also constructed the $NiCo_2O_4$ (110) with Ni_{Oh}-Co_{Td} site exchange (**Figure 4.19**). We calculated

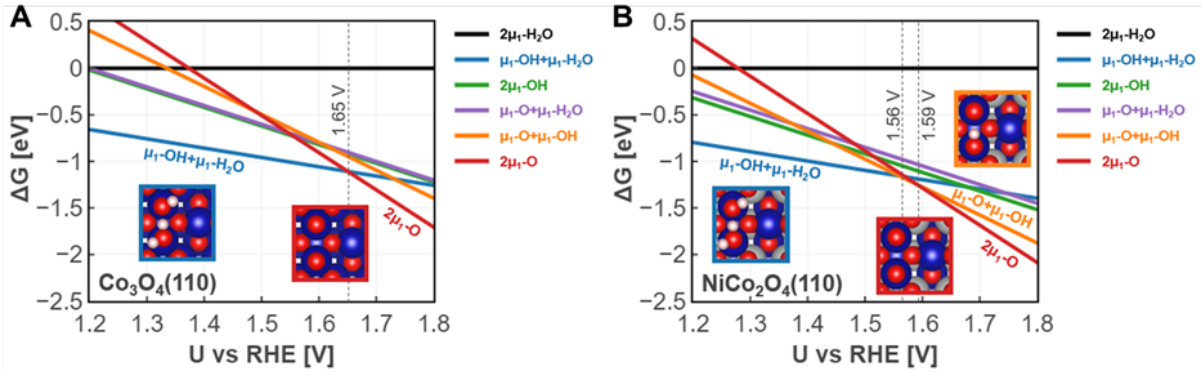

Figure 4.17: Surface Pourbaix diagrams for **(A)** Co_3O_4 (110) and **(B)** $NiCo_2O_4$ (110) surface. The insets show the atomic geometries of energetically favorable surface states. The blue, grey, red, and white spheres in the inset represent Co, Ni, O, and H elements.

the onset potential for the active phase (1.52 V) on this surface, which is similar to that of the intact $NiCo_2O_4$ (110) (1.56 V). However, this exchange leads to AEM ($\Delta G^{\ddagger}$=0.52 eV) rather than DOC mechanism because the μ_2-O_2 ($d_{O\text{-}O}$=1.35 Å) to μ_1-O_2 ($d_{O\text{-}O}$=1.28 Å) transition is unfavorable (ΔG=0.65 eV) due to the stable bridging O_2 state. This makes the non-electrochemical steps more sluggish, so this minor motif would not contribute to the higher OER activity of $NiCo_2O_4$ compared to Co_3O_4 (110).

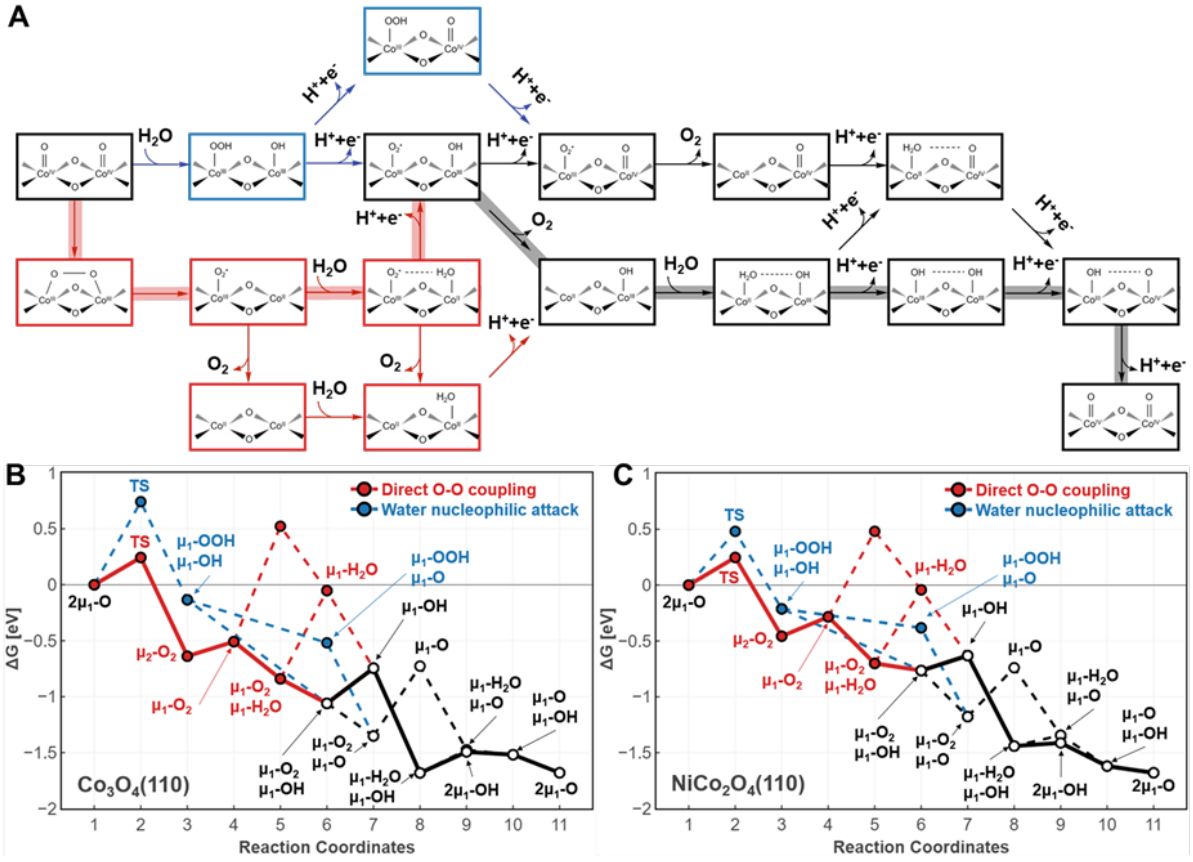

Figure 4.18: **(A)** OER network. Red lines represent the direct oxo coupling (DOC) mechanism, and blue lines represent the water nucleophilic attack adsorbate evolution mechanism (AEM) mechanism. The black line represents common elementary reaction steps for both mechanisms. The thick transparent line indicates the most favorable OER pathway. The free energy landscapes along OER pathways at 1.65 V vs. RHE on **(B)** Co_3O_4 (110) surface and **(C)** $NiCo_2O_4$ (110) surface. The thick solid line indicates the most favorable pathway, while the dashed line indicates another minor pathway. TS denotes the transition state for the O-O bond formation step.

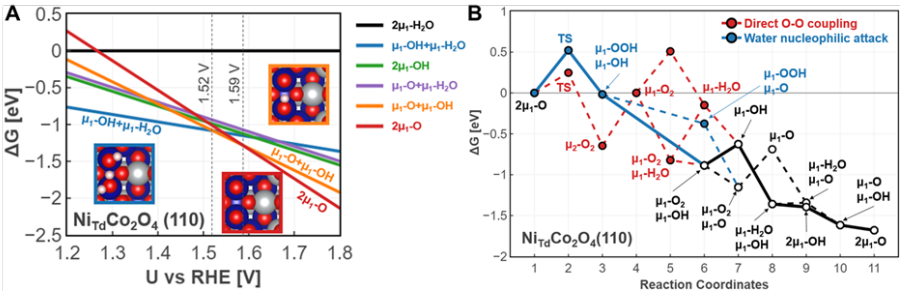

Figure 4.19: **(A)** Surface Pourbaix diagram for $Ni_{Td}Co_2O_4$ (110) surface. The insets show the atomic geometries of energetically favorable surface states. The blue, grey, red, and white spheres in the inset represent Co, Ni, O, and H elements. **(B)** Free energy landscape along OER pathways at 1.6 V vs. RHE. The thick solid line and dashed line indicate the most favorable pathway and other minor pathways, respectively. Red and blue lines represent the direct oxo coupling mechanism and water nucleophilic attack mechanism, respectively. The black line represents common elementary reaction steps for both mechanisms. TS denotes a transition state for the O-O bond formation step.

4.5 Conclusion

In summary, we utilized a facile hydrothermal-annealing method to synthesize the cobalt-based spinel oxides that obey the DOC designing rule. Specifically, the coordination environment of $NiCo_2O_4$ was studied via XAS, in which Ni mainly occupies the octahedral site. Among all the synthesized spinel oxides, $NiCo_2O_4$ demonstrated ultrahigh activity towards OER in 0.5 M H_2SO_4 with an overpotential of 407 mV at 100 mA/cm^2. The slight overpotential increase of 68.9 mV after the 20-hour chronopotentiometry test indicates $NiCo_2O_4$'s superior durability. *In situ* XAS studies revealed that adding Ni improved the structure endurance during the OER. DFT calculations unveiled that the favorable mechanism on the (110) surface of $NiCo_2O_4$ and Co_3O_4 is DOC mechanism. The $NiCo_2O_4$ (110) surface demonstrated 90 mV lower overpotential than the Co_3O_4 (110) surface. This work provides new insights for designing durable and effective non-precious catalysts for acidic OER. Moreover, the developed catalyst may provide the potential to serve as the anode material of the proton exchange membrane (PEM) electrolyzer, facilitating cheaper and more durable hydrogen production.

4.6 Author Contribution

Haotian Liu proposed the idea of Ni addition to improve the acidic OER performance, improved the synthetic recipe, and conducted the corresponding characterization. William A. Goddard and Soonho Kwon led the theoretical study. Qingying Jia and Ershuai Liu led the XAS measurement and analysis. Heting Pu provided support on synthesis and characterizartion. Zeyan Liu, Bosi Peng, Jin Cai, Ao Zhang, and Chengzhang Wan provided support for other characterizations. Yu Huang proposed and organized the project.

CHAPTER 5

Conclusion and Perspective

Throughout my Ph.D. studies, I focused primarily on fields related to water-splitting, such as hydrogen evolution reaction (HER) in alkaline media catalyzed by Pt-based alloy and oxygen evolution reaction (OER) in acidic media catalyzed by non-precious Co-based spinel structure.

The HER performance was promoted by introducing surface engineering and lattice tuning, respectively. We were able to successfully manufacture PtNi-O/C nano octahedra with a $Ni(OH)_2$/Pt(111) interface by employing surface engineering techniques. The as-prepared PtNi-O/C demonstrated record-breaking alkaline HER activity and remarkable durability. Utilizing lattice tuning, we improved the performance of the alkaline HER even further. Incorporating various annealing conditions, we investigated the relationship between HER performance and lattice parameter for PtNi/C and PtNiCu/C. Moreover, a lattice parameter range was found to deliver the optimal alkaline HER activity.

In the aspect of OER, I designed the transition metal doped cobalt-based spinel oxide structure, utilizing the outstanding acid-corrosion resistivity from Co_3O_4. After adding Ni in the structure, the geometrical configuration obeys the rule for a kinetically more favorable DOC mechanism. Specifically, I fabricated a Co-based spinel structure grown on carbon fiber paper. The as-prepared $NiCo_2O_4$ exhibited ultrahigh performance in 0.5 M H_2SO_4 with preeminent stability. These achievements provided direction for future water-splitting catalyst design and fundamentals for industrial electrolyzer development.

For the future research, here I propose several directions according to the developed

materials and techniques:

1. Incorporating the anode material $NiCo_2O_4$/CFP and cathode material PtNi-O/C into an industrial electrolyzer. Current research is conducted at lab scale using a single-cell, three-electrode system, which omits some practical engineering issues in a real water-splitting device, such as mass transport, high-temperature stability, and membrane durability, among others.

2. Since industrial water electrolysis is conducted at 60-80°C and a current density of approximately 0.5-1 A/cm^2, the durability of the catalyst, particularly the anode catalyst, must be enhanced due to the more corrosive conditions in the anode chamber. It is a potential approach to fabricate protective layers outside of the nanostructures, such as TiO_2 or graphene.

3. The $NiCo_2O_4$/CFP OER activity can be further enhanced. Incorporating a single atom of Ir on the surface may stabilize the entire structure and improve OER performance.

Bibliography

[1] N. Henrik et al. International climate negotiations: Issues at stake in view of the cop 24 un climate change conference in katowice and beyond. Report, 2018.

[2] S. Solomon et al. Climate change 2007: The physical science basis. Report, 2007.

[3] U.S. Energy Information Administration. Monthly energy review. Report, Apr 2022.

[4] College of the Desert. Module 1. hydrogen properties. 2001.

[5] IOR Energy. List of common conversion factors (engineering conversion factors).

[6] Saad Mekhilef, Rahman Saidur, and Azadeh Safari. Comparative study of different fuel cell technologies. *Renewable and Sustainable Energy Reviews*, 16(1):981–989, 2012.

[7] Ke Song, Yimin Wang, Yuhang Ding, Hongjie Xu, Philip Mueller-Welt, Tobias Stuermlinger, Katharina Bause, Christopher Ehrmann, Hannes W Weinmann, Jens Schaefer, et al. Assembly techniques for proton exchange membrane fuel cell stack: A literature review. *Renewable and Sustainable Energy Reviews*, 153:111777, 2022.

[8] Ching Chuen Chan. The state of the art of electric, hybrid, and fuel cell vehicles. *Proceedings of the IEEE*, 95(4):704–718, 2007.

[9] Hui Xing, Charles Stuart, Stephen Spence, and Hua Chen. Fuel cell power systems for maritime applications: Progress and perspectives. *Sustainability*, 13(3):1213, 2021.

[10] Thomas H Bradley, Blake A Moffitt, Dimitri N Mavris, and David E Parekh. Development and experimental characterization of a fuel cell powered aircraft. *Journal of Power sources*, 171(2):793–801, 2007.

[11] Zhigang Qi, Chunzhi He, and Arthur Kaufman. Effect of co in the anode fuel on the performance of pem fuel cell cathode. *Journal of Power Sources*, 111(2):239–247, 2002.

[12] S Shiva Kumar and V Himabindu. Hydrogen production by pem water electrolysis–a review. *Materials Science for Energy Technologies*, 2(3):442–454, 2019.

[13] Zipeng Zhao, Haotian Liu, Wenpei Gao, Wang Xue, Zeyan Liu, Jin Huang, Xiaoqing Pan, and Yu Huang. Surface-engineered ptni-o nanostructure with record-high performance for electrocatalytic hydrogen evolution reaction. *Journal of the American Chemical Society*, 140(29):9046–9050, 2018.

[14] Ping Liu and José A Rodriguez. Catalysts for hydrogen evolution from the [nife] hydrogenase to the ni2p (001) surface: the importance of ensemble effect. *Journal of the American Chemical Society*, 127(42):14871–14878, 2005.

[15] Jingqi Tian, Qian Liu, Abdullah M Asiri, and Xuping Sun. Self-supported nanoporous cobalt phosphide nanowire arrays: an efficient 3d hydrogen-evolving cathode over the wide range of ph 0–14. *Journal of the American Chemical Society*, 136(21):7587–7590, 2014.

[16] Junfeng Xie, Shuang Li, Xiaodong Zhang, Jiajia Zhang, Ruoxing Wang, Hao Zhang, Bicai Pan, and Yi Xie. Atomically-thin molybdenum nitride nanosheets with exposed active surface sites for efficient hydrogen evolution. *Chemical science*, 5(12):4615–4620, 2014.

[17] Wei-Fu Chen, Kotaro Sasaki, Chao Ma, Anatoly I Frenkel, Nebojsa Marinkovic, James T Muckerman, Yimei Zhu, and Radoslav R Adzic. Hydrogen-evolution catalysts based on non-noble metal nickel–molybdenum nitride nanosheets. *Angewandte Chemie International Edition*, 51(25):6131–6135, 2012.

[18] Jian Yu, Anran Li, Lidong Li, Xiaoxia Li, Xiaotian Wang, and Lin Guo. Morphological and structural engineering in amorphous cu2mos4 nanocages for remarkable electrocatalytic hydrogen evolution. *Science China Materials*, 62(9):1275–1284, 2019.

[19] Liang-Liang Feng, Guangtao Yu, Yuanyuan Wu, Guo-Dong Li, Hui Li, Yuanhui Sun, Tewodros Asefa, Wei Chen, and Xiaoxin Zou. High-index faceted ni3s2 nanosheet arrays as highly active and ultrastable electrocatalysts for water splitting. *Journal of the American Chemical Society*, 137(44):14023–14026, 2015.

[20] Angel T Garcia-Esparza, Dongkyu Cha, Yiwei Ou, Jun Kubota, Kazunari Domen, and Kazuhiro Takanabe. Tungsten carbide nanoparticles as efficient cocatalysts for photocatalytic overall water splitting. *ChemSusChem*, 6(1):168–181, 2013.

[21] Yong Zhao, Kazuhide Kamiya, Kazuhito Hashimoto, and Shuji Nakanishi. Hydrogen evolution by tungsten carbonitride nanoelectrocatalysts synthesized by the formation of a tungsten acid/polymer hybrid in situ. *Angewandte Chemie*, 125(51):13883–13886, 2013.

[22] Zhenming Cao, Qiaoli Chen, Jiawei Zhang, Huiqi Li, Yaqi Jiang, Shouyu Shen, Gang Fu, Bang-an Lu, Zhaoxiong Xie, and Lansun Zheng. Platinum-nickel alloy excavated nano-multipods with hexagonal close-packed structure and superior activity towards hydrogen evolution reaction. *Nature communications*, 8(1):1–7, 2017.

[23] Pengtang Wang, Xu Zhang, Jin Zhang, Sheng Wan, Shaojun Guo, Gang Lu, Jianlin Yao, and Xiaoqing Huang. Precise tuning in platinum-nickel/nickel sulfide interface nanowires for synergistic hydrogen evolution catalysis. *Nature communications*, 8(1):1–9, 2017.

[24] Andrzej Lasia. Mechanism and kinetics of the hydrogen evolution reaction. *International Journal of Hydrogen Energy*, 44(36):19484–19518, 2019.

[25] Ram Subbaraman, Dusan Tripkovic, Dusan Strmcnik, Kee-Chul Chang, Masanobu Uchimura, Arvydas P Paulikas, Vojislav Stamenkovic, and Nenad M Markovic. Enhancing hydrogen evolution activity in water splitting by tailoring li+-ni (oh) 2-pt interfaces. *Science*, 334(6060):1256–1260, 2011.

[26] Patricia A Thiel and Theodore E Madey. The interaction of water with solid surfaces: fundamental aspects. *Surface Science Reports*, 7(6-8):211–385, 1987.

[27] Michael A Henderson. The interaction of water with solid surfaces: fundamental aspects revisited. *Surface Science Reports*, 46(1-8):1–308, 2002.

[28] Huajie Yin, Shenlong Zhao, Kun Zhao, Abdul Muqsit, Hongjie Tang, Lin Chang, Huijun Zhao, Yan Gao, and Zhiyong Tang. Ultrathin platinum nanowires grown on single-layered nickel hydroxide with high hydrogen evolution activity. *Nature communications*, 6(1):1–8, 2015.

[29] Pengtang Wang, Kezhu Jiang, Gongming Wang, Jianlin Yao, and Xiaoqing Huang. Phase and interface engineering of platinum–nickel nanowires for efficient electrochemical hydrogen evolution. *Angewandte Chemie*, 128(41):13051–13055, 2016.

[30] SL Medway, CA Lucas, A Kowal, RJ Nichols, and D Johnson. In situ studies of the oxidation of nickel electrodes in alkaline solution. *Journal of Electroanalytical Chemistry*, 587(1):172–181, 2006.

[31] Boon Siang Yeo and Alexis T Bell. In situ raman study of nickel oxide and gold-supported nickel oxide catalysts for the electrochemical evolution of oxygen. *The Journal of Physical Chemistry C*, 116(15):8394–8400, 2012.

[32] Lili Fan, Peng Fei Liu, Xuecheng Yan, Lin Gu, Zhen Zhong Yang, Hua Gui Yang, Shilun Qiu, and Xiangdong Yao. Atomically isolated nickel species anchored on graphitized carbon for efficient hydrogen evolution electrocatalysis. *Nature communications*, 7(1):1–7, 2016.

[33] Reza Kavian, Sang-Il Choi, Jinho Park, Tianyuan Liu, Hsin-Chieh Peng, Ning Lu, Jinguo Wang, Moon J Kim, Younan Xia, and Seung Woo Lee. Pt–ni octahedral nanocrystals as a class of highly active electrocatalysts toward the hydrogen evolution reaction in an alkaline electrolyte. *Journal of Materials Chemistry A*, 4(32):12392–12397, 2016.

[34] AI Frenkel, EA Stern, M Qian, and M Newville. Multiple-scattering x-ray-absorption fine-structure analysis and thermal expansion of alkali halides. *Physical Review B*, 48(17):12449, 1993.

[35] Qingying Jia, Wentao Liang, Michael K Bates, Prasanna Mani, Wendy Lee, and Sanjeev Mukerjee. Activity descriptor identification for oxygen reduction on platinum-based bimetallic nanoparticles: in situ observation of the linear composition–strain–activity relationship. *ACS nano*, 9(1):387–400, 2015.

[36] H Modrow, Ss Bucher, JJ Rehr, and AL Ankudinov. Calculation and interpretation of k-shell x-ray absorption near-edge structure of transition metal oxides. *Physical Review B*, 67(3):035123, 2003.

[37] Liang Cao, Zipeng Zhao, Zeyan Liu, Wenpei Gao, Sheng Dai, Joonho Gha, Wang Xue, Hongtao Sun, Xiangfeng Duan, Xiaoqing Pan, et al. Differential surface elemental distribution leads to significantly enhanced stability of ptni-based orr catalysts. *Matter*, 1(6):1567–1580, 2019.

[38] Zipeng Zhao, Miao Feng, Jihan Zhou, Zeyan Liu, Mufan Li, Zheng Fan, Oshton Tsen, Jianwei Miao, Xiangfeng Duan, and Yu Huang. Composition tunable ternary pt–ni–co octahedra for optimized oxygen reduction activity. *Chemical Communications*, 52(75):11215–11218, 2016.

[39] Xiaoqing Huang, Zipeng Zhao, Yu Chen, Enbo Zhu, Mufan Li, Xiangfeng Duan, and Yu Huang. A rational design of carbon-supported dispersive pt-based octahedra as efficient oxygen reduction reaction catalysts. *Energy & Environmental Science*, 7(9):2957–2962, 2014.

[40] Yadong Yin, Robert M Rioux, Can K Erdonmez, Steven Hughes, Gabor A Somorjai, and A Paul Alivisatos. Formation of hollow nanocrystals through the nanoscale kirkendall effect. *Science*, 304(5671):711–714, 2004.

[41] Mufan Li, Kaining Duanmu, Chengzhang Wan, Tao Cheng, Liang Zhang, Sheng Dai, Wenxin Chen, Zipeng Zhao, Peng Li, Huilong Fei, et al. Single-atom tailoring of platinum nanocatalysts for high-performance multifunctional electrocatalysis. *Nature Catalysis*, 2(6):495–503, 2019.

[42] Jing M Chen. Carbon neutrality: toward a sustainable future. *The Innovation*, 2(3), 2021.

[43] Fang Wang, Jean Damascene Harindintwali, Zhizhang Yuan, Min Wang, Faming Wang, Sheng Li, Zhigang Yin, Lei Huang, Yuhao Fu, Lei Li, et al. Technologies and perspectives for achieving carbon neutrality. *The Innovation*, 2(4):100180, 2021.

[44] Xianhua Wu, Zhiqing Tian, and Ji Guo. A review of the theoretical research and practical progress of carbon neutrality. *Sustainable Operations and Computers*, 3:54–66, 2022.

[45] Wolfgang Lubitz and William Tumas. Hydrogen: an overview. *Chemical reviews*, 107(10):3900–3903, 2007.

[46] H Ishaq and I Dincer. Comparative assessment of renewable energy-based hydrogen production methods. *Renewable and Sustainable Energy Reviews*, 135:110192, 2021.

[47] Jie Zheng, Wenchao Sheng, Zhongbin Zhuang, Bingjun Xu, and Yushan Yan. Universal dependence of hydrogen oxidation and evolution reaction activity of platinum-group metals on ph and hydrogen binding energy. *Science advances*, 2(3):e1501602, 2016.

[48] Marcelo Carmo, David L Fritz, Jürgen Mergel, and Detlef Stolten. A comprehensive review on pem water electrolysis. *International journal of hydrogen energy*, 38(12):4901–4934, 2013.

[49] SA Grigoriev, VN Fateev, DG Bessarabov, and P Millet. Current status, research trends,

and challenges in water electrolysis science and technology. *International Journal of Hydrogen Energy*, 45(49):26036–26058, 2020.

[50] Leigang Li, Pengtang Wang, Qi Shao, and Xiaoqing Huang. Recent progress in advanced electrocatalyst design for acidic oxygen evolution reaction. *Advanced Materials*, 33(50):2004243, 2021.

[51] Rasmus Frydendal, Elisa A Paoli, Ib Chorkendorff, Jan Rossmeisl, and Ifan EL Stephens. Toward an active and stable catalyst for oxygen evolution in acidic media: Ti-stabilized mno2. *Advanced Energy Materials*, 5(22):1500991, 2015.

[52] Wai Ling Kwong, Cheng Choo Lee, Andrey Shchukarev, Erik Björn, and Johannes Messinger. High-performance iron (iii) oxide electrocatalyst for water oxidation in strongly acidic media. *Journal of Catalysis*, 365:29–35, 2018.

[53] Michael Huynh, Tuncay Ozel, Chong Liu, Eric C Lau, and Daniel G Nocera. Design of template-stabilized active and earth-abundant oxygen evolution catalysts in acid. *Chemical science*, 8(7):4779–4794, 2017.

[54] Prasad Prakash Patel, Moni Kanchan Datta, Oleg I Velikokhatnyi, Ramalinga Kuruba, Krishnan Damodaran, Prashanth Jampani, Bharat Gattu, Pavithra Murugavel Shanthi, Sameer S Damle, and Prashant N Kumta. Noble metal-free bifunctional oxygen evolution and oxygen reduction acidic media electro-catalysts. *Scientific reports*, 6(1):1–14, 2016.

[55] Marta Blasco-Ahicart, Joaquín Soriano-López, Jorge J Carbó, Josep M Poblet, and Jose-Ramon Galan-Mascaros. Polyoxometalate electrocatalysts based on earth-abundant metals for efficient water oxidation in acidic media. *Nature chemistry*, 10(1):24–30, 2018.

[56] Xiulin Yang, Henan Li, Ang-Yu Lu, Shixiong Min, Zacharie Idriss, Mohamed Nejib Hedhili, Kuo-Wei Huang, Hicham Idriss, and Lain-Jong Li. Highly acid-durable carbon

coated co3o4 nanoarrays as efficient oxygen evolution electrocatalysts. *Nano Energy*, 25:42–50, 2016.

[57] Jared S Mondschein, Juan F Callejas, Carlos G Read, Jamie YC Chen, Cameron F Holder, Catherine K Badding, and Raymond E Schaak. Crystalline cobalt oxide films for sustained electrocatalytic oxygen evolution under strongly acidic conditions. *Chemistry of Materials*, 29(3):950–957, 2017.

[58] Kai-Li Yan, Jing-Qi Chi, Jing-Yi Xie, Bin Dong, Zi-Zhang Liu, Wen-Kun Gao, Jia-Hui Lin, Yong-Ming Chai, and Chen-Guang Liu. Mesoporous ag-doped co3o4 nanowire arrays supported on fto as efficient electrocatalysts for oxygen evolution reaction in acidic media. *Renewable Energy*, 119:54–61, 2018.

[59] A Rebekah, E Ashok Kumar, C Viswanathan, and N Ponpandian. Effect of cation substitution in mnco2o4 spinel anchored over rgo for enhancing the electrocatalytic activity towards oxygen evolution reaction (oer). *International Journal of Hydrogen Energy*, 45(11):6391–6403, 2020.

[60] José Béjar, Lorena Álvarez-Contreras, J Ledesma-García, Noé Arjona, and LG Arriaga. Electrocatalytic evaluation of co3o4 and nico2o4 rosettes-like hierarchical spinel as bi-functional materials for oxygen evolution (oer) and reduction (orr) reactions in alkaline media. *Journal of Electroanalytical Chemistry*, 847:113190, 2019.

[61] Tianze Wu, Shengnan Sun, Jiajia Song, Shibo Xi, Yonghua Du, Bo Chen, Wardhana Aji Sasangka, Hanbin Liao, Chee Lip Gan, Günther G Scherer, et al. Iron-facilitated dynamic active-site generation on spinel coal2o4 with self-termination of surface reconstruction for water oxidation. *Nature Catalysis*, 2(9):763–772, 2019.

[62] Xi Rong, Jules Parolin, and Alexie M Kolpak. A fundamental relationship between reaction mechanism and stability in metal oxide catalysts for oxygen evolution. *Acs Catalysis*, 6(2):1153–1158, 2016.

[63] Zhen-Feng Huang, Jiajia Song, Shuo Dou, Xiaogang Li, Jiong Wang, and Xin Wang. Strategies to break the scaling relation toward enhanced oxygen electrocatalysis. *Matter*, 1(6):1494–1518, 2019.

[64] Jan Rossmeisl, Z-W Qu, H Zhu, G-J Kroes, and Jens Kehlet Nørskov. Electrolysis of water on oxide surfaces. *Journal of Electroanalytical Chemistry*, 607(1-2):83–89, 2007.

[65] Zhi Wei Seh, Jakob Kibsgaard, Colin F Dickens, IB Chorkendorff, Jens K Nørskov, and Thomas F Jaramillo. Combining theory and experiment in electrocatalysis: Insights into materials design. *Science*, 355(6321):eaad4998, 2017.

[66] Feifei Li, Haoqiang Ai, Dong Liu, Kin Ho Lo, and Hui Pan. An enhanced oxygen evolution reaction on 2d coooh via strain engineering: an insightful view from spin state transition. *Journal of Materials Chemistry A*, 9(33):17749–17759, 2021.

[67] Ya-Hui Fang and Zhi-Pan Liu. Mechanism and tafel lines of electro-oxidation of water to oxygen on ruo2 (110). *Journal of the American Chemical Society*, 132(51):18214–18222, 2010.

[68] Chao Lin, Ji-Li Li, Xiaopeng Li, Shuai Yang, Wei Luo, Yaojia Zhang, Sung-Hae Kim, Dong-Hyung Kim, Sambhaji S Shinde, Ye-Fei Li, et al. In-situ reconstructed ru atom array on α-mno2 with enhanced performance for acidic water oxidation. *Nature Catalysis*, 4(12):1012–1023, 2021.

[69] Alexis Grimaud, Oscar Diaz-Morales, Binghong Han, Wesley T Hong, Yueh-Lin Lee, Livia Giordano, Kelsey A Stoerzinger, Marc Koper, and Yang Shao-Horn. Activating lattice oxygen redox reactions in metal oxides to catalyse oxygen evolution. *Nature chemistry*, 9(5):457–465, 2017.

[70] Jong Suk Yoo, Xi Rong, Yusu Liu, and Alexie M Kolpak. Role of lattice oxygen participation in understanding trends in the oxygen evolution reaction on perovskites. *ACS Catalysis*, 8(5):4628–4636, 2018.

[71] Tobias Reier, Hong Nhan Nong, Detre Teschner, Robert Schlögl, and Peter Strasser. Electrocatalytic oxygen evolution reaction in acidic environments–reaction mechanisms and catalysts. *Advanced Energy Materials*, 7(1):1601275, 2017.

[72] Chang Liu, Jin Qian, Yifan Ye, Hua Zhou, Cheng-Jun Sun, Colton Sheehan, Zhiyong Zhang, Gang Wan, Yi-Sheng Liu, Jinghua Guo, et al. Oxygen evolution reaction over catalytic single-site co in a well-defined brookite tio2 nanorod surface. *Nature Catalysis*, 4(1):36–45, 2021.

[73] Dandan Chen, Qiuhong Sun, Cheng Han, Yuanyuan Guo, Qi Huang, William A Goddard, and Jinjie Qian. Enhanced oxygen evolution catalyzed by in situ formed fe-doped ni oxyhydroxides in carbon nanotubes. *Journal of Materials Chemistry A*, 10(30):16007–16015, 2022.

[74] Bailin Tian, Hyeyoung Shin, Shengtang Liu, Muchun Fei, Zhangyan Mu, Cheng Liu, Yanghang Pan, Yamei Sun, William A Goddard III, and Mengning Ding. Double-exchange-induced in situ conductivity in nickel-based oxyhydroxides: An effective descriptor for electrocatalytic oxygen evolution. *Angewandte Chemie International Edition*, 60(30):16448–16456, 2021.

[75] Harsharaj S Jadhav, Alok Kumar Rai, Jae Young Lee, Jaekook Kim, and Chan-Jin Park. Enhanced electrochemical performance of flower-like co3o4 as an anode material for high performance lithium-ion batteries. *Electrochimica Acta*, 146:270–277, 2014.

[76] Thomas M Arruda, Badri Shyam, Joseph M Ziegelbauer, Sanjeev Mukerjee, and David E Ramaker. Investigation into the competitive and site-specific nature of anion adsorption on pt using in situ x-ray absorption spectroscopy. *The Journal of Physical Chemistry C*, 112(46):18087–18097, 2008.

[77] Cuihua An, Yijing Wang, Yanan Huang, Yanan Xu, Lifang Jiao, and Huatang Yuan.

Porous nico2o4 nanostructures for high performance supercapacitors via a microemulsion technique. *Nano Energy*, 10:125–134, 2014.

[78] Roderick J Hill, James R Craig, and GV Gibbs. Systematics of the spinel structure type. *Physics and chemistry of minerals*, 4(4):317–339, 1979.

[79] Jinzhen Huang, Hongyuan Sheng, R Dominic Ross, Jiecai Han, Xianjie Wang, Bo Song, and Song Jin. Modifying redox properties and local bonding of co3o4 by ceo2 enhances oxygen evolution catalysis in acid. *Nature communications*, 12(1):1–11, 2021.

[80] Ailong Li, Shuang Kong, Chenxi Guo, Hideshi Ooka, Kiyohiro Adachi, Daisuke Hashizume, Qike Jiang, Hongxian Han, Jianping Xiao, and Ryuhei Nakamura. Enhancing the stability of cobalt spinel oxide towards sustainable oxygen evolution in acid. *Nature Catalysis*, 5(2):109–118, 2022.

[81] Michel Lenglet, René Guillamet, Jean Dürr, D Gryffroy, and RE Vandenberghe. Electronic structure of nico2o4 by xanes, exafs and 61ni mössbauer studies. *Solid state communications*, 74(10):1035–1039, 1990.

[82] VG Harris, NC Koon, CM Williams, Q Zhang, M Abe, JP Kirkland, and DA McKeown. Direct measurement of octahedral and tetrahedral site environments in nizn-ferrites. *IEEE Transactions on Magnetics*, 31(6):3473–3475, 1995.

[83] Chao Wei, Zhenxing Feng, Murat Baisariyev, Linghui Yu, Li Zeng, Tianpin Wu, Haiyan Zhao, Yaqin Huang, Michael J Bedzyk, Thirumany Sritharan, et al. Valence change ability and geometrical occupation of substitution cations determine the pseudocapacitance of spinel ferrite xfe2o4 (x= mn, co, ni, fe). *Chemistry of Materials*, 28(12):4129–4133, 2016.

[84] JF Marco, JR Gancedo, M Gracia, JL Gautier, E Ríos, and FJ Berry. Characterization of the nickel cobaltite, nico2o4, prepared by several methods: an xrd, xanes, exafs, and xps study. *Journal of Solid State Chemistry*, 153(1):74–81, 2000.

[85] Nana Han, Ke R Yang, Zhiyi Lu, Yingjie Li, Wenwen Xu, Tengfei Gao, Zhao Cai, Ying Zhang, Victor S Batista, Wen Liu, et al. Nitrogen-doped tungsten carbide nanoarray as an efficient bifunctional electrocatalyst for water splitting in acid. *Nature communications*, 9(1):1–10, 2018.

[86] Hongyu Guo, Zhiwei Fang, Hao Li, Desiree Fernandez, Graeme Henkelman, Simon M Humphrey, and Guihua Yu. Rational design of rhodium–iridium alloy nanoparticles as highly active catalysts for acidic oxygen evolution. *ACS nano*, 13(11):13225–13234, 2019.

[87] Xiaopeng Han, Guowei He, Yu He, Jinfeng Zhang, Xuerong Zheng, Lanlan Li, Cheng Zhong, Wenbin Hu, Yida Deng, and Tian-Yi Ma. Engineering catalytic active sites on cobalt oxide surface for enhanced oxygen electrocatalysis. *Advanced Energy Materials*, 8(10):1702222, 2018.

[88] Qianfeng Liu, Zhiping Chen, Zhao Yan, Yao Wang, Erdong Wang, Sheng Wang, Shudong Wang, and Gongquan Sun. Crystal-plane-dependent activity of spinel co3o4 towards water splitting and the oxygen reduction reaction. *ChemElectroChem*, 5(7):1080–1086, 2018.

[89] Yong Xu, Fengchu Zhang, Tian Sheng, Tao Ye, Ding Yi, Yijun Yang, Shoujie Liu, Xi Wang, and Jiannian Yao. Clarifying the controversial catalytic active sites of co 3 o 4 for the oxygen evolution reaction. *Journal of Materials Chemistry A*, 7(40):23191–23198, 2019.

[90] Miao Zhang, Moreno De Respinis, and Heinz Frei. Time-resolved observations of water oxidation intermediates on a cobalt oxide nanoparticle catalyst. *Nature chemistry*, 6(4):362–367, 2014.

[91] Jia Chen and Annabella Selloni. Water adsorption and oxidation at the co3o4 (110) surface. *The Journal of Physical Chemistry Letters*, 3(19):2808–2814, 2012.

[92] Monica Garcia-Mota, Michal Bajdich, Venkatasubramanian Viswanathan, Aleksandra Vojvodic, Alexis T Bell, and Jens K Nørskov. Importance of correlation in determining electrocatalytic oxygen evolution activity on cobalt oxides. *The Journal of Physical Chemistry C*, 116(39):21077–21082, 2012.

[93] Aliki Moysiadou, Seunghwa Lee, Chia-Shuo Hsu, Hao Ming Chen, and Xile Hu. Mechanism of oxygen evolution catalyzed by cobalt oxyhydroxide: cobalt superoxide species as a key intermediate and dioxygen release as a rate-determining step. *Journal of the American Chemical Society*, 142(27):11901–11914, 2020.

[94] J Gregory McAlpin, Yogesh Surendranath, Mircea Dinca, Troy A Stich, Sebastian A Stoian, William H Casey, Daniel G Nocera, and R David Britt. Epr evidence for co (iv) species produced during water oxidation at neutral ph. *Journal of the American Chemical Society*, 132(20):6882–6883, 2010.

[95] Lee-Ping Wang and Troy Van Voorhis. Direct-coupling o2 bond forming a pathway in cobalt oxide water oxidation catalysts. *The Journal of Physical Chemistry Letters*, 2(17):2200–2204, 2011.

[96] Andrew M Ullman, Casey N Brodsky, Nancy Li, Shao-Liang Zheng, and Daniel G Nocera. Probing edge site reactivity of oxidic cobalt water oxidation catalysts. *Journal of the American Chemical Society*, 138(12):4229–4236, 2016.

[97] Hieu H Pham, Mu-Jeng Cheng, Heinz Frei, and Lin-Wang Wang. Surface proton hopping and fast-kinetics pathway of water oxidation on co3o4 (001) surface. *ACS Catalysis*, 6(8):5610–5617, 2016.

[98] Isabela C Man, Hai-Yan Su, Federico Calle-Vallejo, Heine A Hansen, José I Martínez, Nilay G Inoglu, John Kitchin, Thomas F Jaramillo, Jens K Nørskov, and Jan Rossmeisl. Universality in oxygen evolution electrocatalysis on oxide surfaces. *ChemCatChem*, 3(7):1159–1165, 2011.

[99] Hsin-Yi Wang, Sung-Fu Hung, Ying-Ya Hsu, Lulu Zhang, Jianwei Miao, Ting-Shan Chan, Qihua Xiong, and Bin Liu. In situ spectroscopic identification of μ-oo bridging on spinel co3o4 water oxidation electrocatalyst. *The Journal of Physical Chemistry Letters*, 7(23):4847–4853, 2016.